ESI for:

N-Coordinated Tellurenium(II) and Telluronium(IV) cations: Synthesis, Structure and Hydrolysis.

Martin Hejda, Lukáš Doležal, Jan Blahut, Emanuel Hupf, Jiří Tydlitát, Roman Jambor, Aleš Růžička, Jens Beckmann* and Libor Dostál*

*E-mails: libor.dostal@upce.cz (L.D.), j.beckmann@uni-bremen.de (J.B.)

Table of contents:

1) Solution NMR spectra of studied compounds.

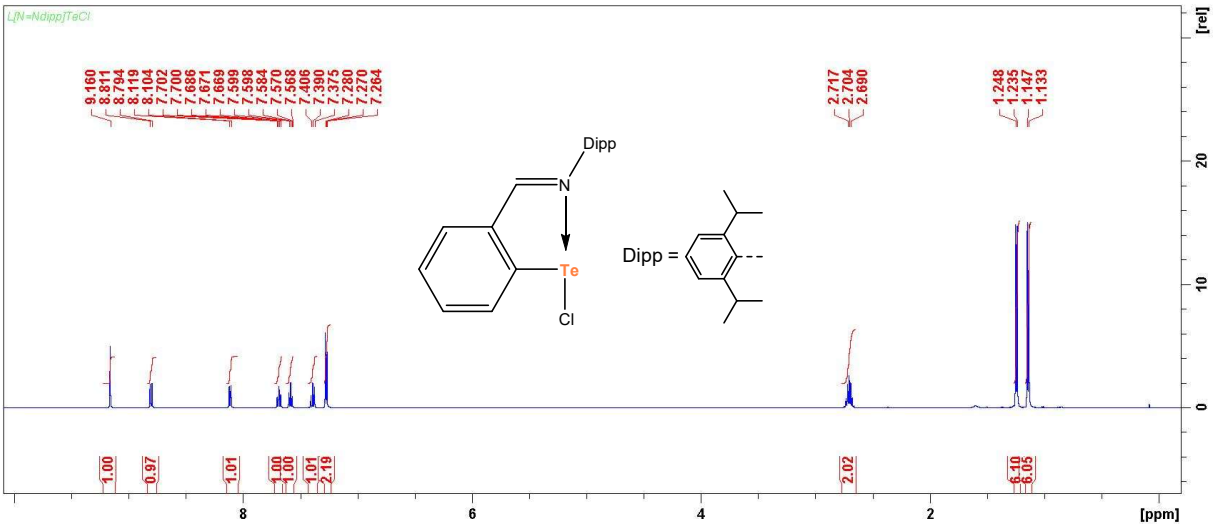

Figure S1: ^{1}H NMR spectrum of **CN^{Dipp}TeCl** in $CDCl_3$ (500 MHz).

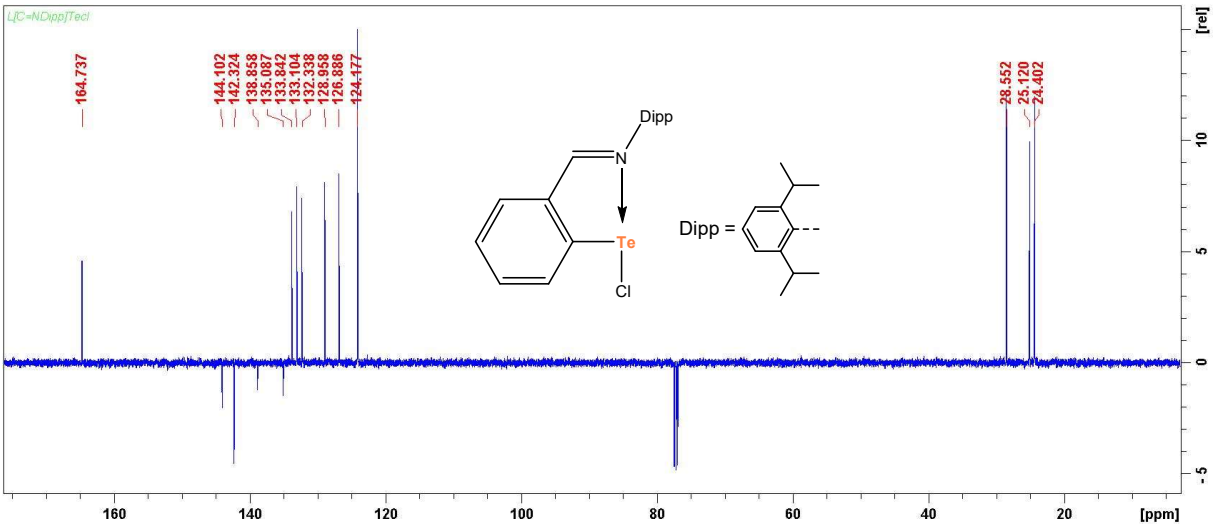

Figure S2: ^{13}C{^{1}H}-APT NMR spectrum of **CN^{Dipp}TeCl** in $CDCl_3$ (125.6 MHz).

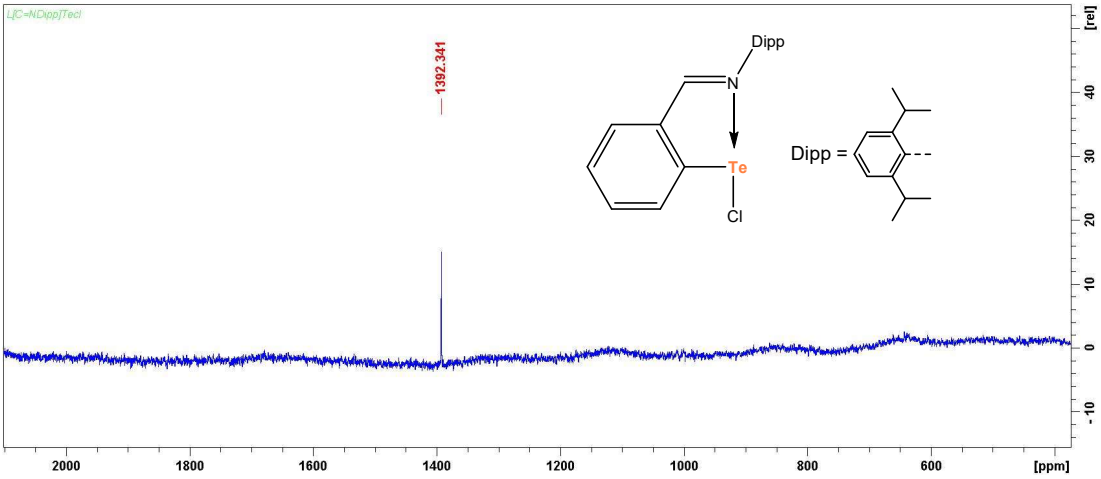

Figure S3: ^{125}Te{^{1}H} NMR spectrum of **CN^{Dipp}TeCl** in $CDCl_3$ (158.0 MHz).

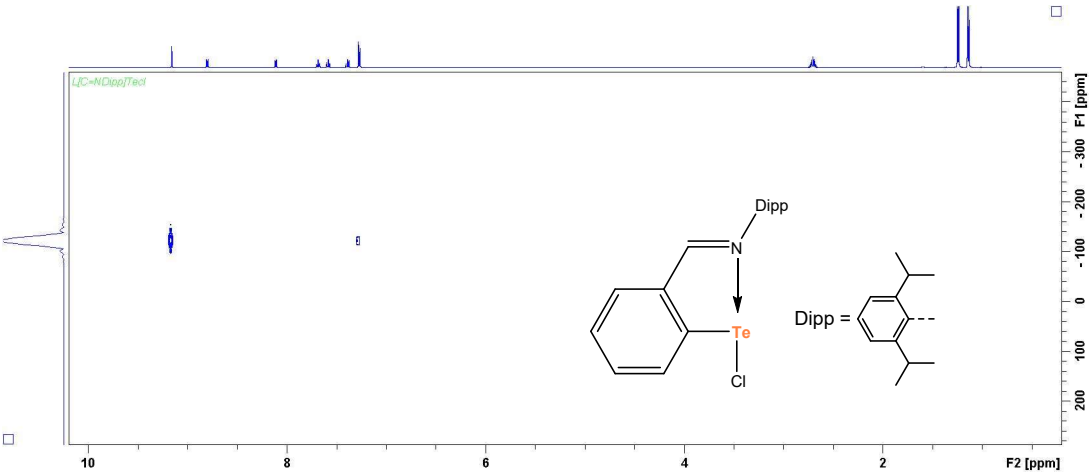

Figure S4: ^{15}N,^{1}H HMBC NMR spectrum of **CN^{Dipp}TeCl** in $CDCl_3$.

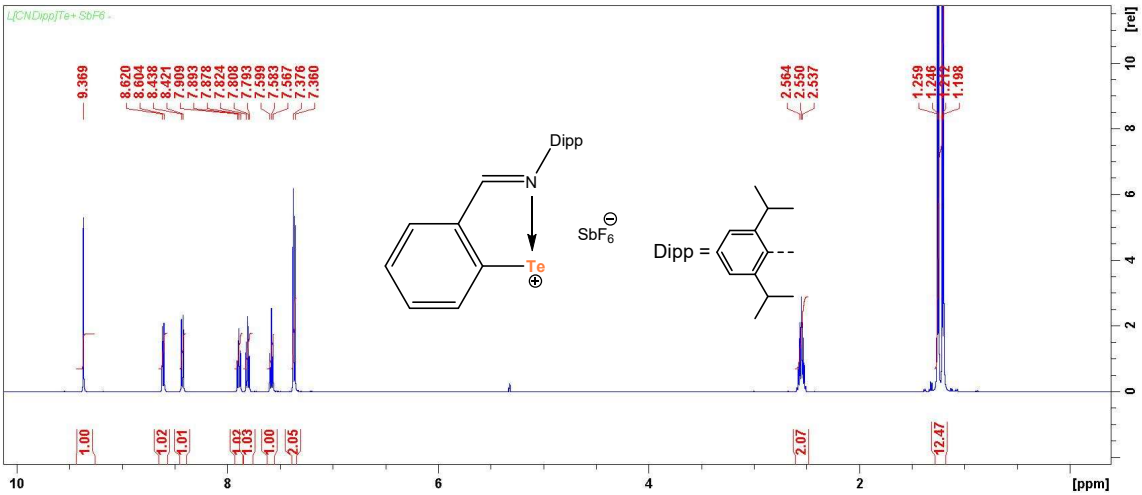

Figure S5: ^{1}H NMR spectrum of **[CN^{Dipp}Te]SbF$_6$** in CD_2Cl_2 (500 MHz).

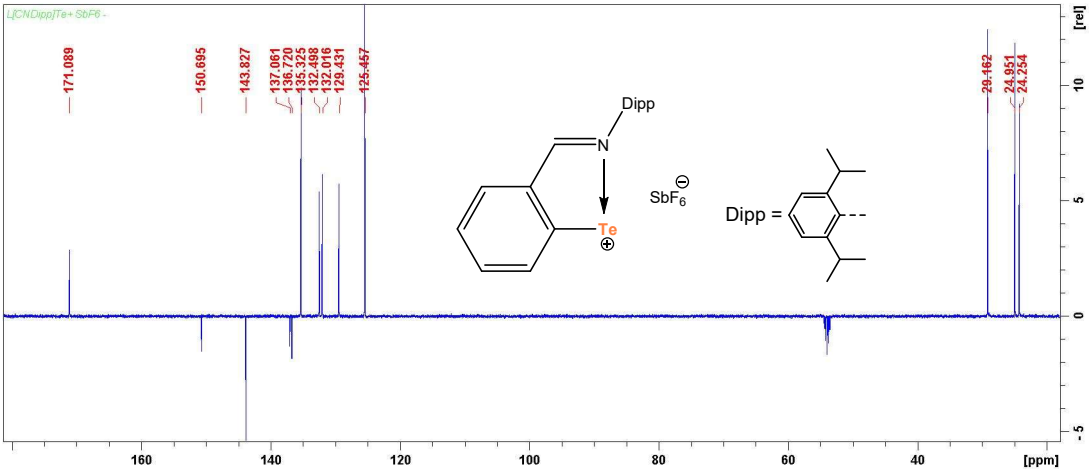

Figure S6: $^{13}C\{^{1}H\}$-APT NMR spectrum of **[CN^{Dipp}Te]SbF$_6$** in CD_2Cl_2 (125.6 MHz).

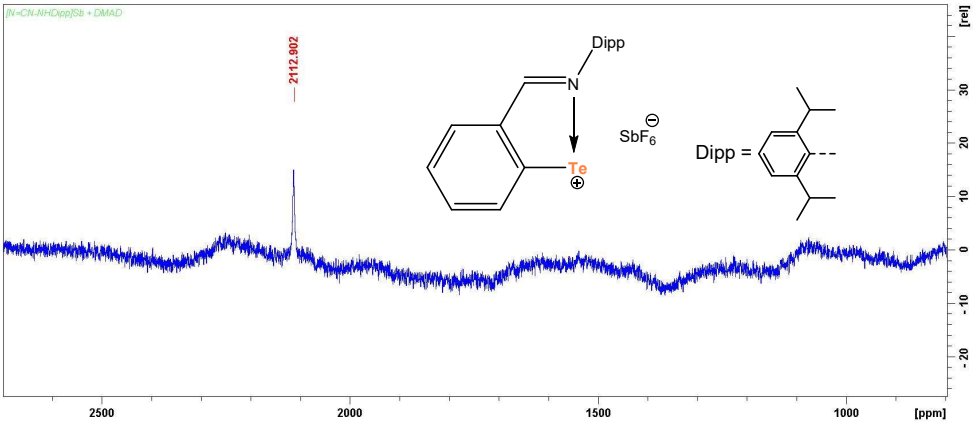

Figure S7: $^{125}Te\{^{1}H\}$ NMR spectrum of **[CN^{Dipp}Te]SbF$_6$** in CD_2Cl_2 (158.0 MHz).

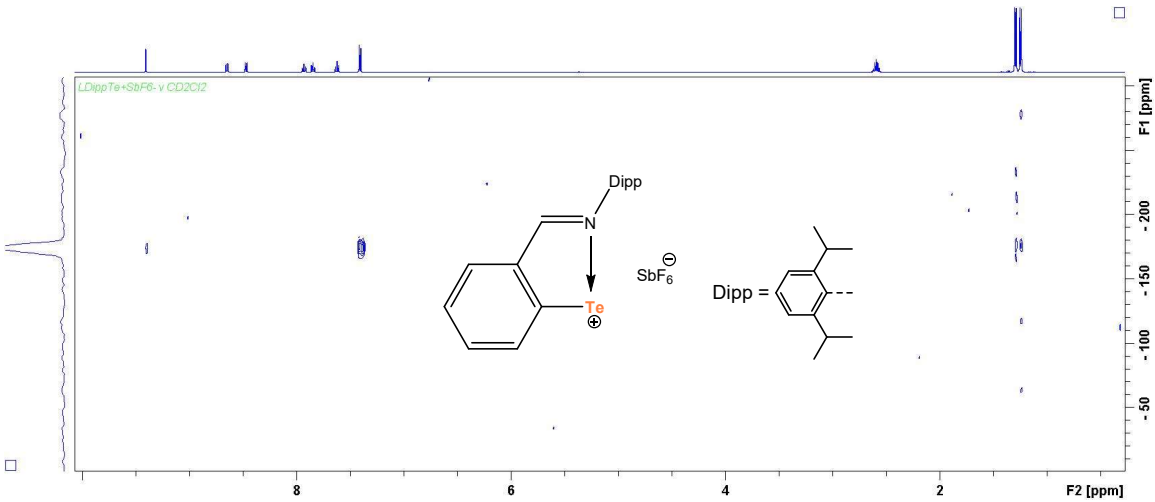

Figure S8: $^{15}N,^{1}H$ HMBC NMR spectrum of **[CN^{Dipp}Te]SbF$_6$** in CD_2Cl_2.

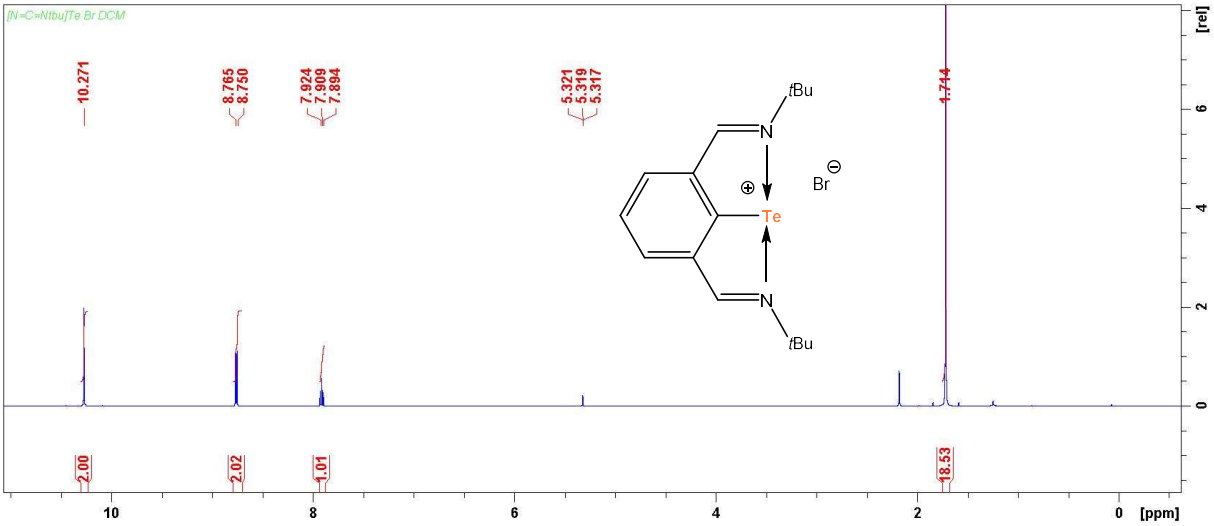

Figure S9: ^{1}H NMR spectrum of **[NCN^{tBu}Te]Br** in CD_2Cl_2 (500 MHz).

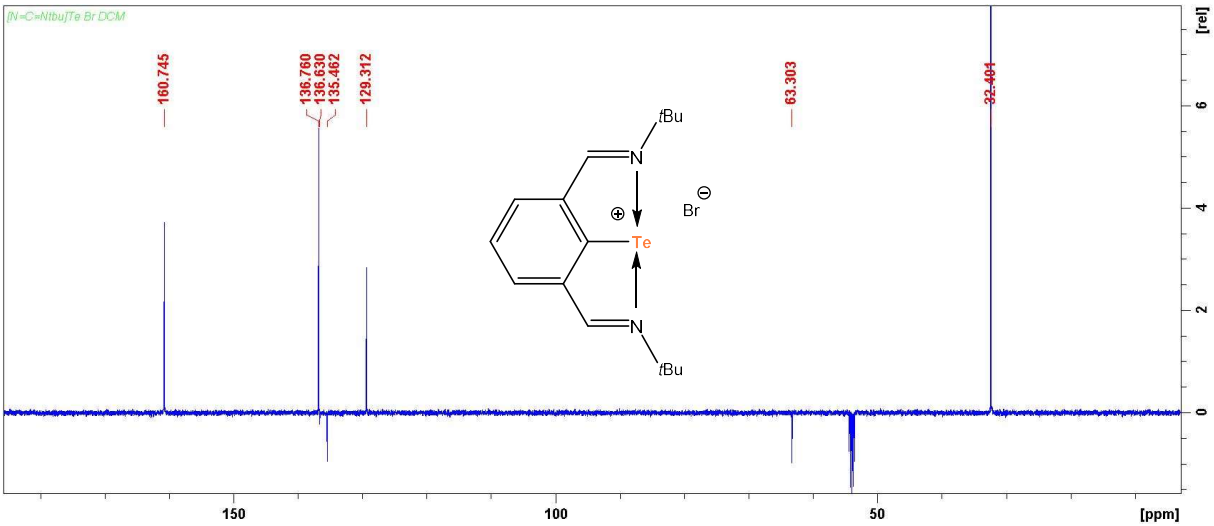

Figure S10: ^{13}C{^{1}H}-APT NMR spectrum of **[NCN^{tBu}Te]Br** in CD_2Cl_2 (125.6 MHz).

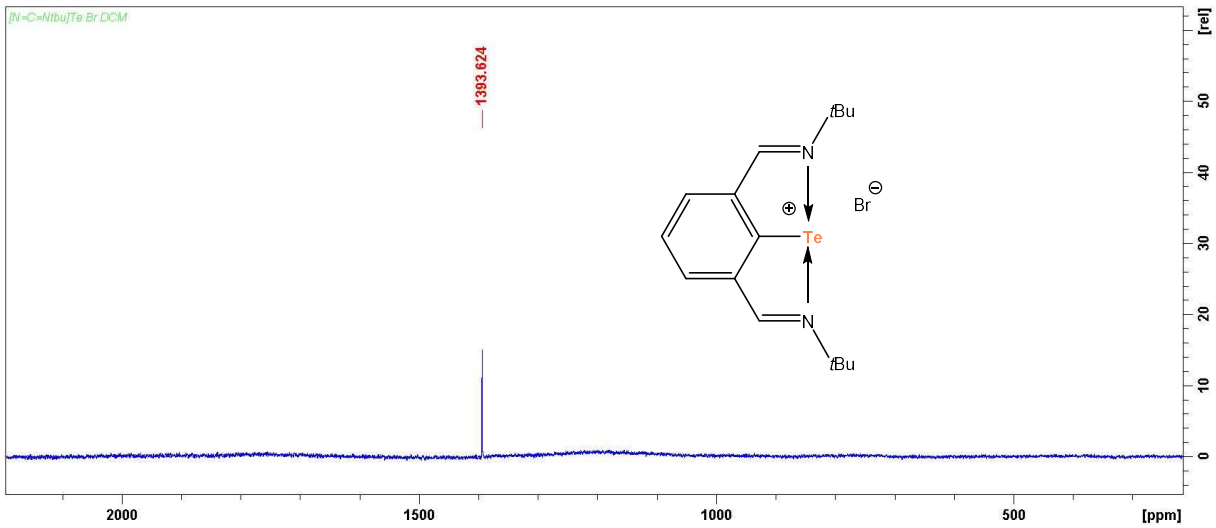

Figure S11: ^{125}Te{^{1}H} NMR spectrum of **[NCN$^{t\mathrm{Bu}}$Te]Br** in CD_2Cl_2 (158.0 MHz).

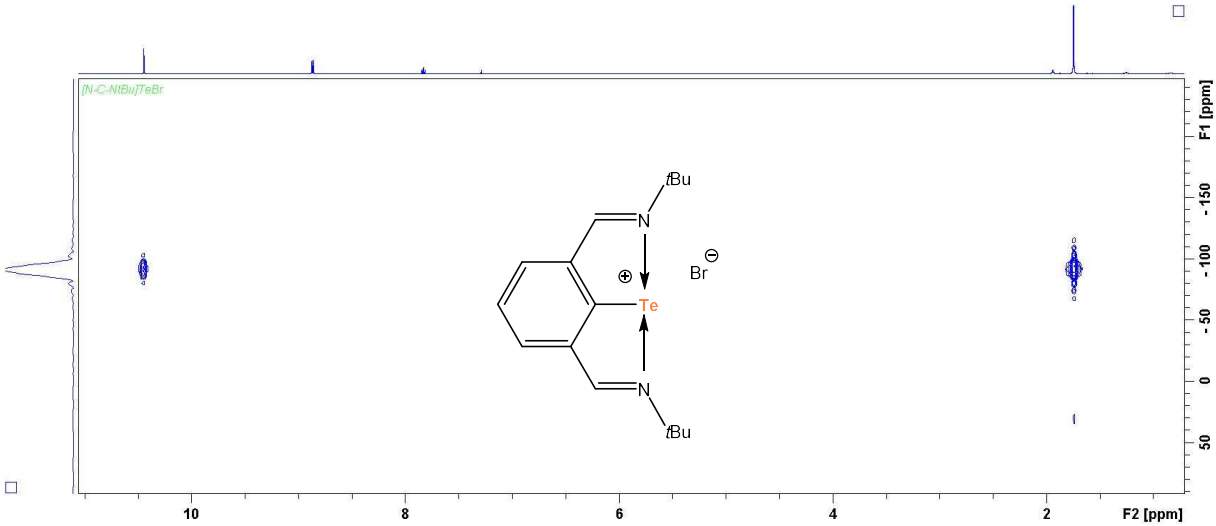

Figure S12: ^{15}N,^{1}H HMBC NMR spectrum of **[NCN$^{t\mathrm{Bu}}$Te]Br** in $CDCl_3$.

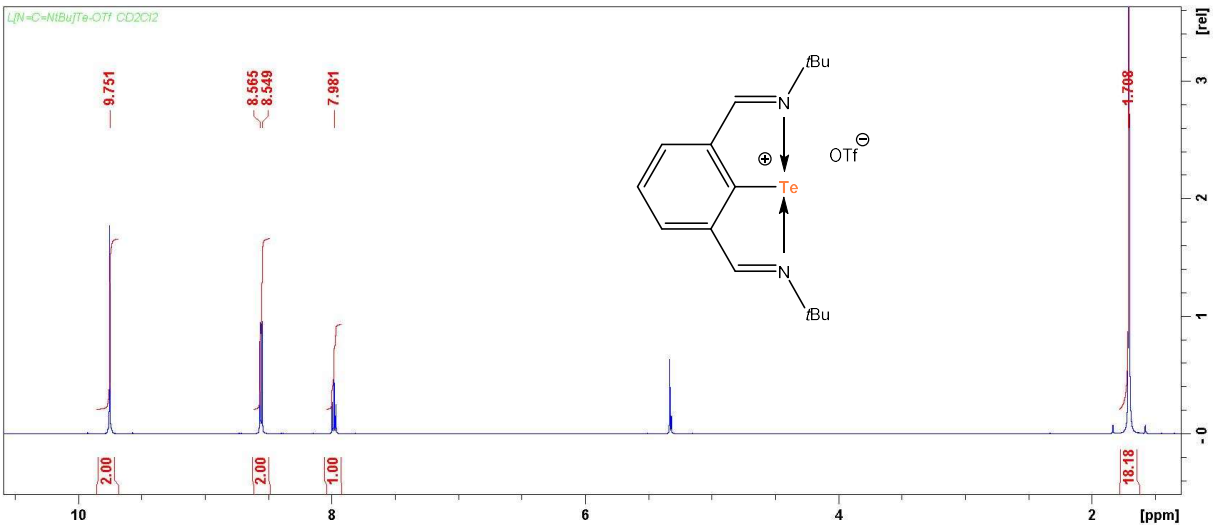

Figure S13: ^{1}H NMR spectrum of **[NCN$^{t\mathrm{Bu}}$Te]OTf** in CD_2Cl_2 (500 MHz).

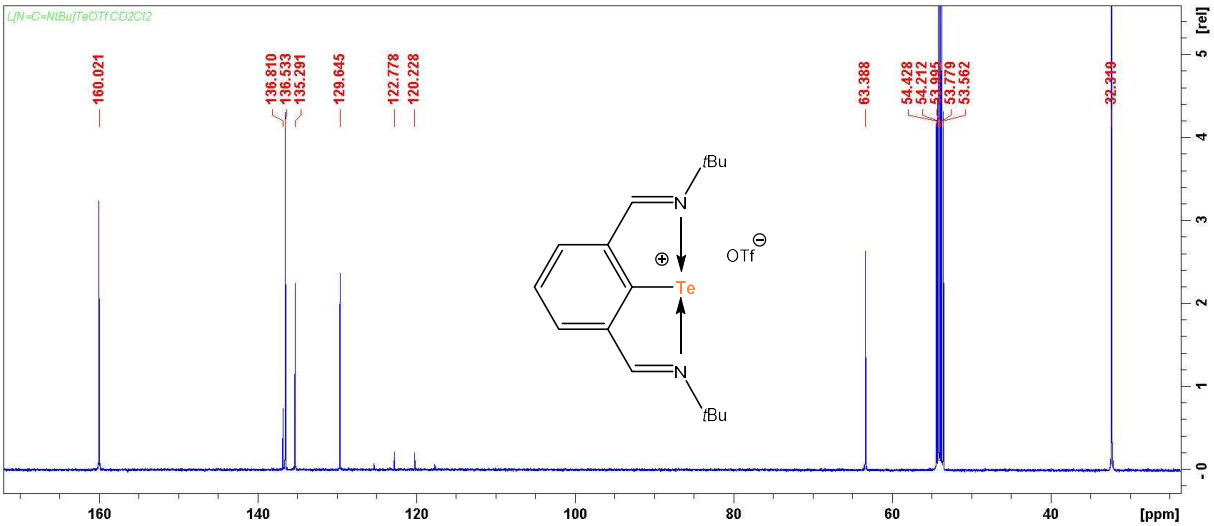

Figure S14: ^{13}C{^{1}H} NMR spectrum of [**NCN$^{t\mathrm{Bu}}$Te]OTf** in CD_2Cl_2 (125.6 MHz).

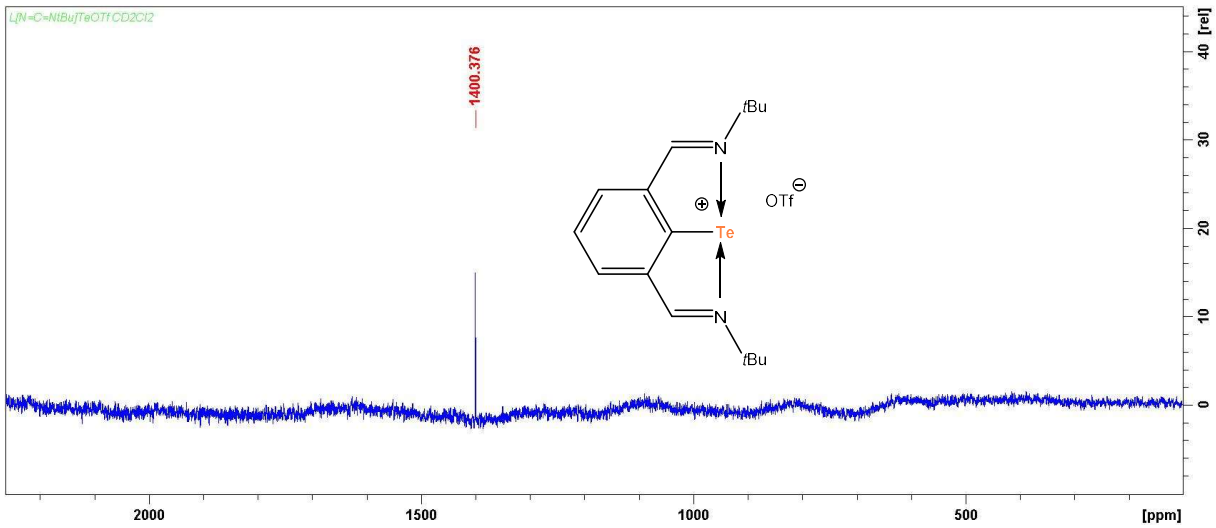

Figure S15: ^{125}Te{^{1}H} NMR spectrum of [**NCN^{tBu}Te]OTf** in CD_2Cl_2 (158.0 MHz).

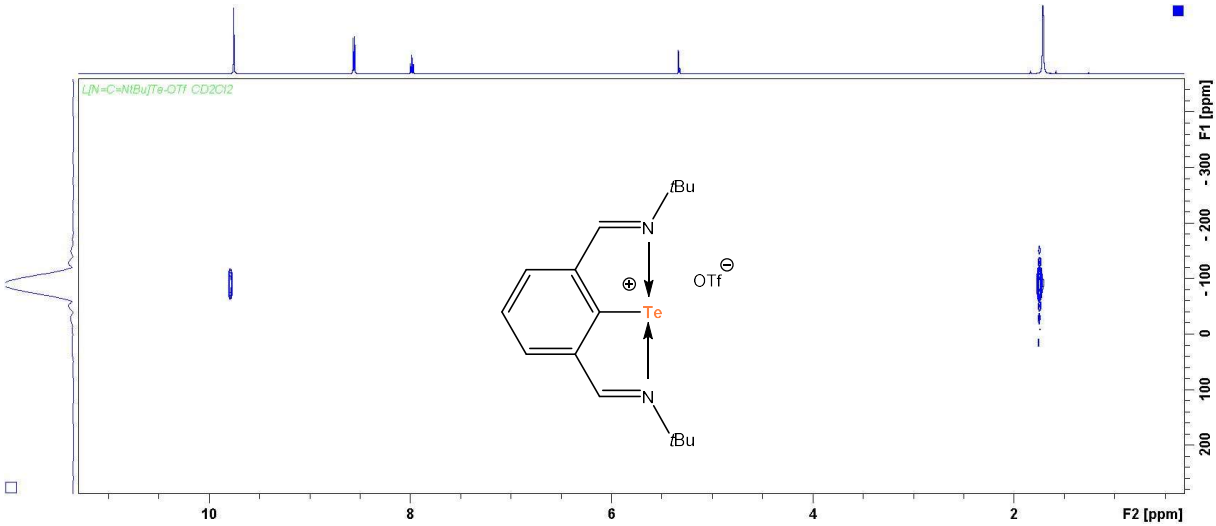

Figure S16: ^{15}N,^{1}H HMBC NMR spectrum of [**NCN^{tBu}Te]OTf** in CD_2Cl_2.

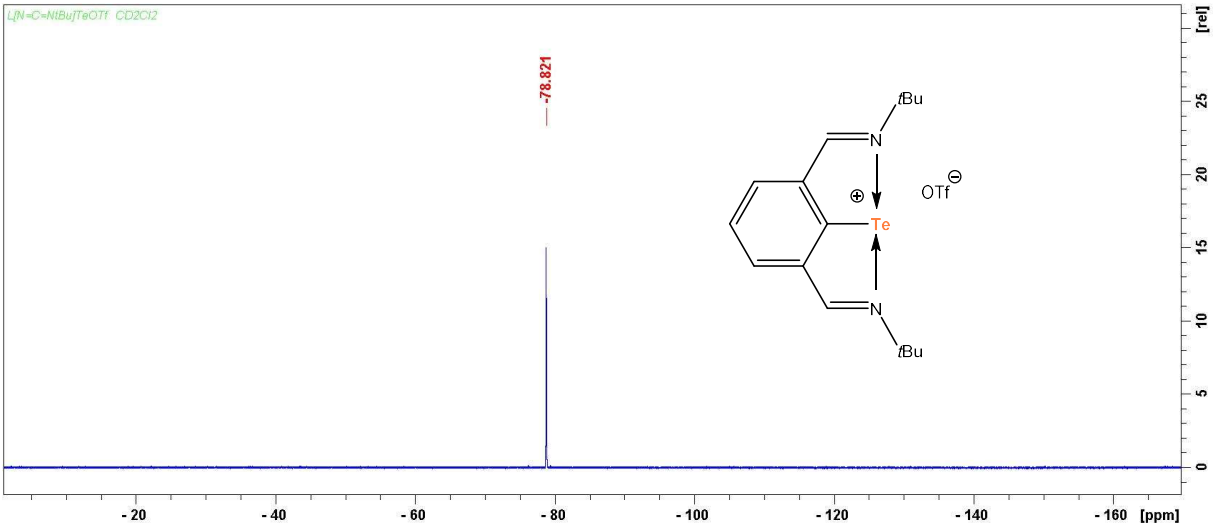

Figure S17: $^{19}F\{^{1}H\}$ NMR spectrum of [**NCN^{tBu}Te]OTf** in CD_2Cl_2 (376.5 MHz).

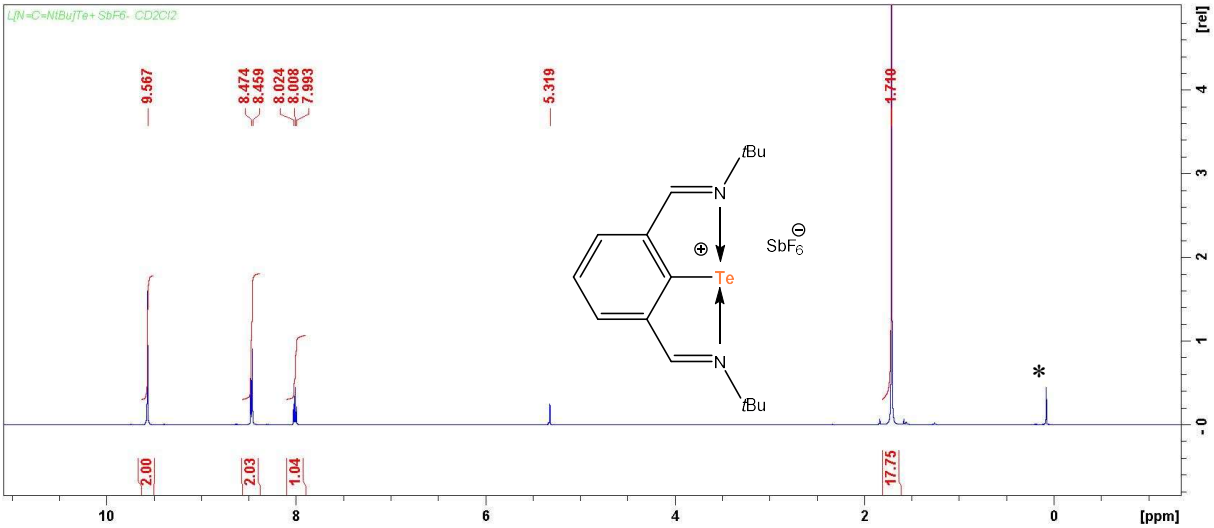

Figure S18: ^{1}H NMR spectrum of [**NCN^{tBu}Te]SbF$_6$** in CD_2Cl_2 (500 MHz). *denotes traces of silicon grease

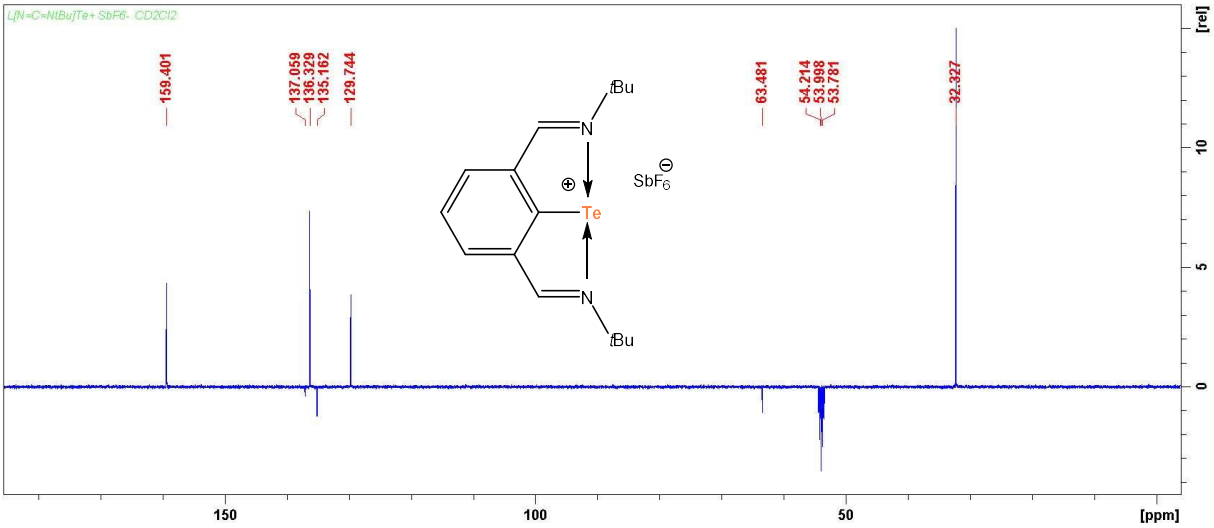

Figure S19: $^{13}C\{^{1}H\}$-APT NMR spectrum of **[NCN^{tBu}Te]SbF$_6$** in CD_2Cl_2 (125.6 MHz).

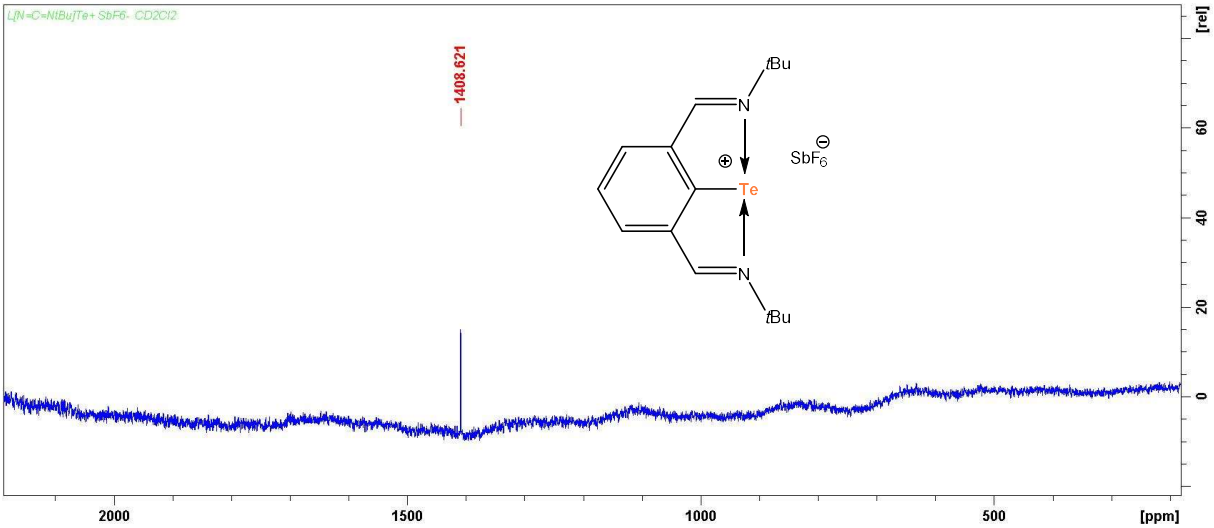

Figure S20: $^{125}Te\{^{1}H\}$ NMR spectrum of **[NCN^{tBu}Te]SbF$_6$** in CD_2Cl_2 (158.0 MHz).

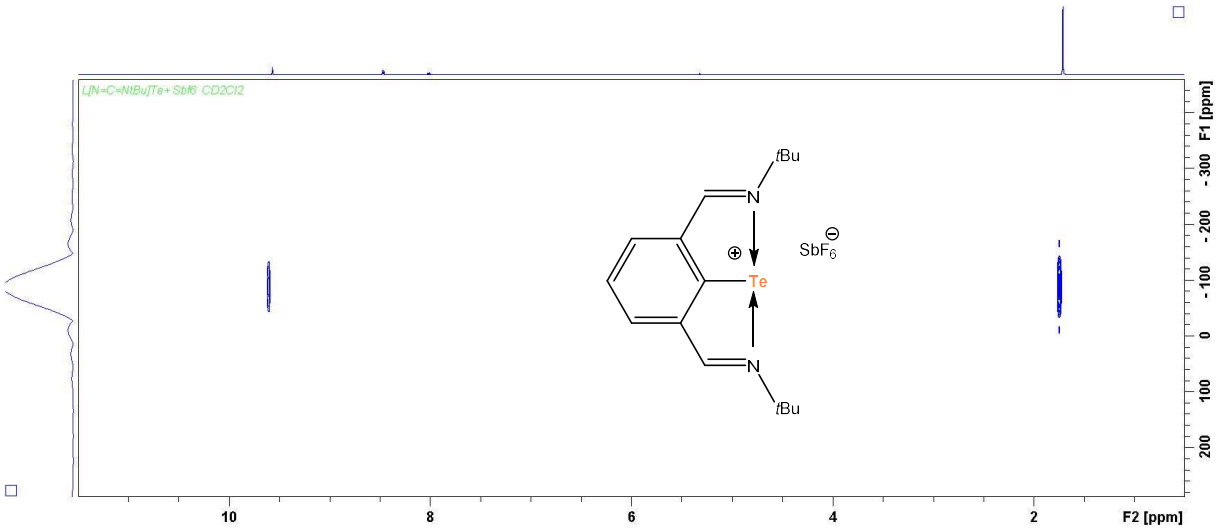

Figure S21: $^{15}N,^{1}H$ HMBC NMR spectrum of **[NCN^{tBu}Te]SbF$_6$** in CD_2Cl_2.

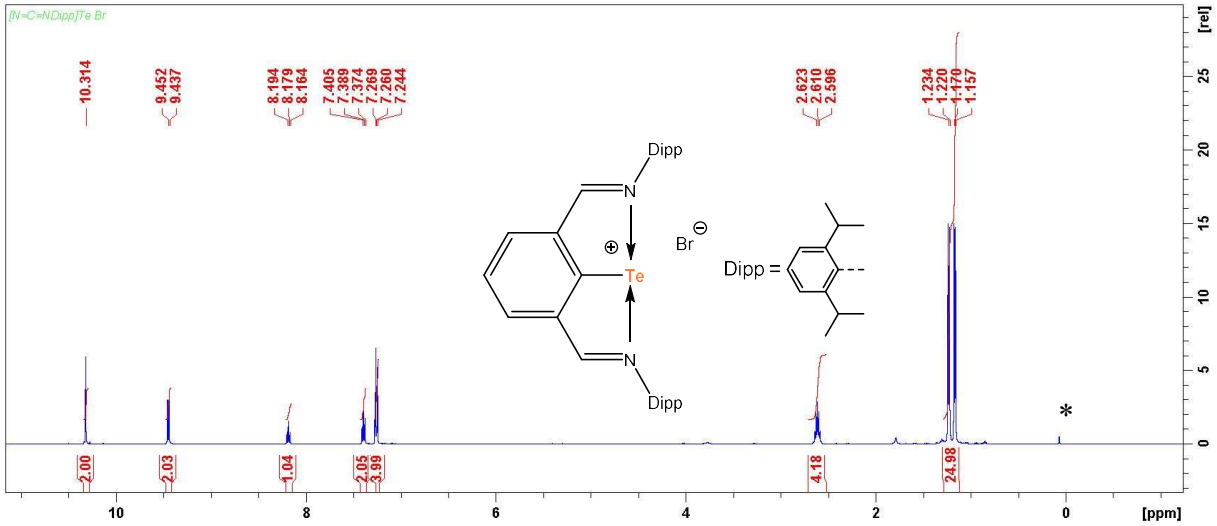

Figure S22: ^{1}H NMR spectrum of **[NCN^{Dipp}Te]Br** in $CDCl_3$ (500 MHz). *denotes traces of silicon grease

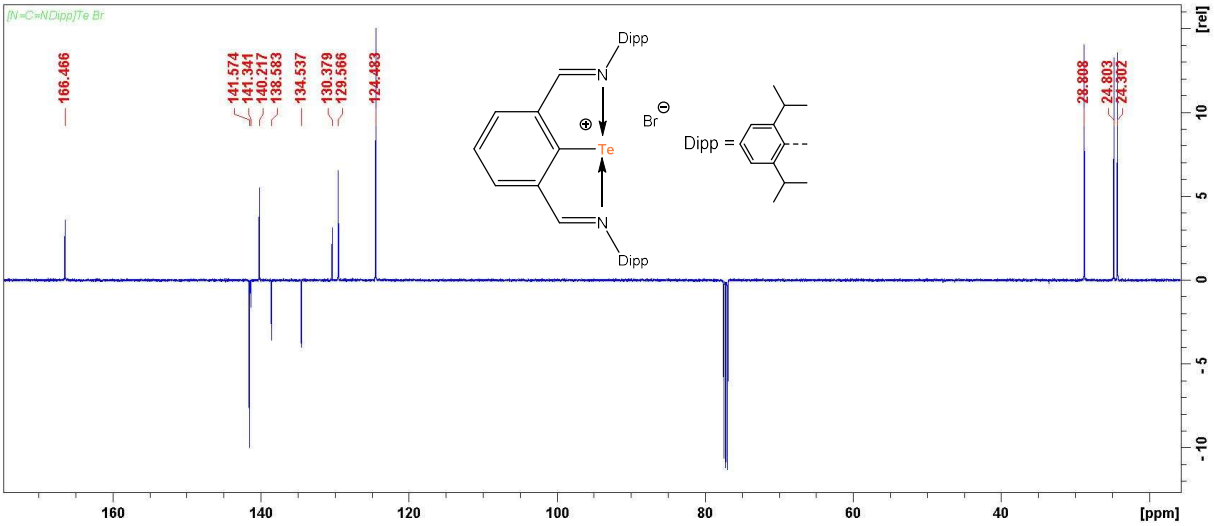

Figure S23: $^{13}C\{^{1}H\}$-APT NMR spectrum of **[NCN^{Dipp}Te]Br** in $CDCl_3$ (125.6 MHz).

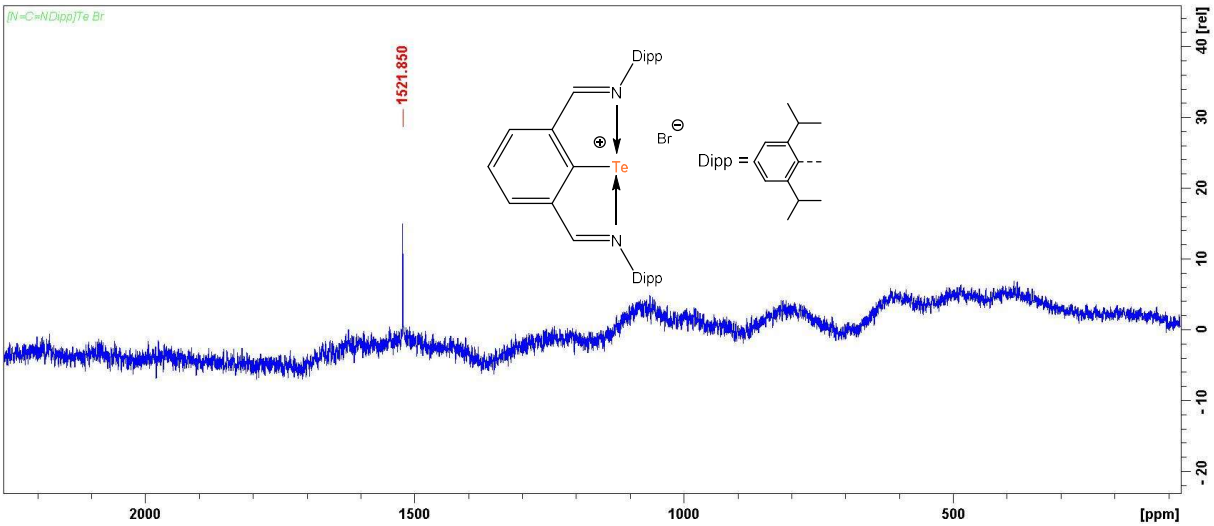

Figure S24: $^{125}Te\{^{1}H\}$ NMR spectrum of **[NCN^{Dipp}Te]Br** in $CDCl_3$ (158.0 MHz).

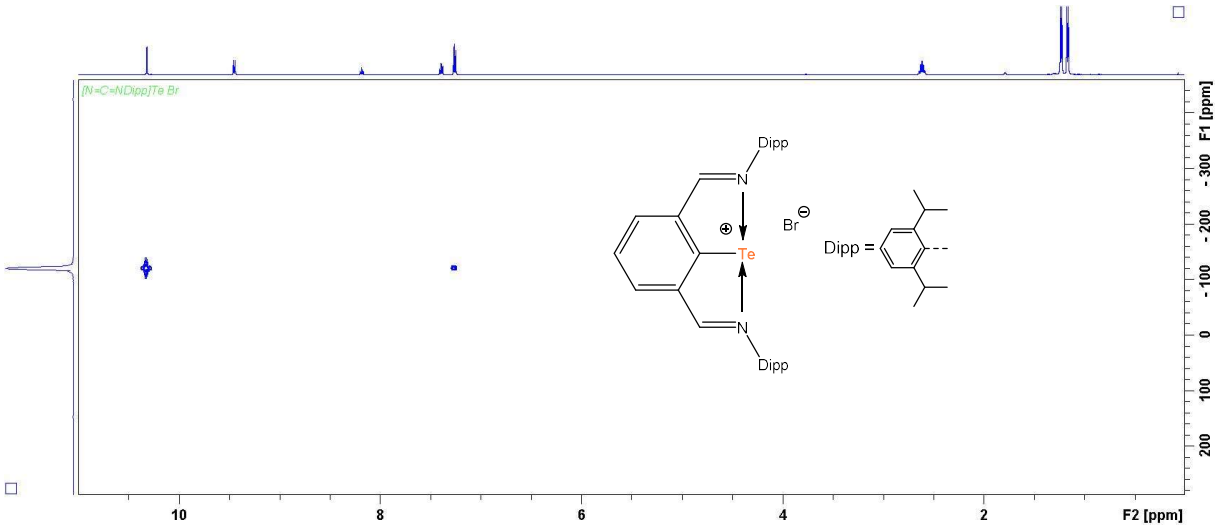

Figure S25: $^{15}N,^{1}H$ HMBC NMR spectrum of **[NCN^{Dipp}Te]Br** in $CDCl_3$.

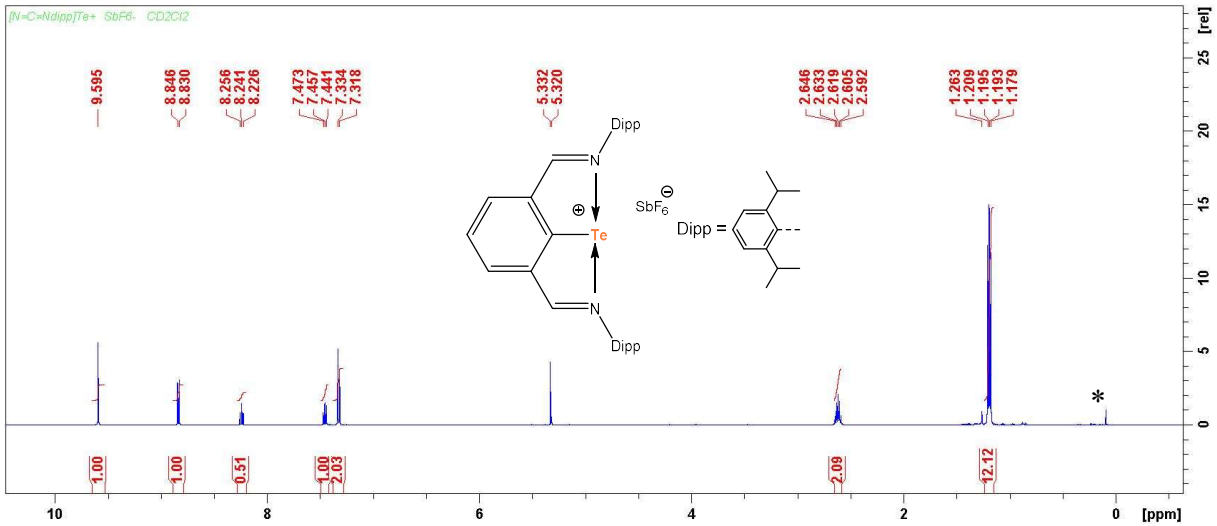

Figure S26: ^{1}H NMR spectrum of **[NCN^{Dipp}Te]SbF$_6$** in CD_2Cl_2 (500 MHz). *denotes traces of silicon grease

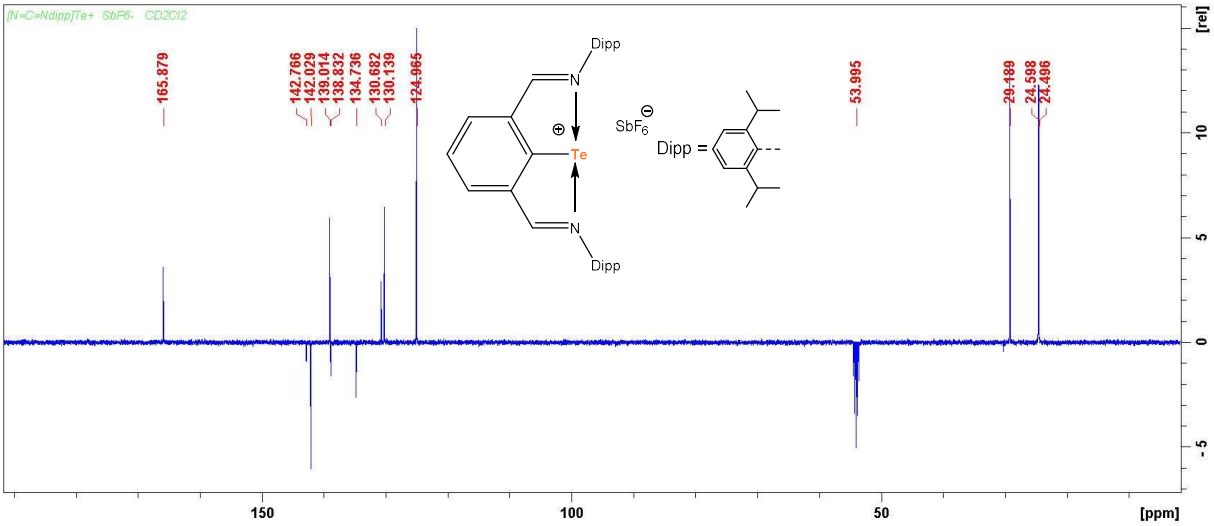

Figure S27: $^{13}C\{^{1}H\}$-APT NMR spectrum of **[NCN^{Dipp}Te]SbF$_6$** in CD_2Cl_2 (125.6 MHz).

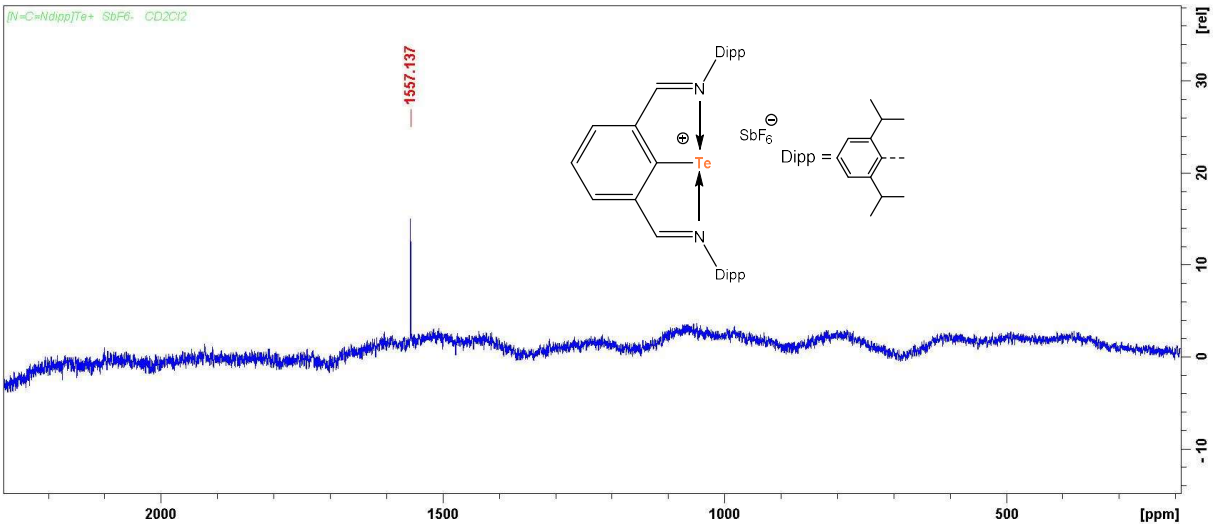

Figure S28: $^{125}Te\{^{1}H\}$ NMR spectrum of **[NCN^{Dipp}Te]SbF$_6$** in CD_2Cl_2 (158.0 MHz).

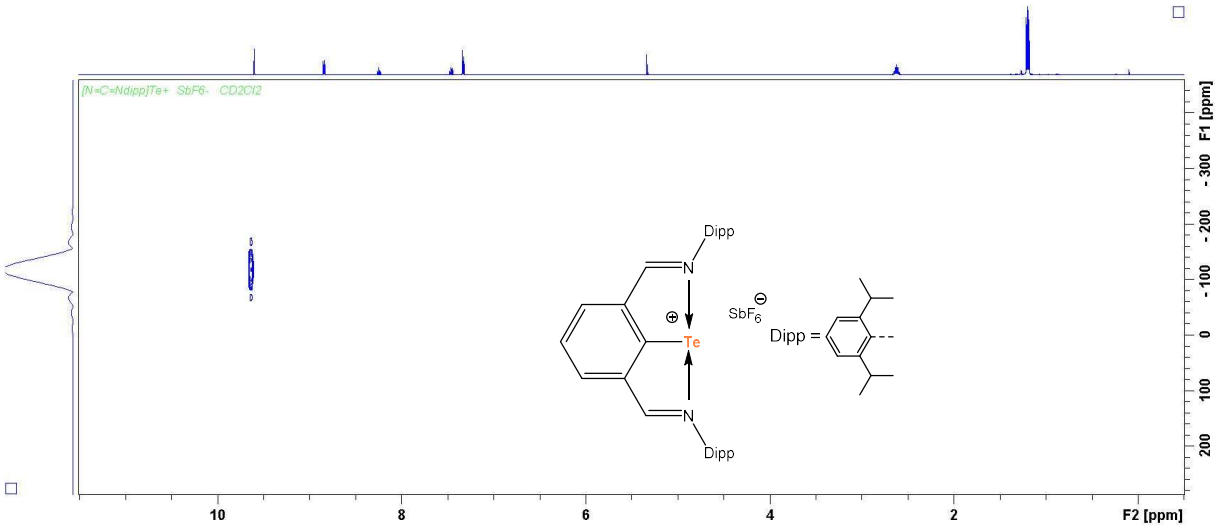

Figure S29: $^{15}N,^{1}H$ HMBC NMR spectrum of **[NCN^{Dipp}Te]SbF$_6$** in CD_2Cl_2.

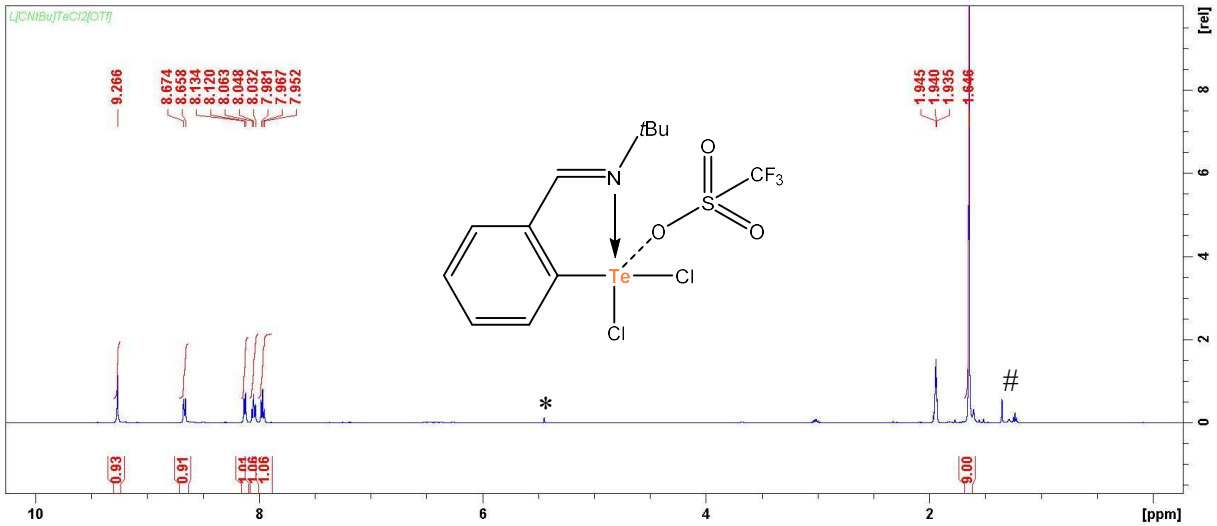

Figure S30: ^{1}H NMR spectrum of **[CN^{tBu}TeCl$_2$]OTf** in CD_3CN (500 MHz). *denotes traces of dichloromethane used in the synthesis, # traces of hexane used for washing of crystals before analysis

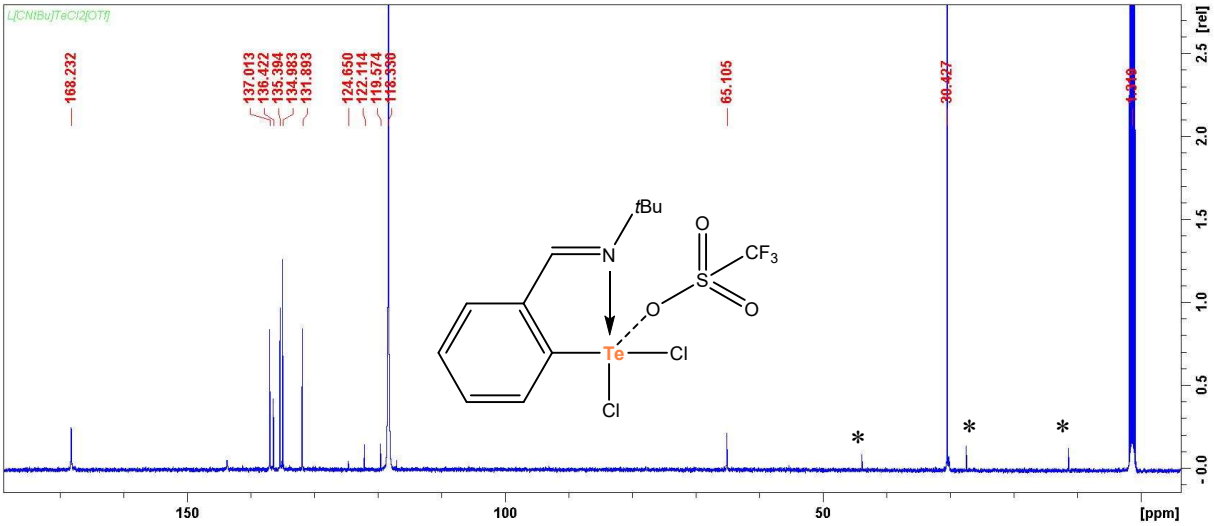

Figure S31: $^{13}C\{^{1}H\}$ NMR spectrum of **[CN^{tBu}TeCl$_2$]OTf** in CD_3CN (125.6 MHz). *denotes traces of hexane.

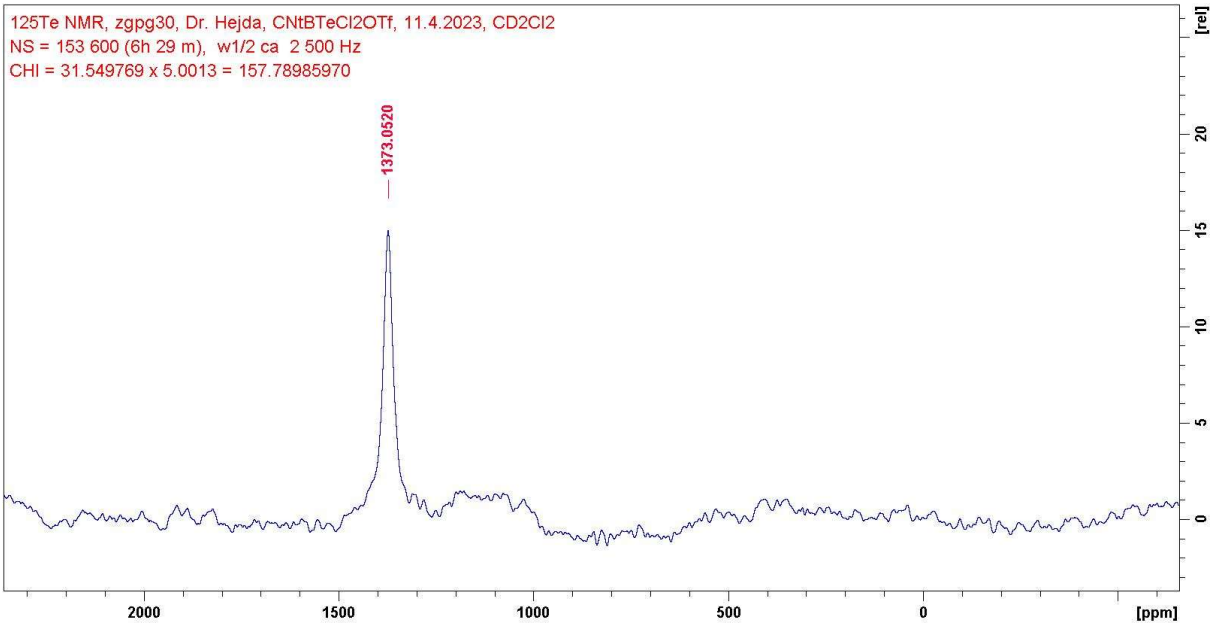

Figure S32: $^{125}Te\{^{1}H\}$ NMR spectrum of **[CN^{tBu}TeCl$_2$]OTf** in CD_3CN (158.0 MHz).

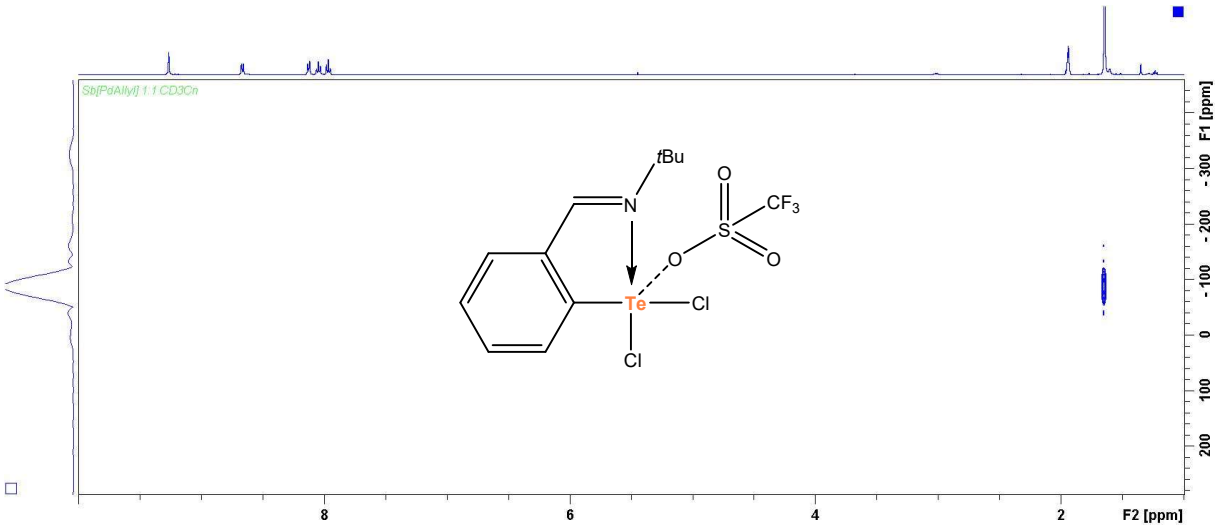

Figure S33: $^{15}N,^{1}H$ HMBC NMR spectrum of **[CN^{tBu}TeCl$_2$]OTf** in CD_3CN.

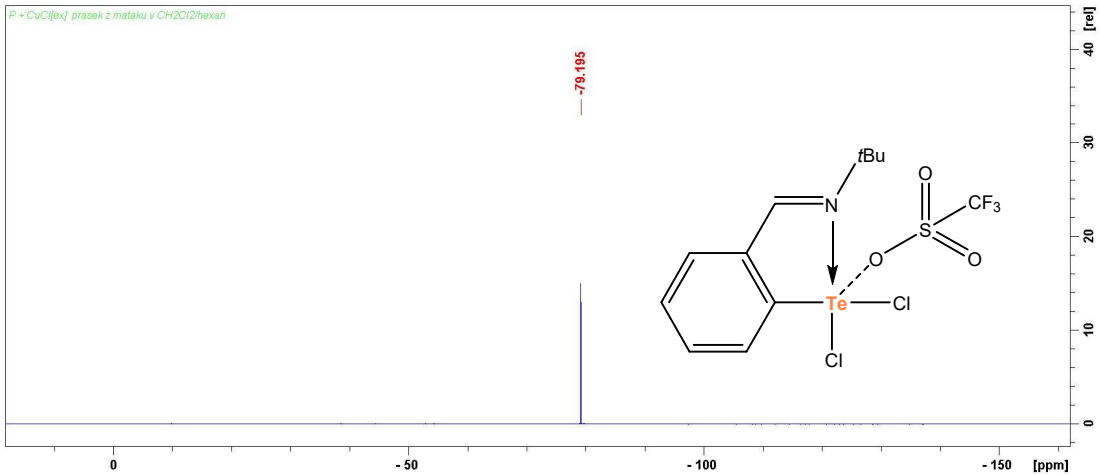

Figure S34: $^{19}F\{^{1}H\}$ NMR spectrum of **[CN^{tBu}TeCl$_2$]OTf** in CD_3CN (376.5 MHz).

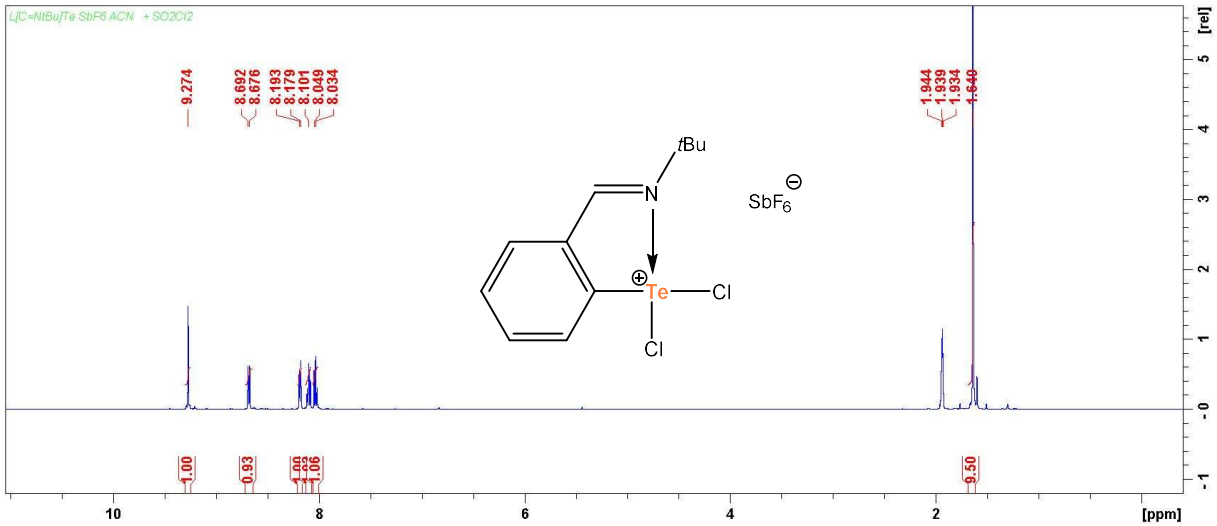

Figure S35: ^{1}H NMR spectrum of **[CN$^{t\mathrm{Bu}}$TeCl$_2$]SbF$_6$** in CD_3CN (500 MHz).

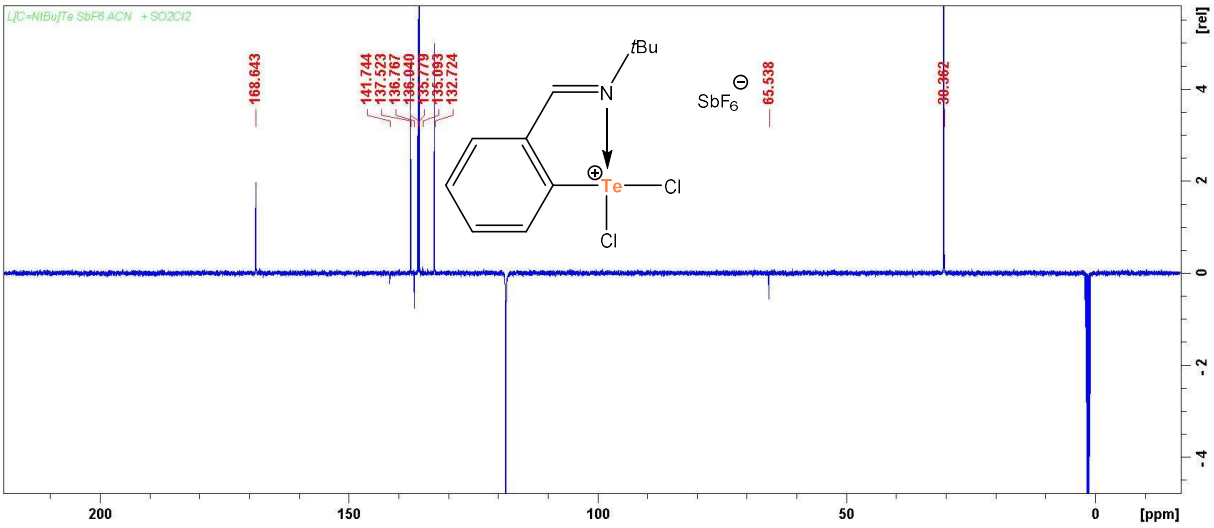

Figure S36: ^{13}C{^{1}H}-APT NMR spectrum of **[CN$^{t\mathrm{Bu}}$TeCl$_2$]SbF$_6$** in CD_3CN (125.6 MHz).

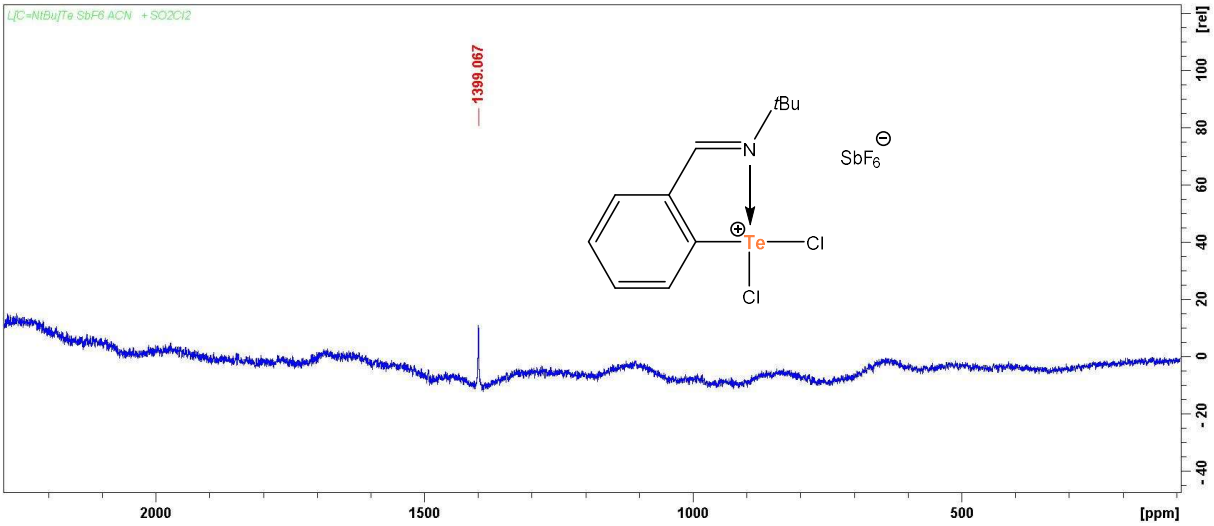

Figure S37: ^{125}Te{^{1}H} NMR spectrum of **[CN$^{t\mathrm{Bu}}$TeCl$_2$]SbF$_6$** in CD_3CN (158.0 MHz).

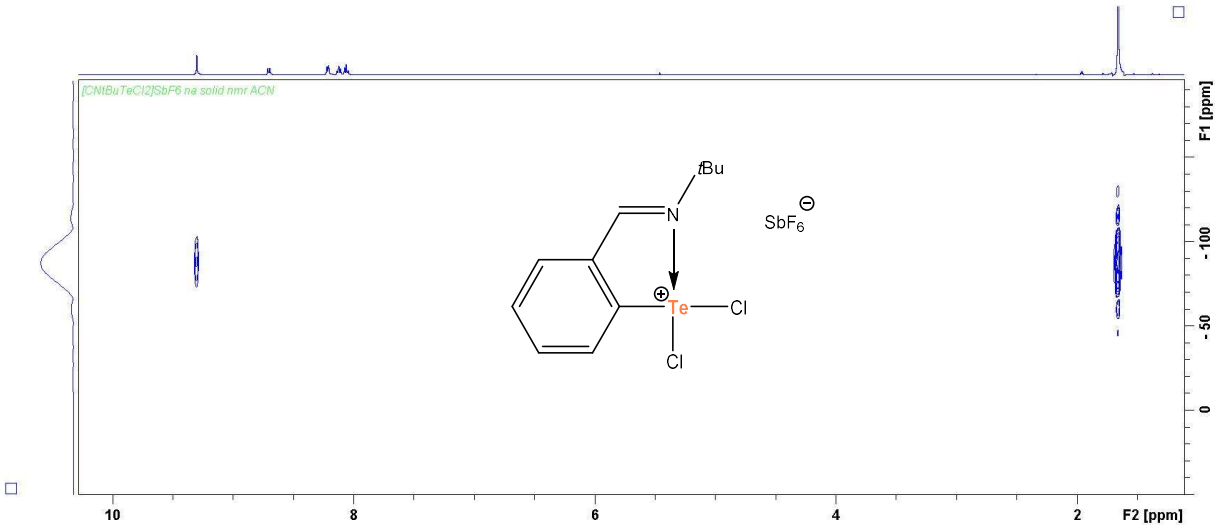

Figure S38: $^{15}N,^{1}H$ HMBC NMR spectrum of **[CN^{tBu}TeCl$_2$]SbF$_6$** in CD_3CN.

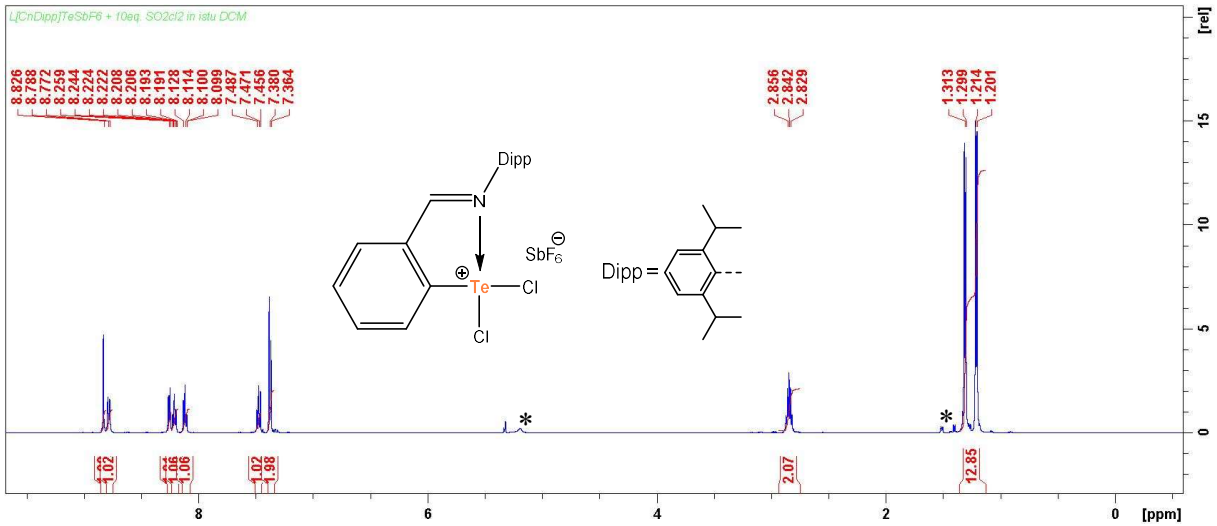

Figure S35: ^{1}H NMR spectrum of *in situ* prepared sample of **[CN^{Dipp}TeCl$_2$]SbF$_6$** in CD_2Cl_2 (500 MHz). *unknown minor impurity

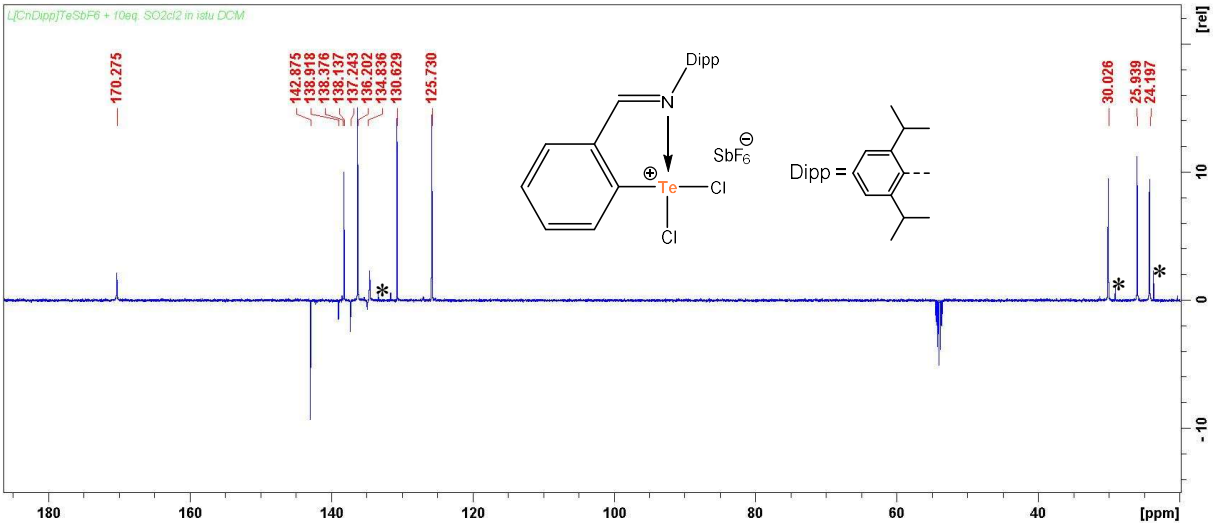

Figure S36: $^{13}C\{^{1}H\}$-APT NMR spectrum of *in situ* prepared sample of **[CN^{Dipp}TeCl$_2$]SbF$_6$** in CD_2Cl_2 (125.6 MHz). *denotes unknown minor impurities

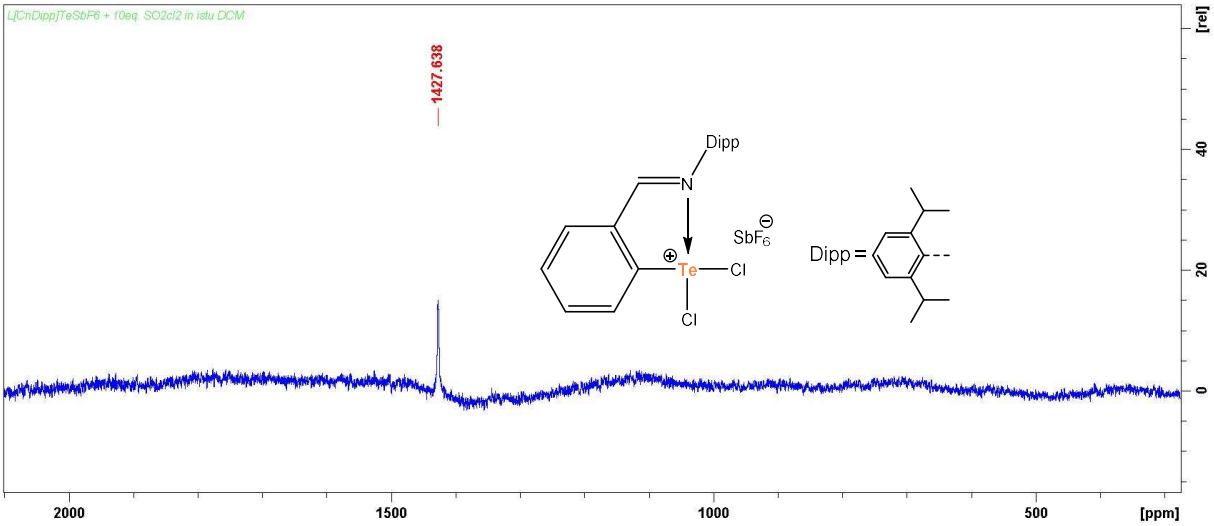

Figure S37: $^{125}Te\{^{1}H\}$ NMR spectrum of *in situ* prepared sample of **[CN^{Dipp}TeCl$_2$]SbF$_6$** in CD_2Cl_2 (158.0 MHz).

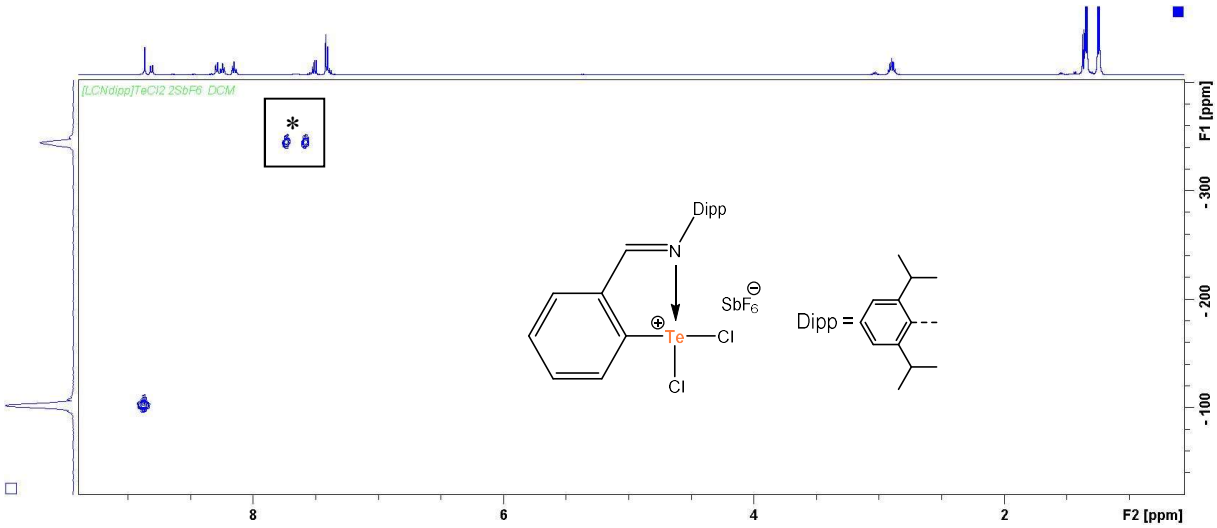

Figure S38: $^{15}N,^{1}H$ HMBC NMR spectrum of *in situ* prepared sample of **[CN^{Dipp}TeCl$_2$]SbF$_6$** in CD_2Cl_2. *denotes minor unknown impurity most probably result of starting hydrolysis as the signal corresponds to an NH group.

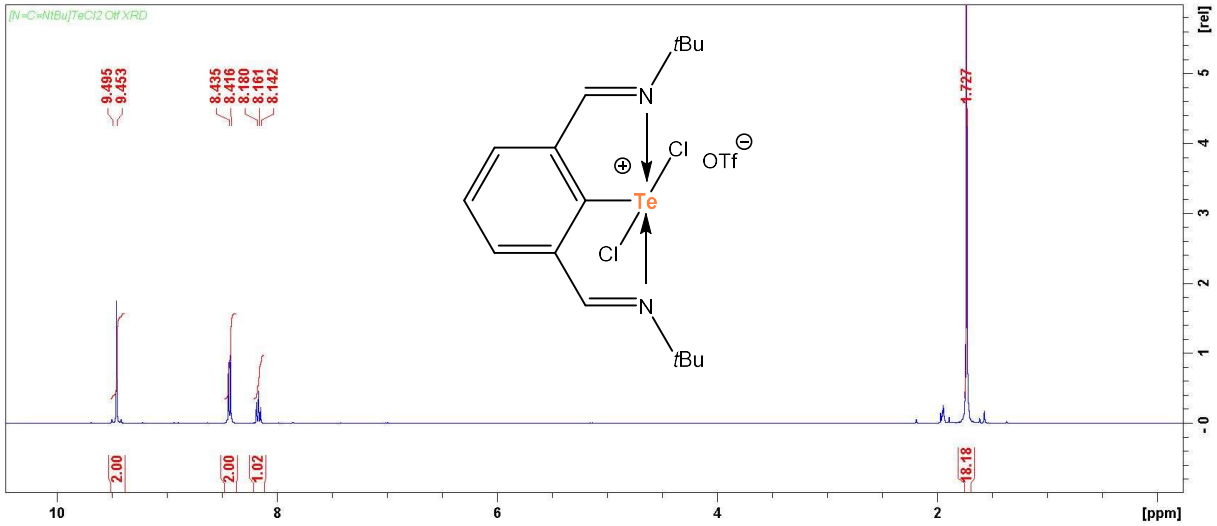

Figure S39: ^{1}H NMR spectrum of **[NCN^{tBu}TeCl$_2$]OTf** in CD_3CN (400 MHz).

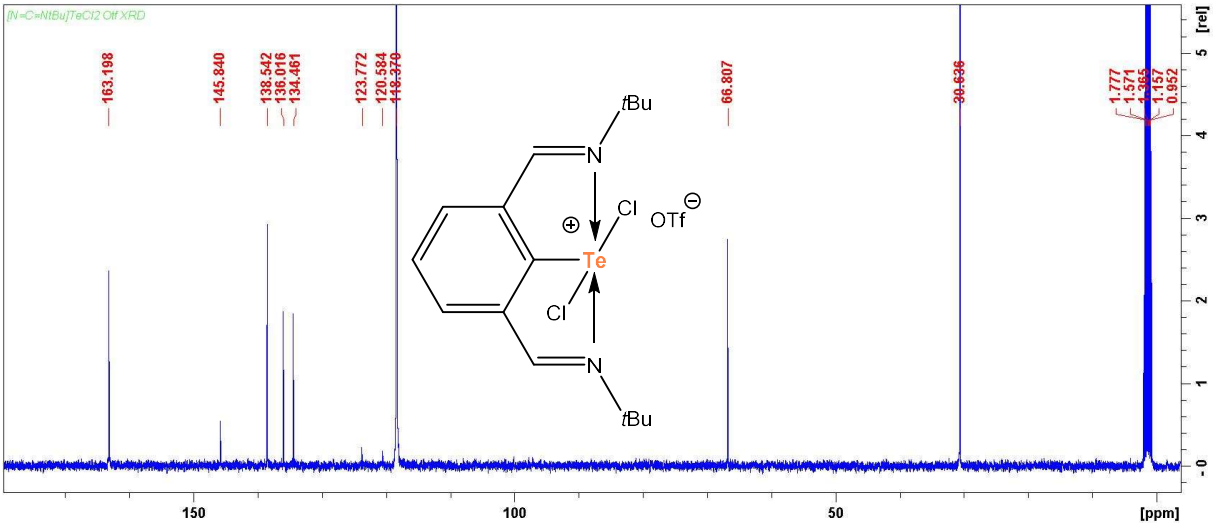

Figure S40: $^{13}C\{^{1}H\}$-APT NMR spectrum of **[NCN^{tBu}TeCl$_2$]OTf** in CD_3CN (125.6 MHz).

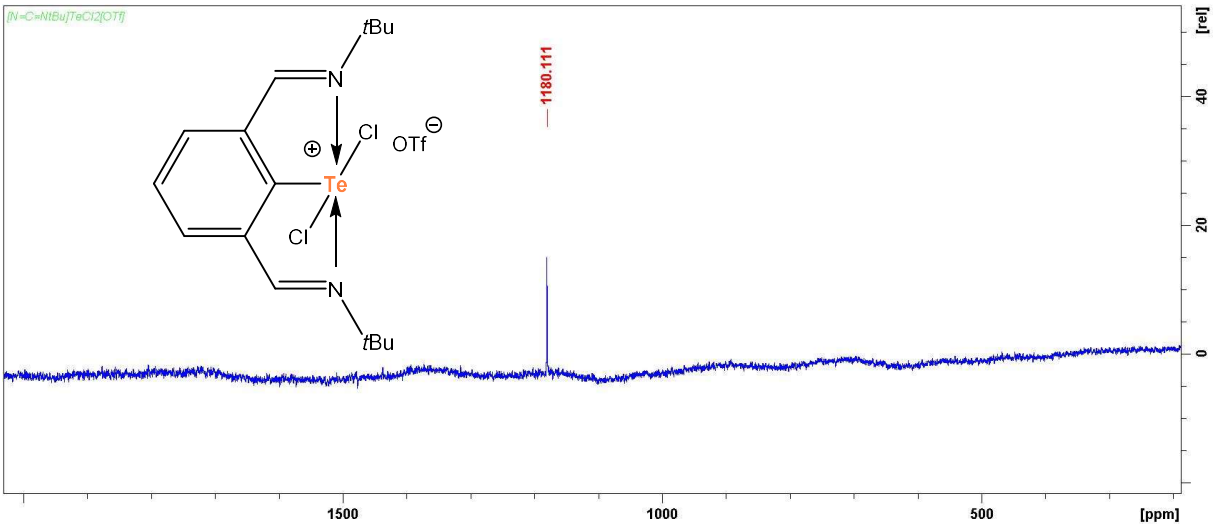

Figure S41: $^{125}Te\{^{1}H\}$ NMR spectrum of **[NCN^{tBu}TeCl$_2$]OTf** in CD_3CN (158.0 MHz).

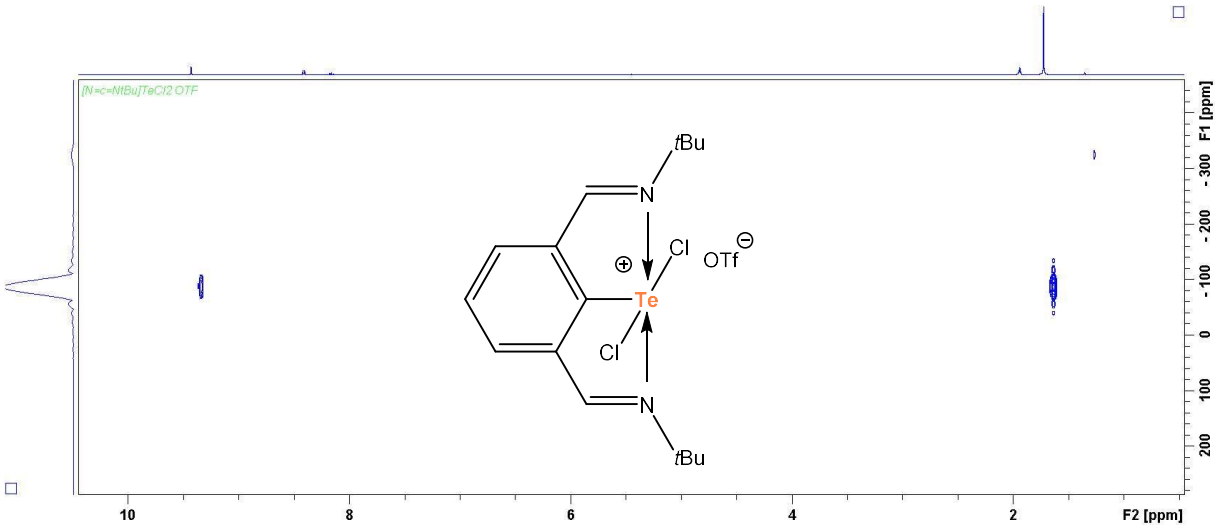

Figure S42: $^{15}N,^{1}H$ HMBC NMR spectrum of **[NCN^{tBu}TeCl$_2$]OTf** in CD_3CN.

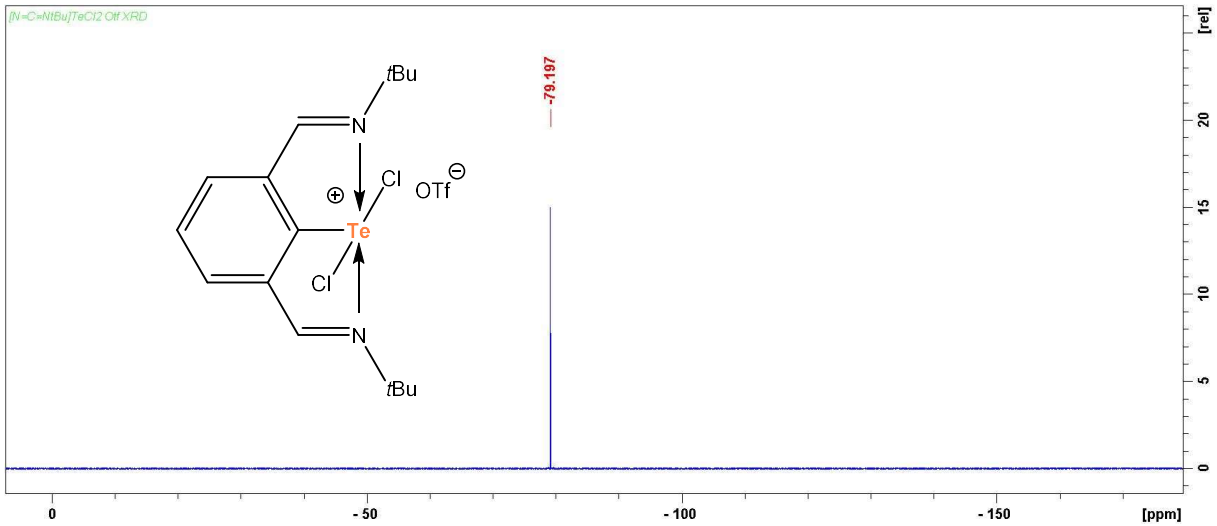

Figure S43: $^{19}F\{^{1}H\}$ NMR spectrum of **[CN^{tBu}TeCl$_2$]OTf** in CD_3CN (376.5 MHz).

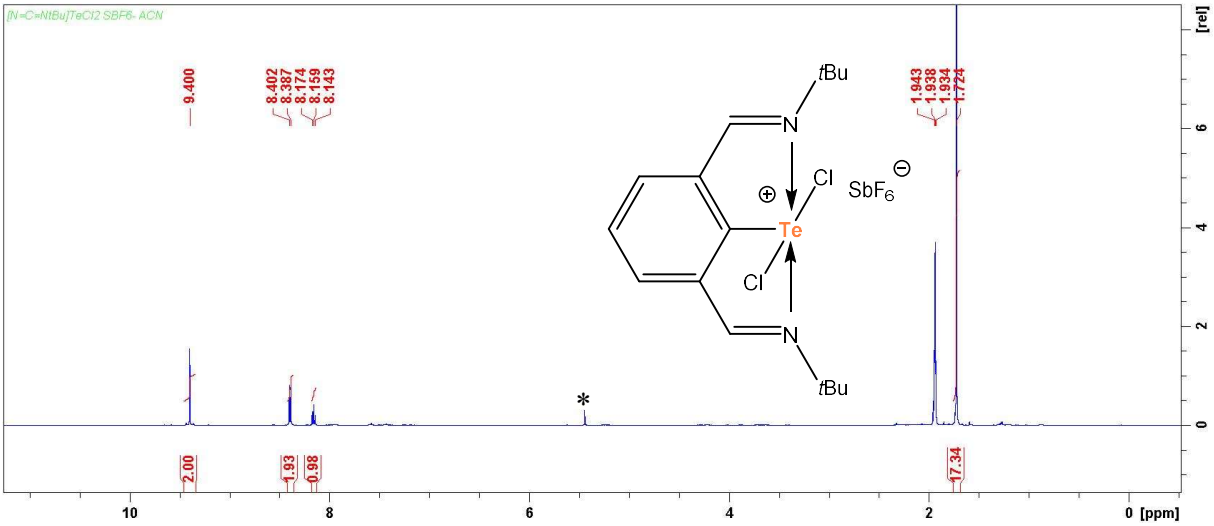

Figure S44: ^{1}H NMR spectrum of **[NCN^{tBu}TeCl$_2$]SbF$_6$** in CD_3CN (400 MHz). *denotes traces of dichloromethane.

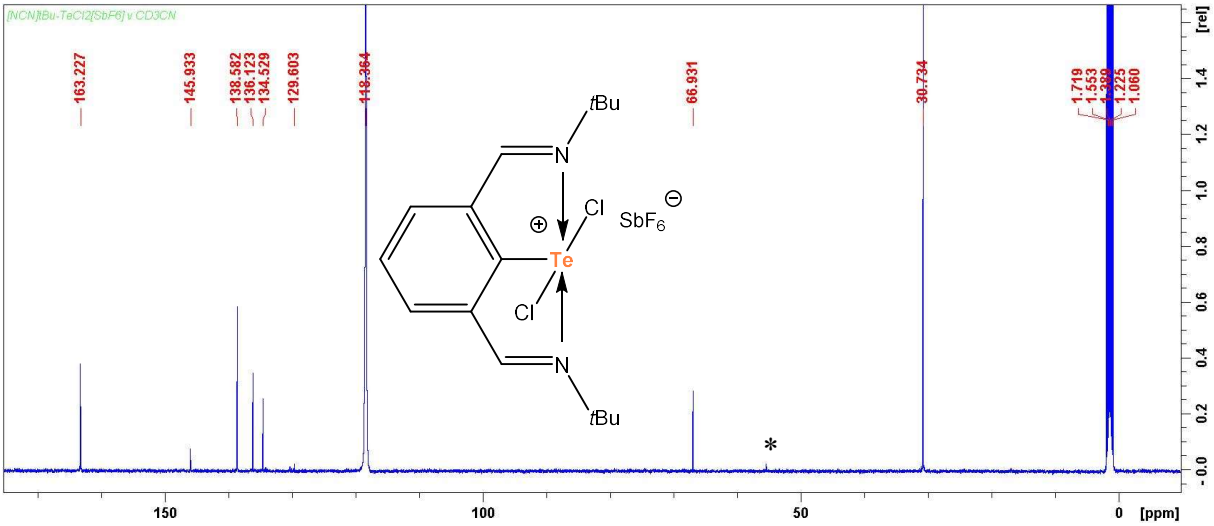

Figure S45: ^{13}C{^{1}H} NMR spectrum of **[NCN^{tBu}TeCl$_2$]SbF$_6$** in CD_3CN (125.6 MHz). *denotes traces of dichloromethane.

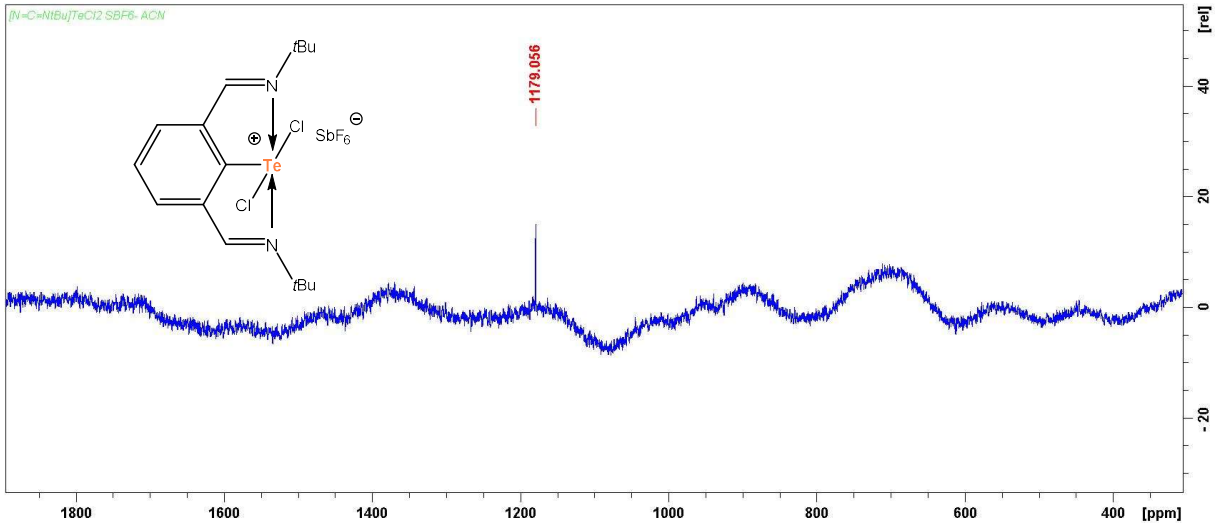

Figure S46: ^{125}Te{^{1}H} NMR spectrum of **[NCN$^{t\mathrm{Bu}}$TeCl$_2$]SbF$_6$** in CD_3CN (158.0 MHz).

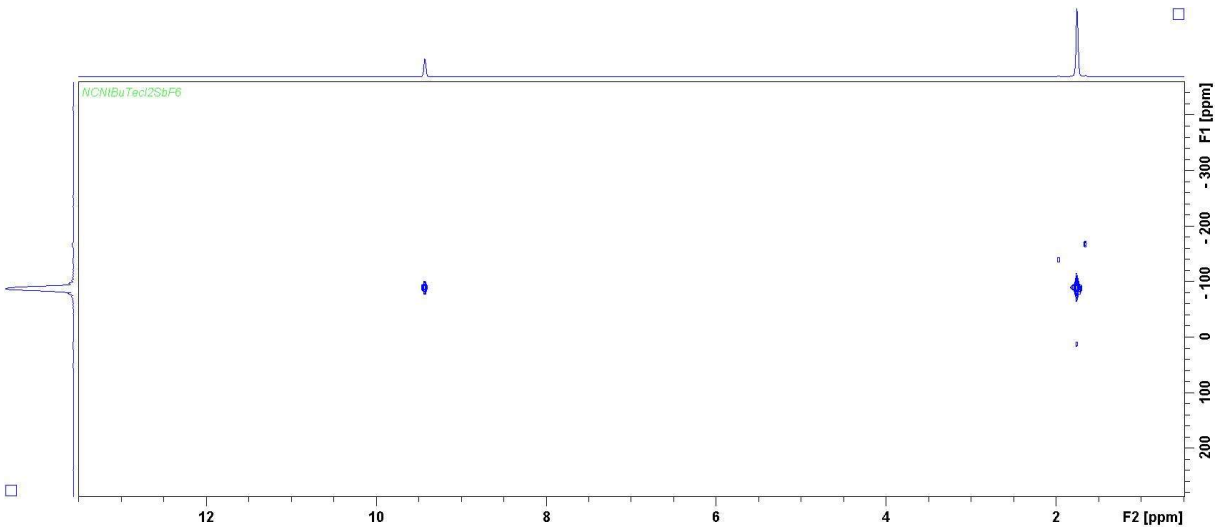

Figure S47: ^{15}N,^{1}H HMBC NMR spectrum of **[NCN$^{t\mathrm{Bu}}$TeCl$_2$]SbF$_6$** in CD_3CN.

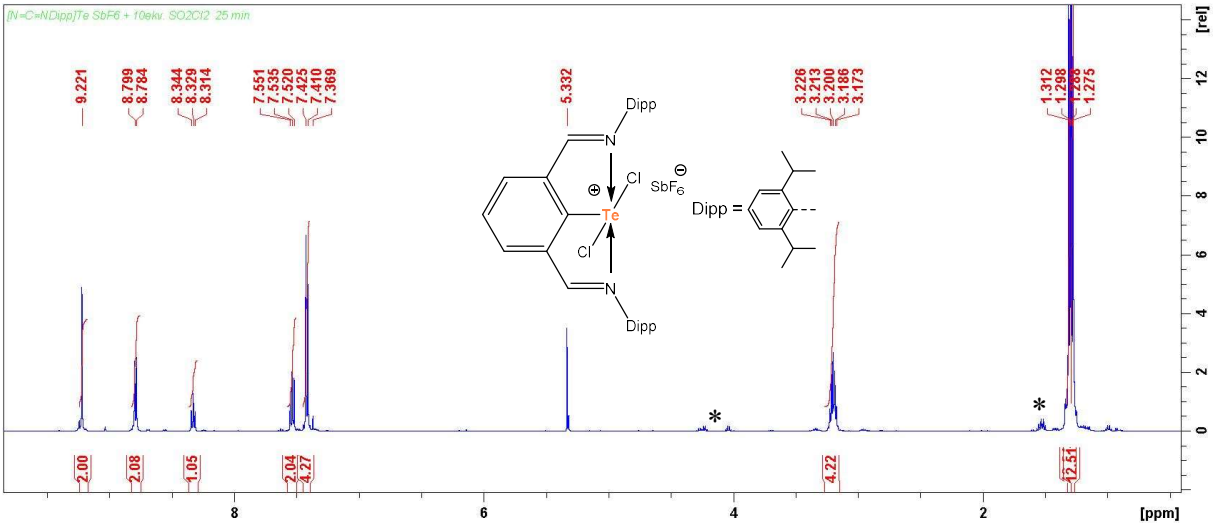

Figure S48: ^{1}H NMR spectrum of *in situ* prepared sample of **[NCN^{Dipp}TeCl$_2$]SbF$_6$** in CD_2Cl_2 (500 MHz). *denotes minor unknown impurities

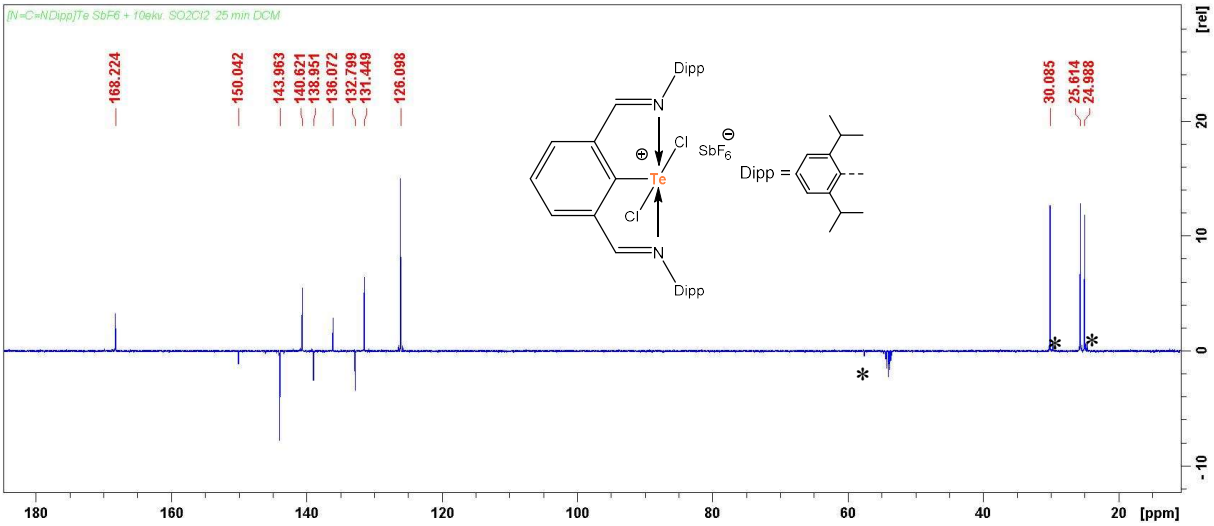

Figure S49: ^{13}C{^{1}H}-APT NMR spectrum of *in situ* prepared sample of **[NCN^{Dipp}TeCl$_2$]SbF$_6$** in CD_2Cl_2 (125.6 MHz). *denotes minor unknown impurities

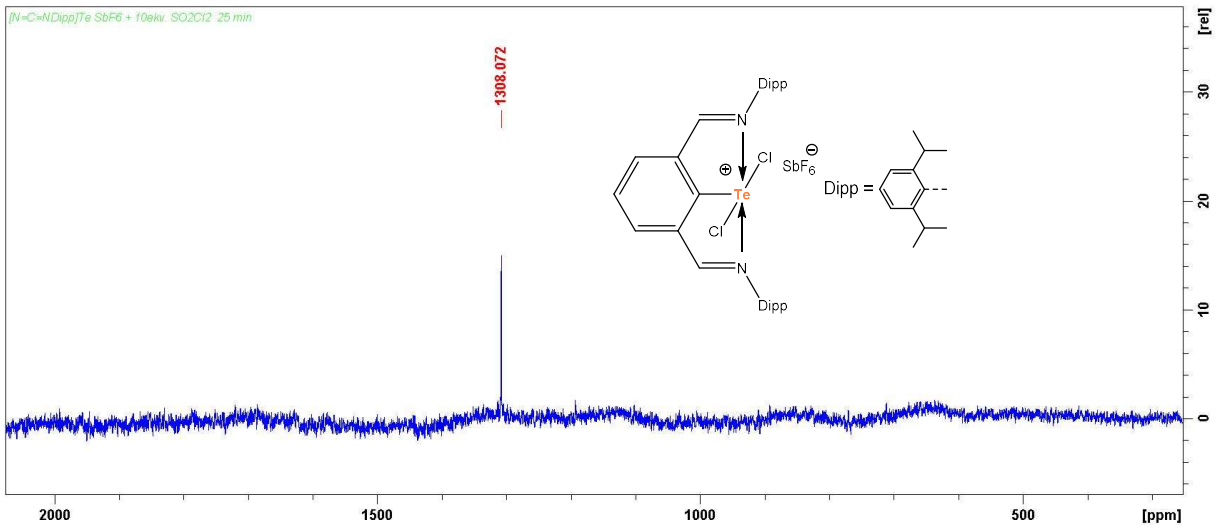

Figure S50: ^{125}Te{^{1}H} NMR spectrum of *in situ* prepared sample of **[NCN^{Dipp}TeCl$_2$]SbF$_6$** in CD_2Cl_2 (158.0 MHz).

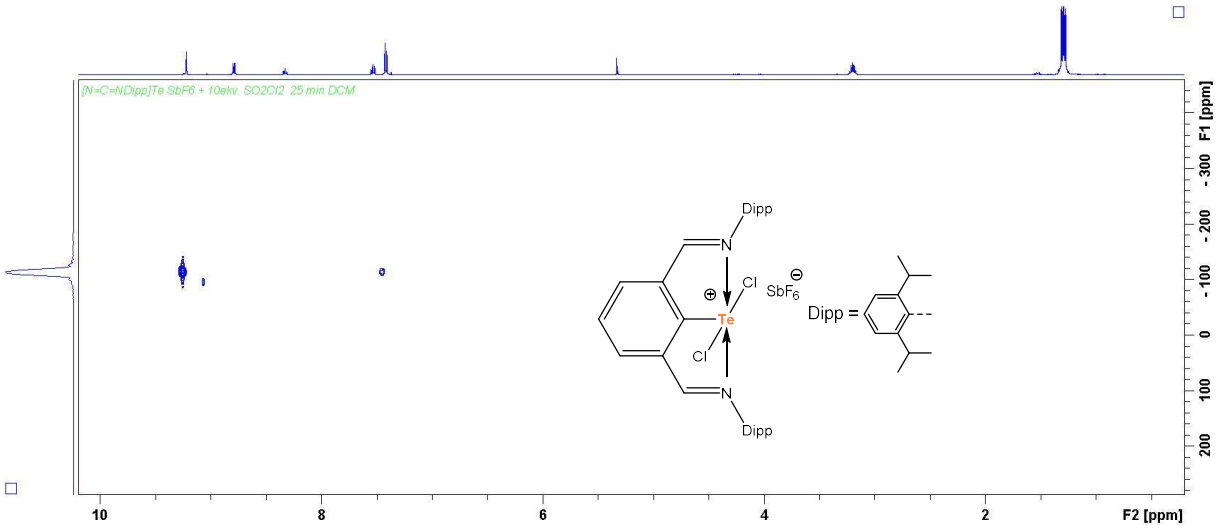

Figure S51: ^{15}N,^{1}H HMBC NMR spectrum of *in situ* prepared sample of **[NCN^{Dipp}TeCl$_2$]SbF$_6$** in CD_2Cl_2.

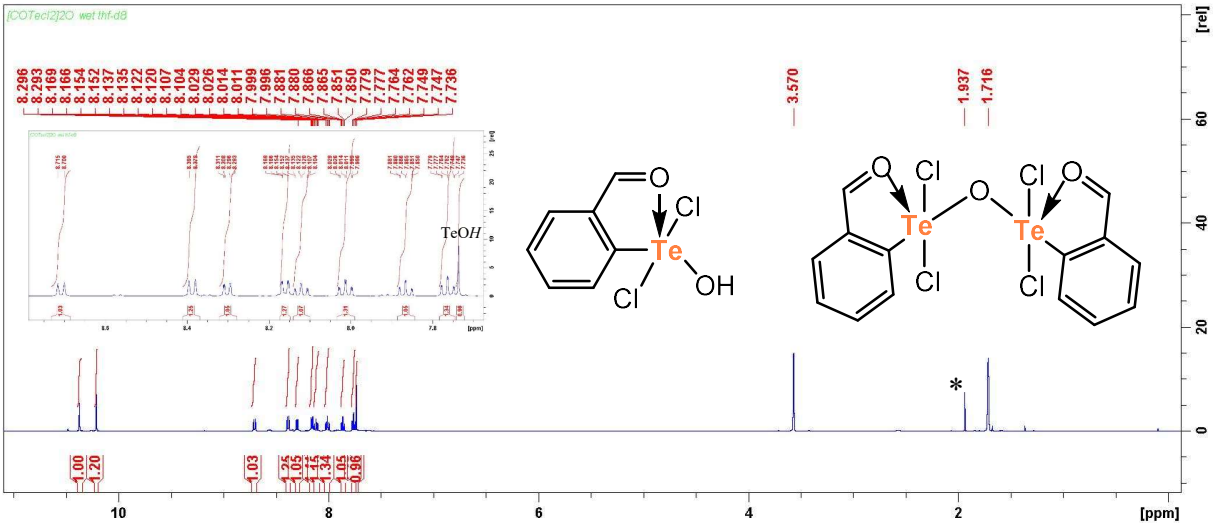

Figure S52: ^{1}H NMR spectrum of single-crystals of **[COTeCl$_2$]$_2$O** in thf-d8 (not dried) (500 MHz). *denotes traces of acetonitrile.

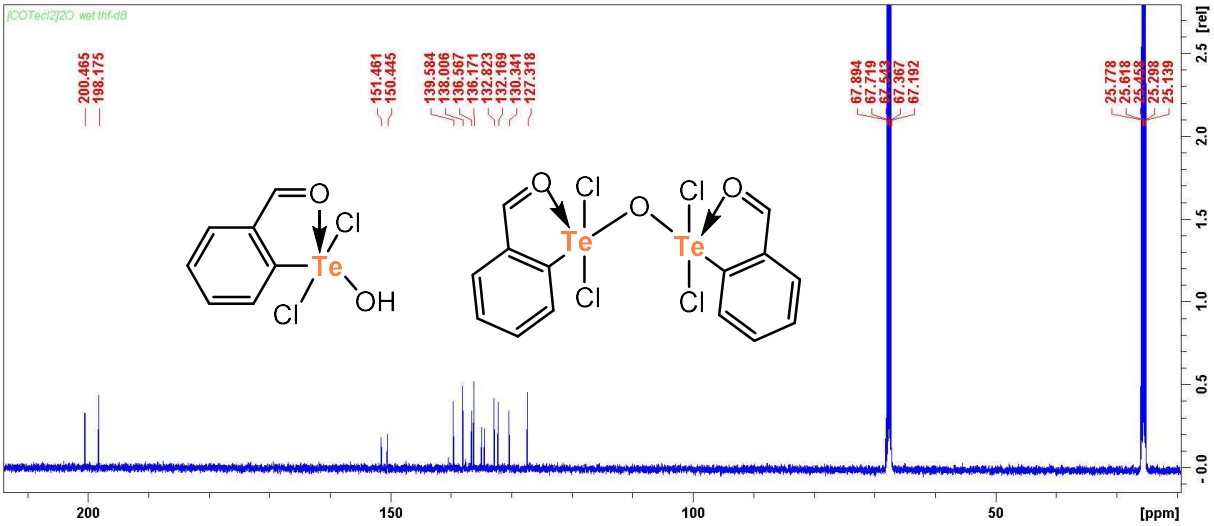

Figure S53: ^{13}C{^{1}H} NMR of single-crystals of **[COTeCl$_2$]$_2$O** in thf-d8 (not dried) (125.6 MHz).

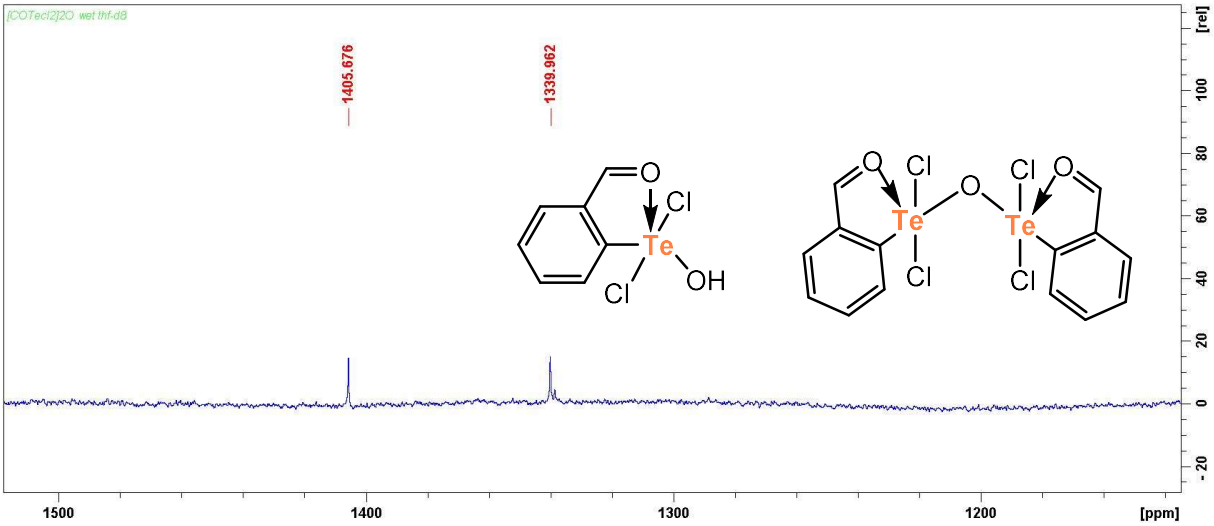

Figure S54: ^{125}Te{^{1}H} NMR spectrum of single-crystals of **[COTeCl$_2$]$_2$O** in thf-d8 (not dried) (158 MHz).

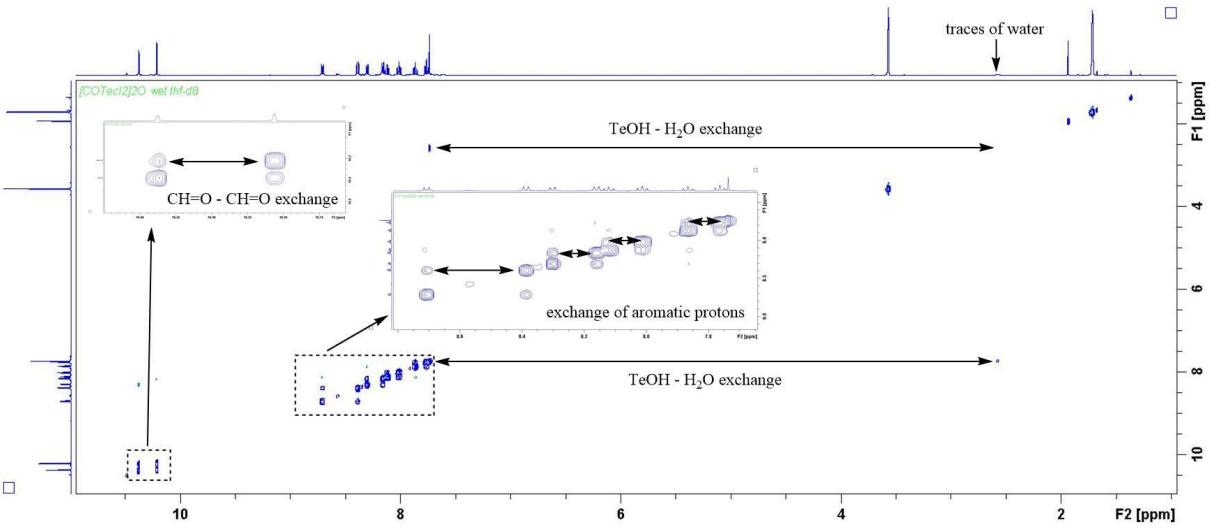

Figure S55: ^{1}H, ^{1}H EXSY NMR spectrum (mixing time 1s) of single-crystals of **[COTeCl$_2$]$_2$O** in thf-d8 (not dried) showing mutual exchange between **[COTeCl$_2$]$_2$O** and **[COTeCl$_2$]OH** and traces amount of water (500 MHz).

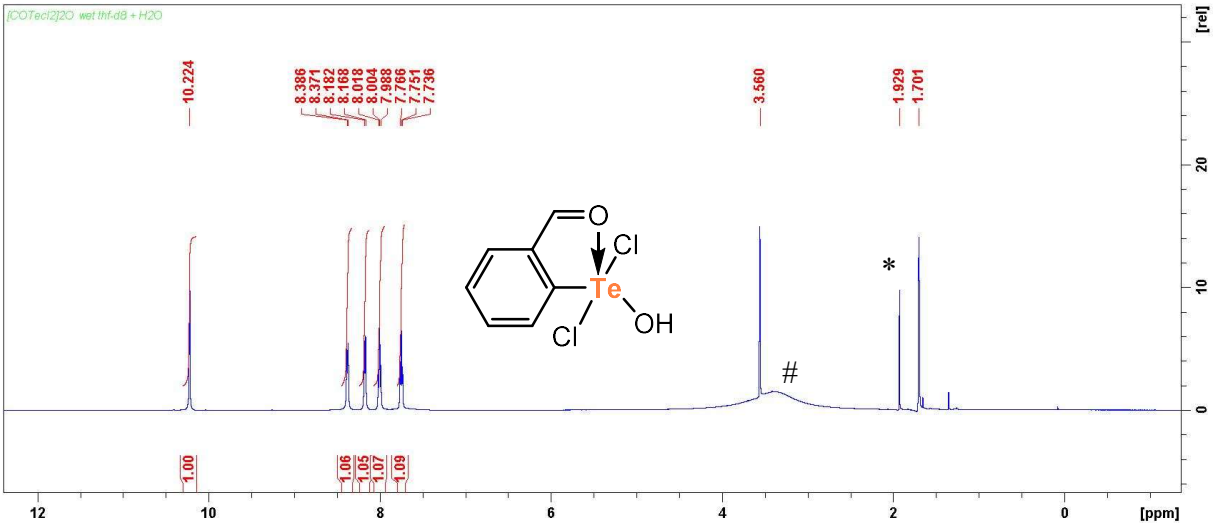

Figure S56: ^{1}H NMR spectrum obtained after dissolving of single-crystals of **[COTeCl$_2$]$_2$O** in thf-d8 and addition of 10 µL of water showing the presence of **[COTeCl$_2$]OH** only (500 MHz). *denotes traces of acetonitrile and # signal of water added. Note: the signal of Te-OH disappeared probably due to the fast exchange with water.

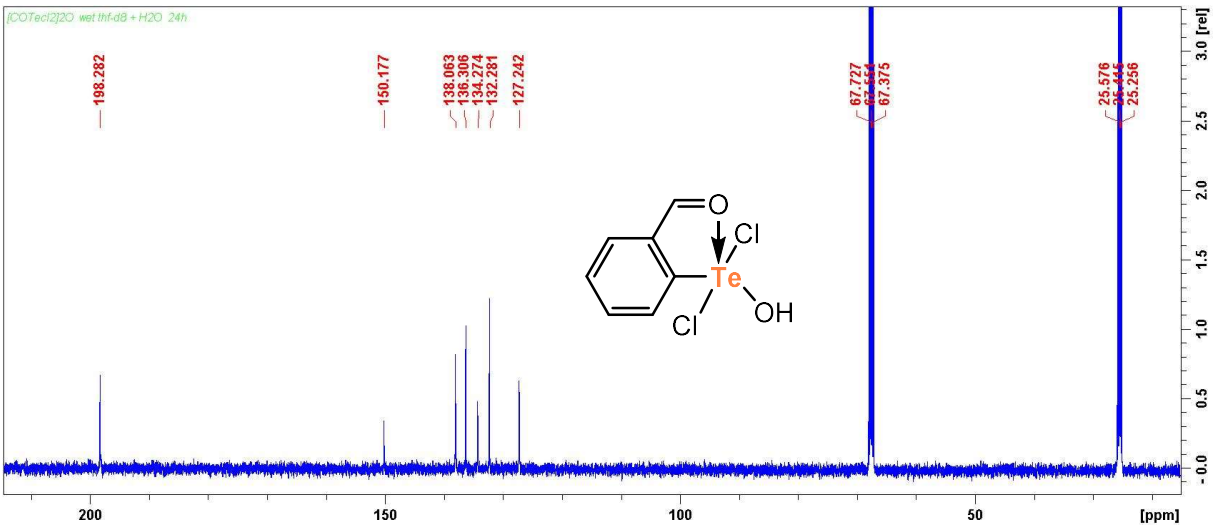

Figure S57: ^{13}C{^{1}H} NMR spectrum obtained after dissolving of single-crystals of **[COTeCl$_2$]$_2$O** in thf-d8 and addition of 10 µL of water showing the presence of **[COTeCl$_2$]OH** only (125.6 MHz).

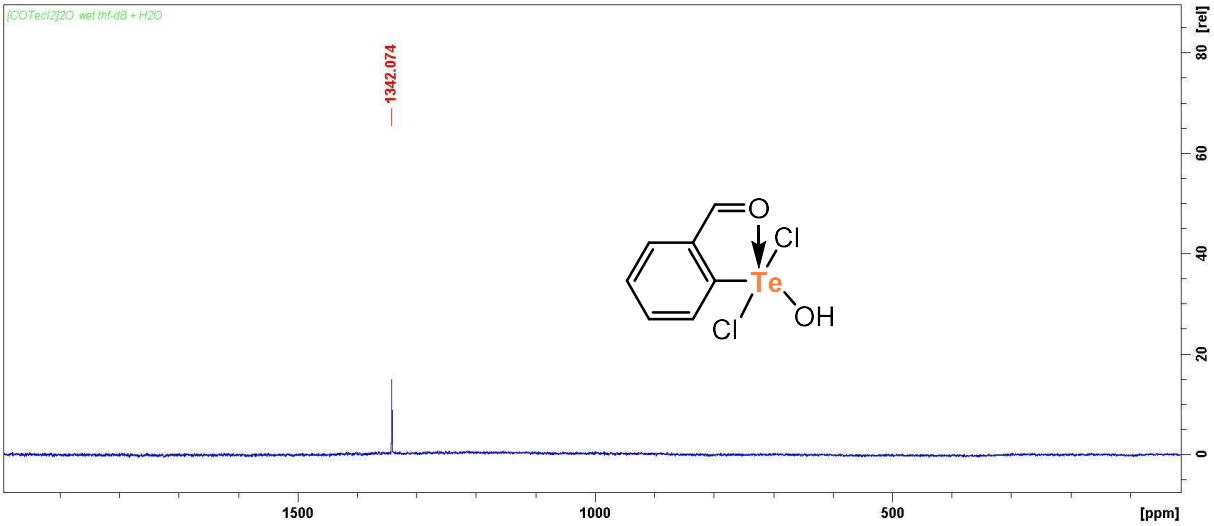

Figure S58: ^{125}Te{^{1}H} NMR spectrum obtained after dissolving of single-crystals of **[COTeCl$_2$]$_2$O** in thf-d8 and addition of 10 µL of water showing the presence of **[COTeCl$_2$]OH** only (158 MHz).

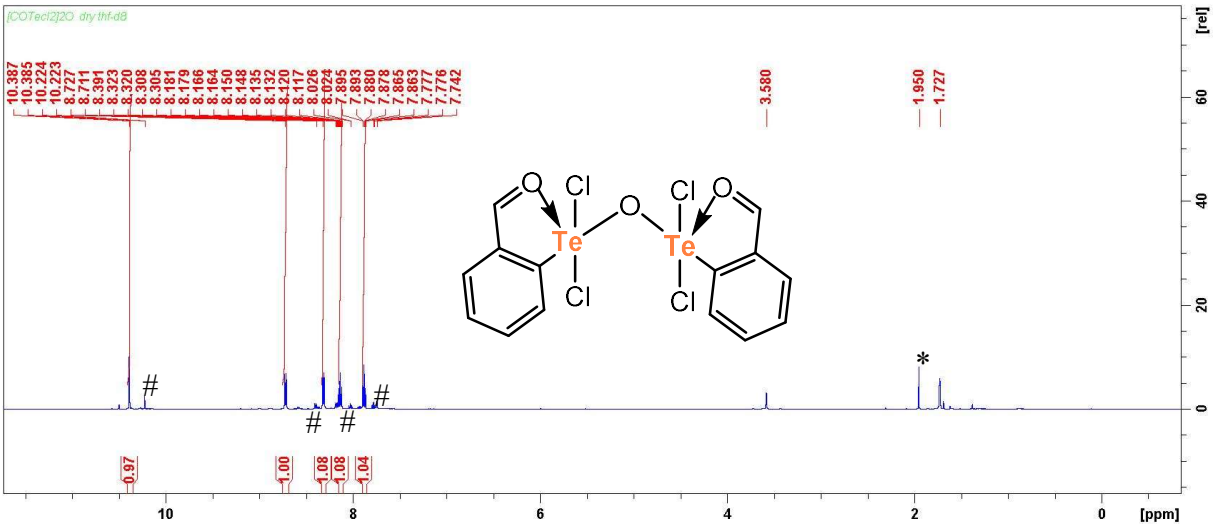

Figure S59: ^{1}H NMR spectrum of single-crystals of **[COTeCl$_2$]$_2$O** in thf-d8 (dried) (500 MHz). The signals of traces of **[COTeCl$_2$]OH** are still present ($^{\#}$). *denotes traces of acetonitrile.

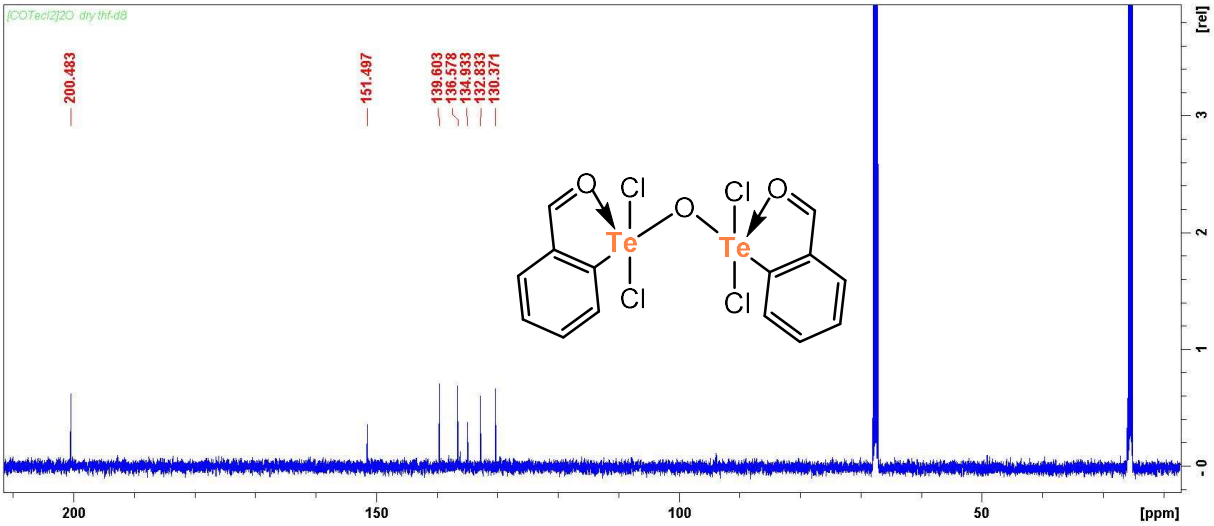

Figure S60: $^{13}C\{^{1}H\}$ NMR spectrum of single-crystals of **[COTeCl$_2$]$_2$O** in thf-d8 (dried) (125.6 MHz).

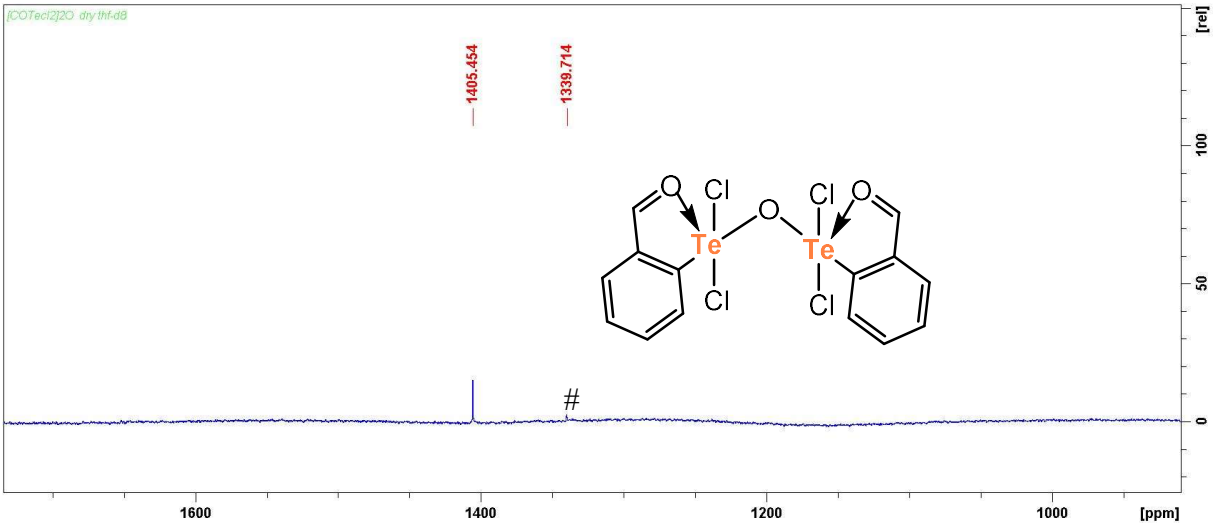

Figure S61: $^{125}Te\{^{1}H\}$ NMR spectrum of single-crystals of **[COTeCl$_2$]$_2$O** in thf-d8 (dried) (158 MHz). The signal of traces of **[COTeCl$_2$]OH** is still present ($^{\#}$).

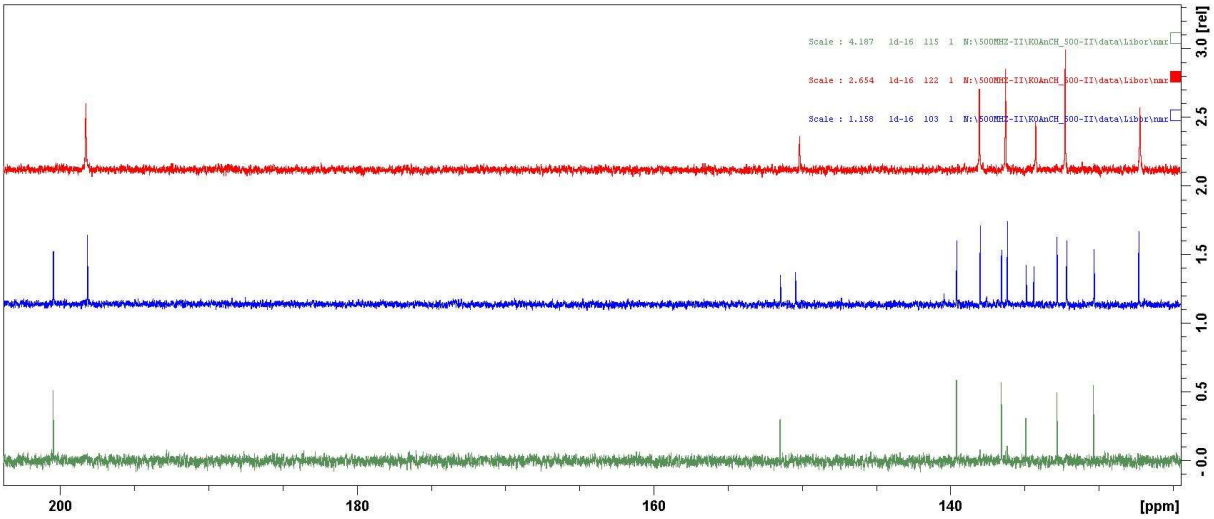

Figure S62: Comparison of $^{13}C\{^{1}H\}$ NMR spectra of **[COTeCl$_2$]$_2$O** in thf-d8 (dried, top) *vs*. mixture of **[COTeCl$_2$]$_2$O** and **[COTeCl$_2$]OH** in thf-d8 (wet, middle) *vs*. **[COTeCl$_2$]OH** in thf-d8 (wet+H_2O, bottom) (125.6 MHz).

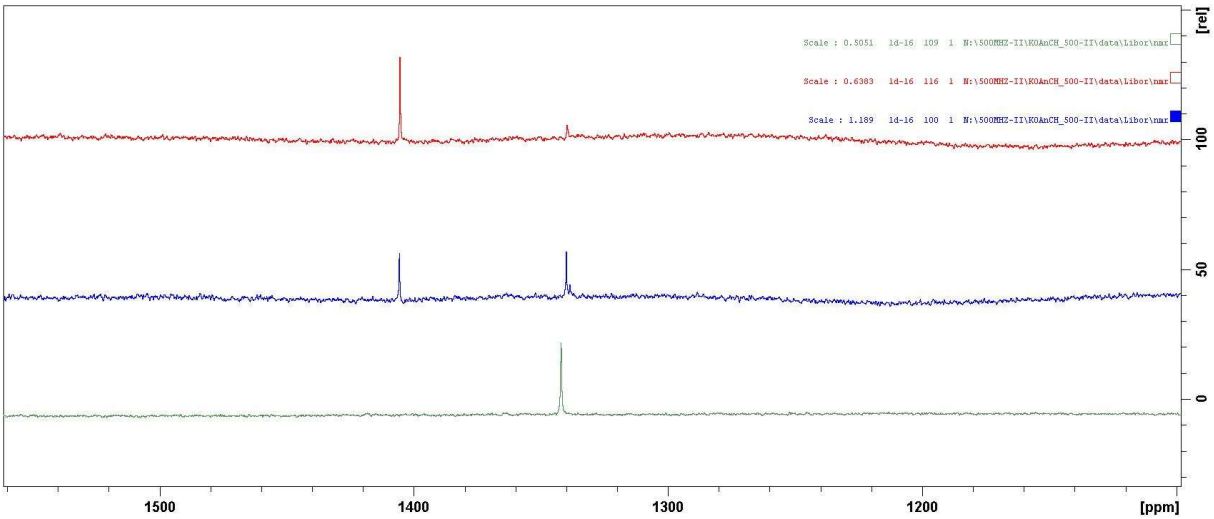

Figure S63: Comparison of $^{125}Te\{^{1}H\}$ NMR spectra of **[COTeCl$_2$]$_2$O** in thf-d8 (dried, top) vs. mixture of **[COTeCl$_2$]$_2$O** and **[COTeCl$_2$]OH** in thf-d8 (wet, middle) vs **[COTeCl$_2$]OH** in thf-d8 (wet+H_2O, bottom) (125.6 MHz).

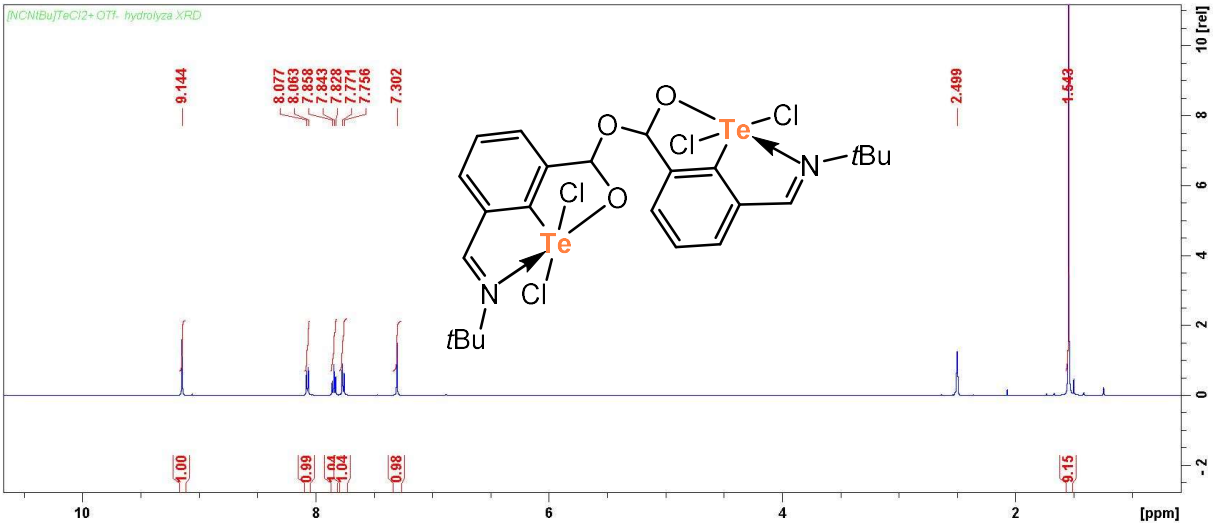

Figure S64: ^{1}H NMR spectrum of single-crystals of **[OCN^{tBu}TeCl$_2$]$_2$O** in dmso-d6 (dried) (500 MHz).

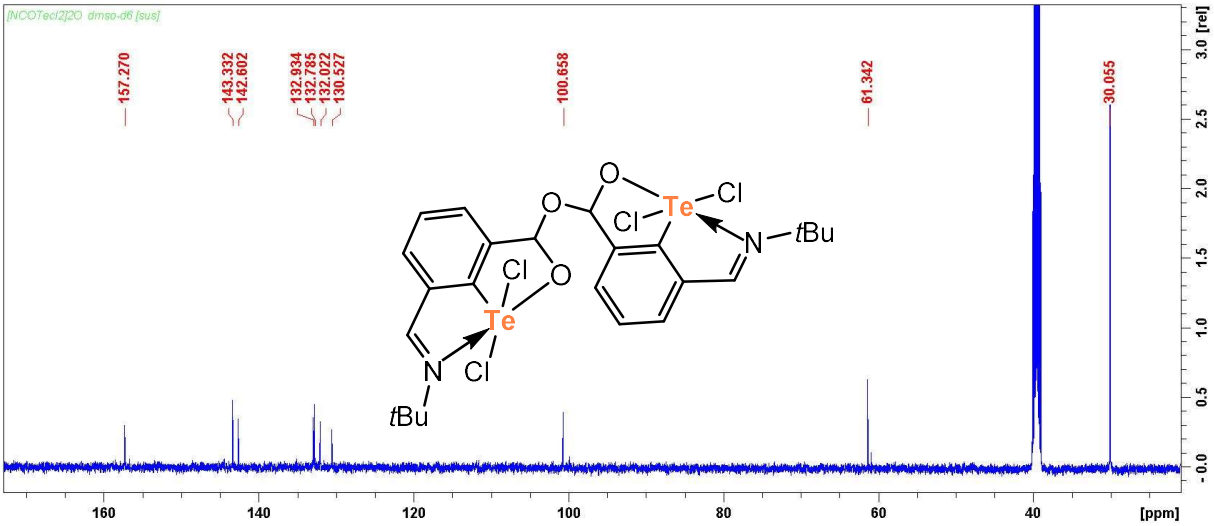

Figure S65: ^{13}C{^{1}H} NMR spectra of **[OCN^{tBu}TeCl$_2$]$_2$O** in dmso-d6 (dried) (125.6 MHz).

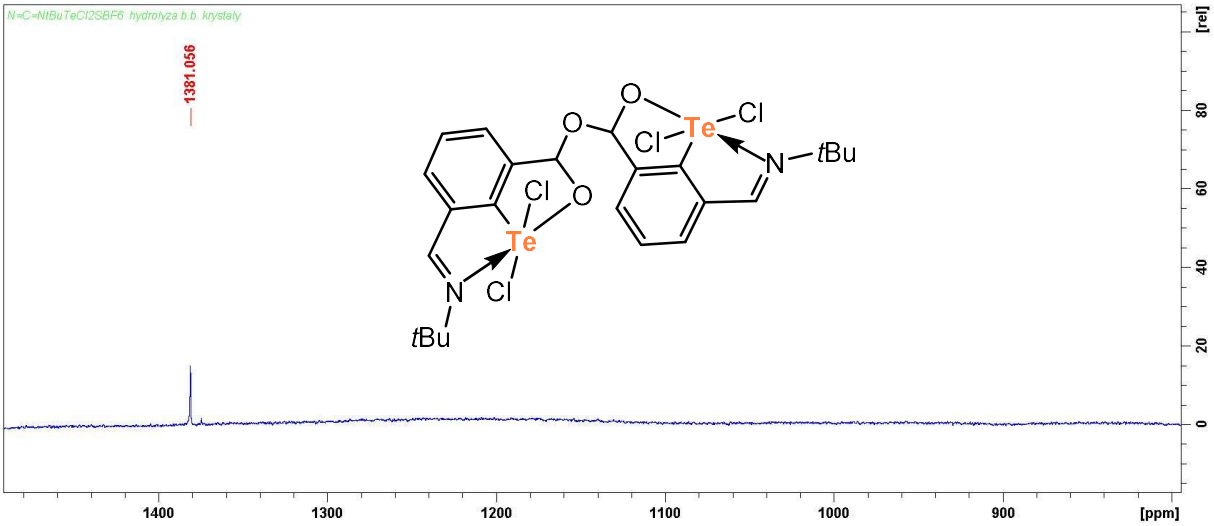

Figure S66: ^{125}Te{^{1}H} NMR spectra of **[OCN^{tBu}TeCl$_2$]$_2$O** in dmso-d6 (dried) (125.6 MHz).

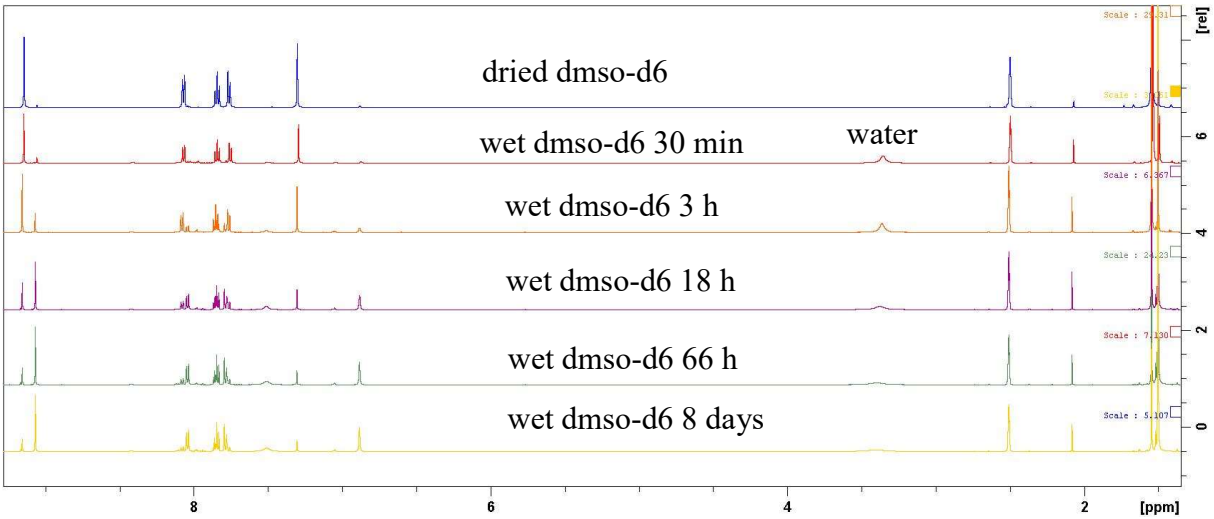

Figure S67: Comparison of ^{11}H NMR spectra of **[OCNTeCl$_2$]$_2$O** in (dried, top) *vs.* mixtures of **[OCNTeCl$_2$]$_2$O** and **[OCNTeCl$_2$]OH** formed in time in wet dmso-d6 (125.6 MHz).

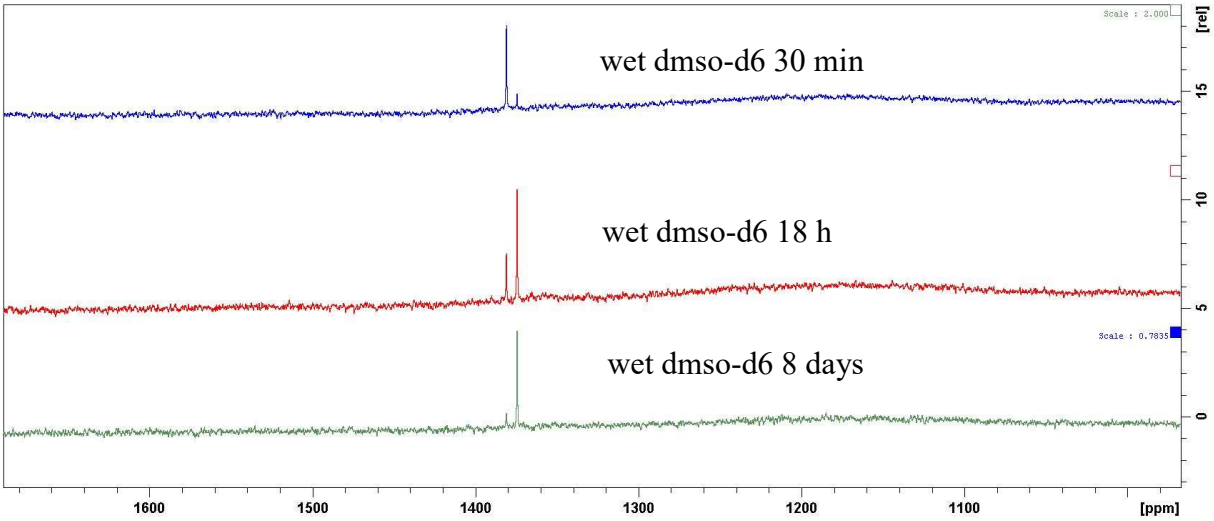

Figure S68: Comparison of ^{125}Te{^{1}H} NMR spectra showing transformation of **[OCNTeCl$_2$]$_2$O** to **[OCNTeCl$_2$]OH** formed in time in wet dmso-d6 (125.6 MHz).

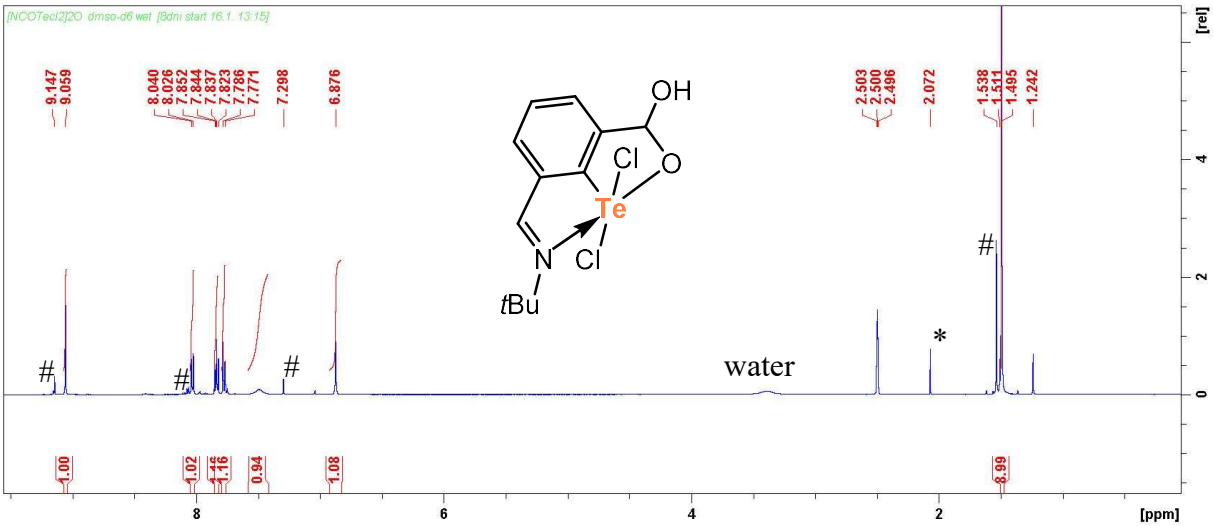

Figure S69: ^{1}H NMR spectrum of single-crystals of **[OCN$^{t\mathrm{Bu}}$TeCl$_2$]OH** in dmso-d6 (wet, 8 days) contaminated by traces of **[OCN$^{t\mathrm{Bu}}$TeCl$_2$]$_2$O** ($^{\#}$) (500 MHz). (*) traces of acetonitrile used in synthesis

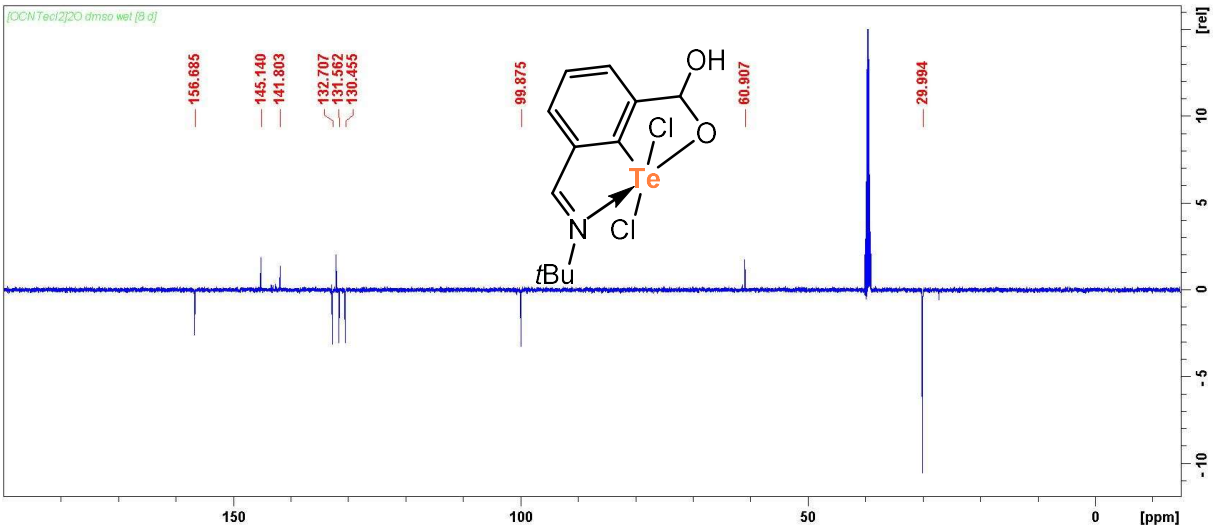

Figure S70: $^{13}C\{^{1}H\}$ NMR spectra of **[OCN^{tBu}TeCl$_2$]OH** in dmso-d6 (wet, 8 days) contaminated by traces of **[OCN^{tBu}TeCl$_2$]$_2$O** (125.6 MHz).

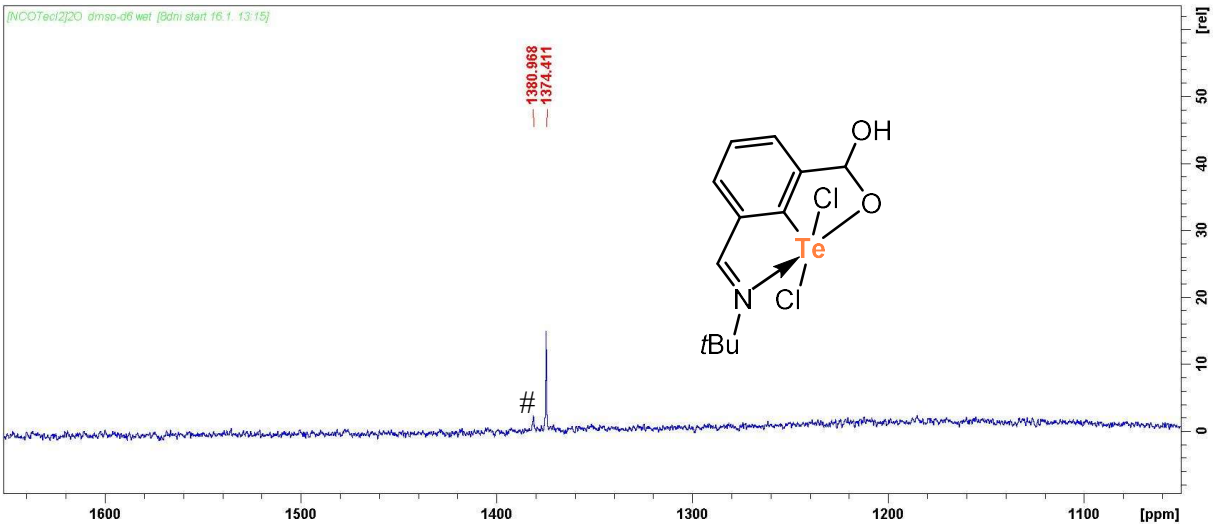

Figure S71: $^{125}Te\{^{1}H\}$ NMR spectra of **[OCN^{tBu}TeCl$_2$]OH** in dmso-d6 (wet, 8 days) contaminated by traces of **[OCN^{tBu}TeCl$_2$]$_2$O** ($^{\#}$) (125.6 MHz).

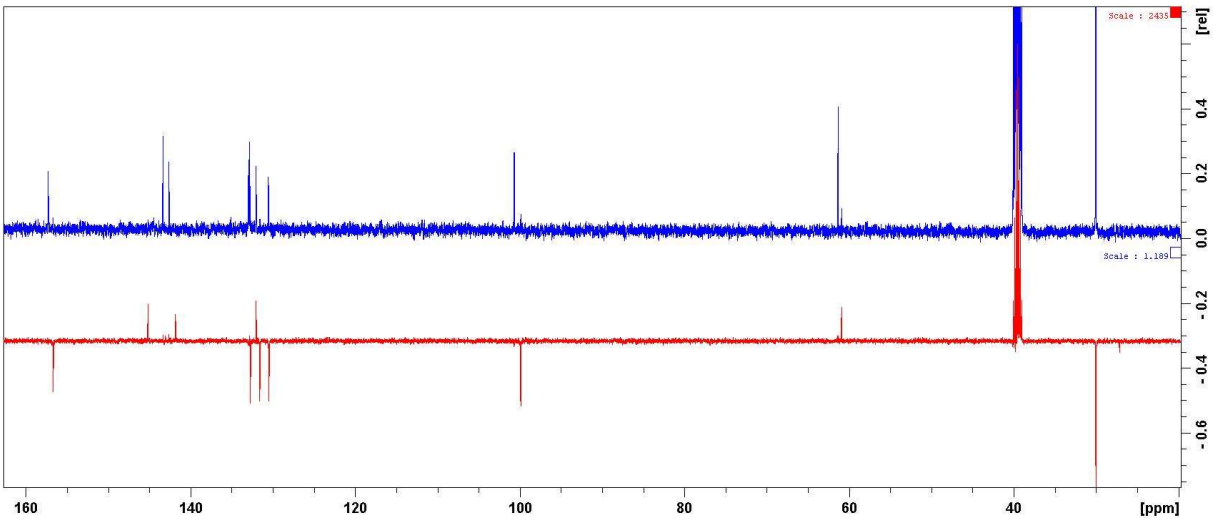

Figure S72: Comparison of $^{13}C\{^{1}H\}$ NMR spectra of **[OCNTeCl2]2O** in dmso-d6 (dried, top) and **[OCNTeCl2]OH** in dmso-d6 (wet, after 8 days) (125.6 MHz).

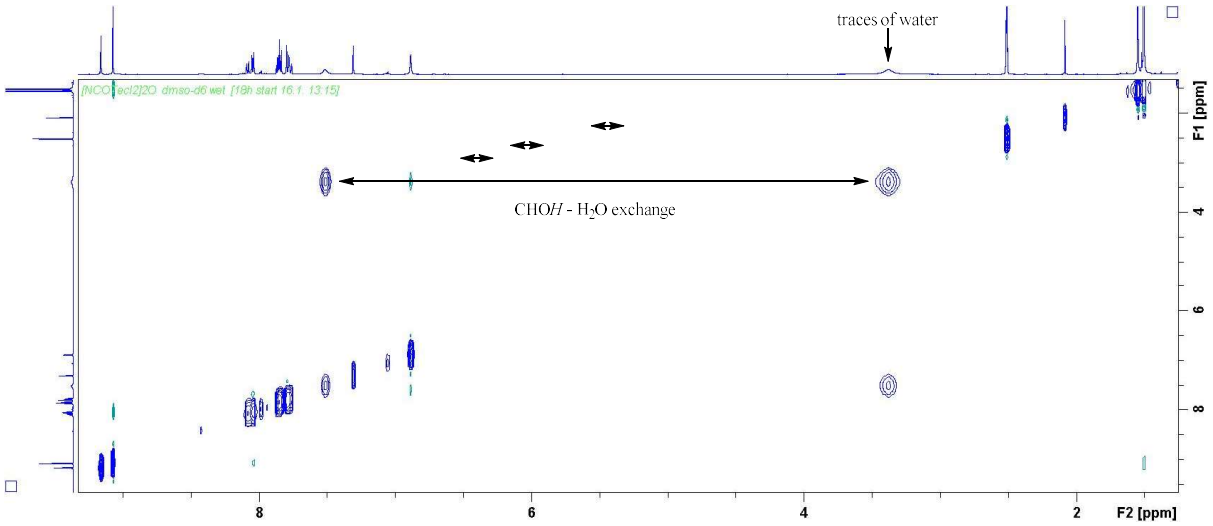

Figure S73: ^{1}H, ^{1}H EXSY NMR spectrum (mixing time 1s) of mixture of **[OCNTeCl2]2O** and **[OCNTeCl2]OH** (wet dmso-d6, 18h) and traces amount of water (500 MHz).

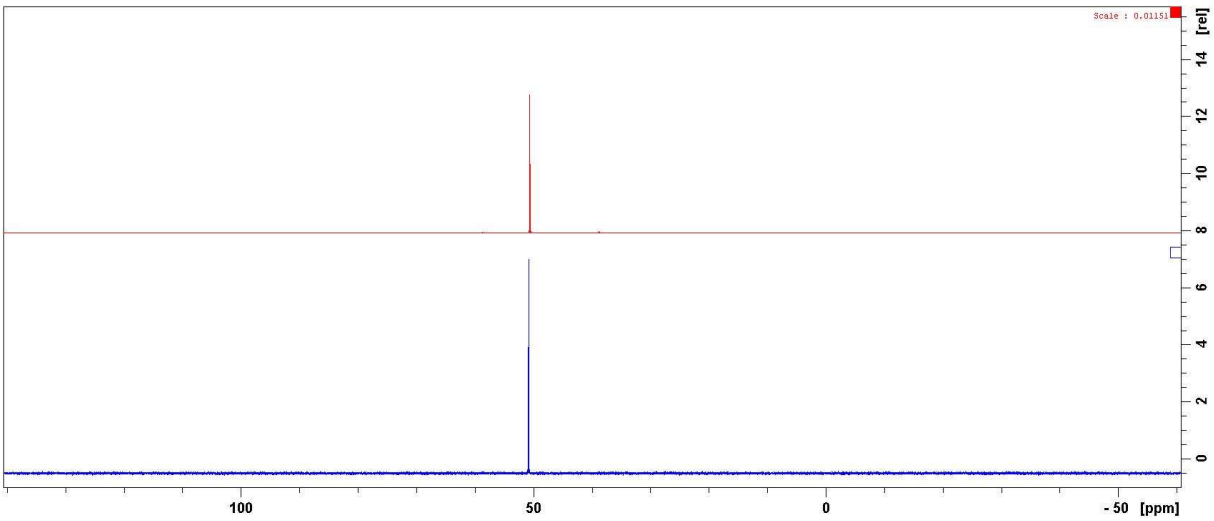

Figure S74: ^{31}P NMR spectra of Et_3PO (top) and its 1:5 molar mixture with **CN^{tBu}TeCl** in dichloromethane-d_2.

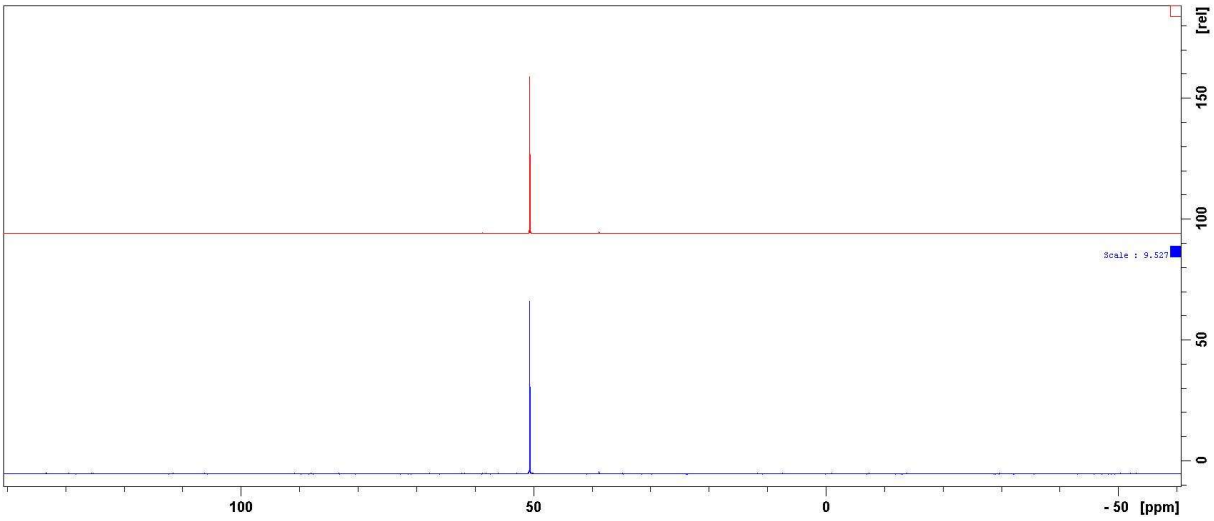

Figure S75: ^{31}P NMR spectra of Et_3PO (top) and its 1:5 molar mixture with **CN^{Dipp}TeCl** in dichloromethane-d_2.

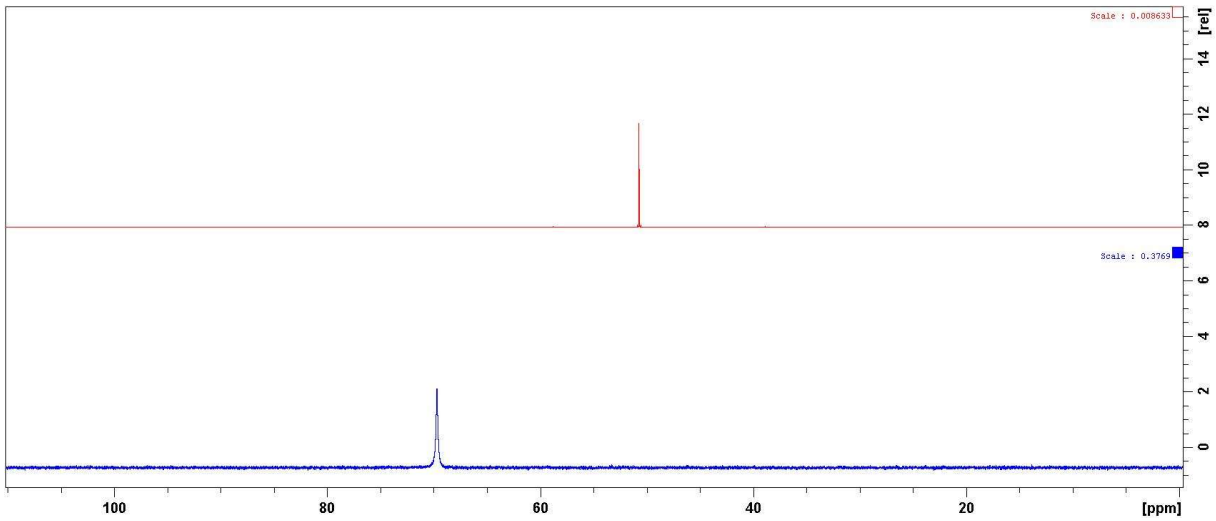

Figure S76: ^{31}P NMR spectra of Et_3PO (top) and its 1:5 molar mixture with **[CN^{tBu}Te]OTf** in dichloromethane-d_2.

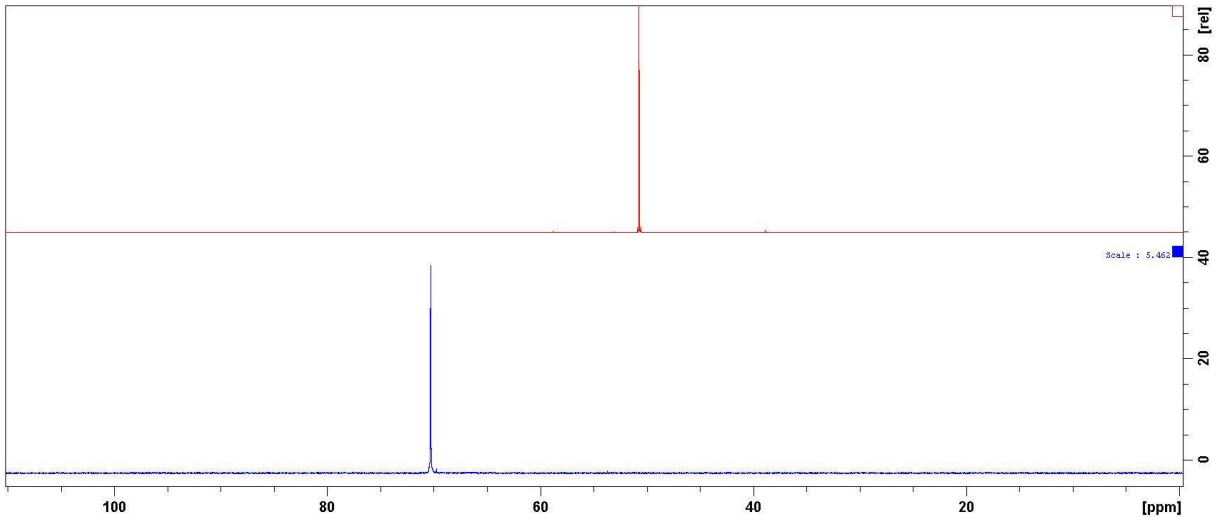

Figure S77: ^{31}P NMR spectra of Et_3PO (top) and its 1:5 molar mixture with **[CN^{tBu}Te]SbF$_6$** in dichloromethane-d_2.

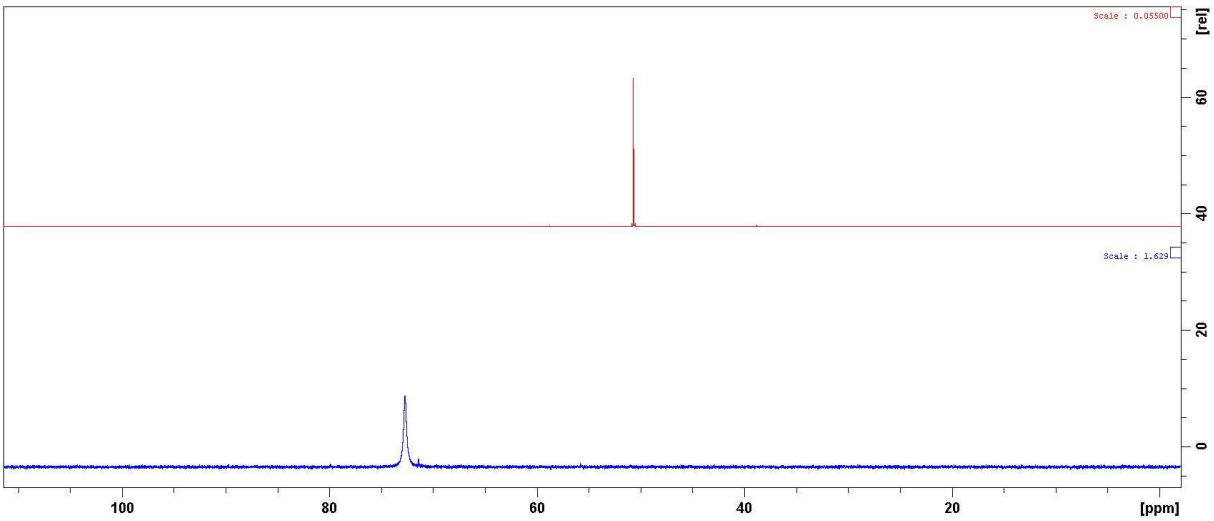

Figure S78: ^{31}P NMR spectra of Et_3PO (top) and its 1:5 molar mixture with **[CN^{Dipp}Te]SbF$_6$** in dichloromethane-d$_2$.

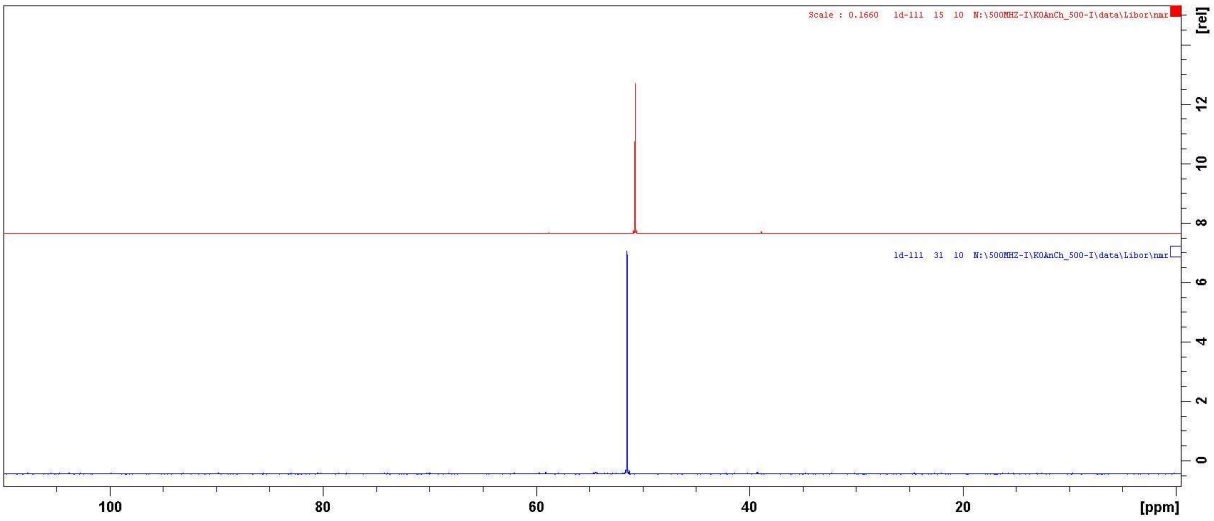

Figure S79: ^{31}P NMR spectra of Et_3PO (top) and its 1:5 molar mixture with **[CN^{Dipp}Te]SbF$_6$** in dichloromethane-d$_2$.

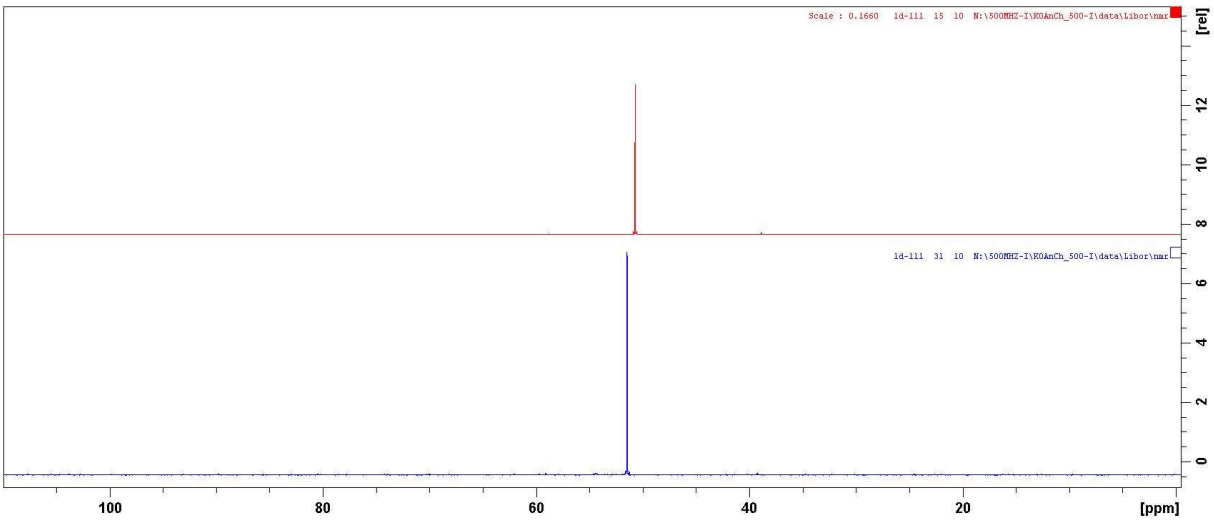

Figure S80: ^{31}P NMR spectra of Et_3PO (top) and its 1:5 molar mixture with **[NCN$^{t\mathrm{Bu}}$Te]Br** in dichloromethane-d_2.

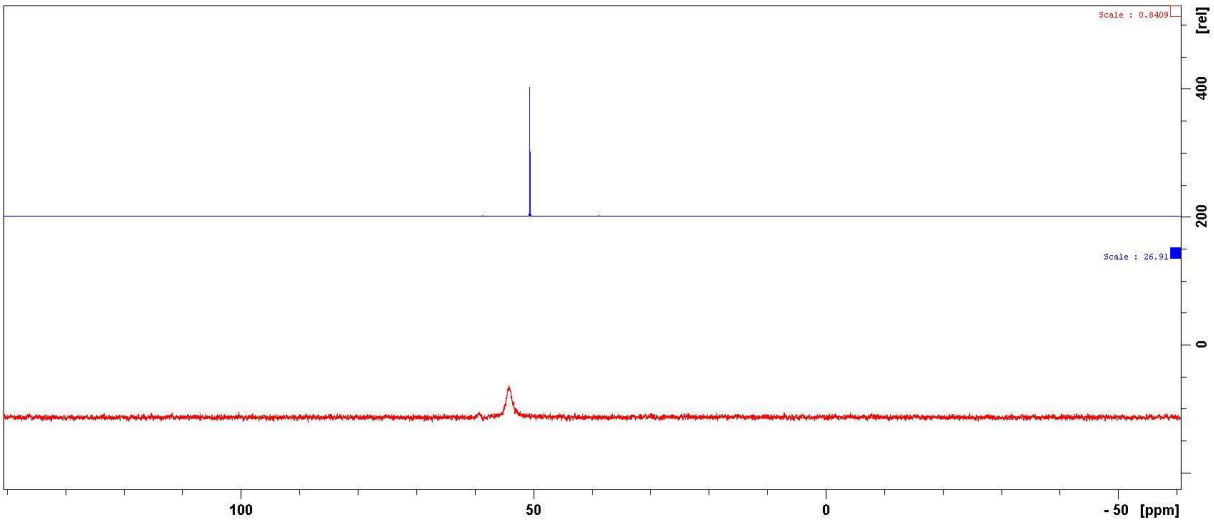

Figure S81: ^{31}P NMR spectra of Et_3PO (top) and its 1:5 molar mixture with **[NCN$^{t\mathrm{Bu}}$Te]OTf** in dichloromethane-d_2.

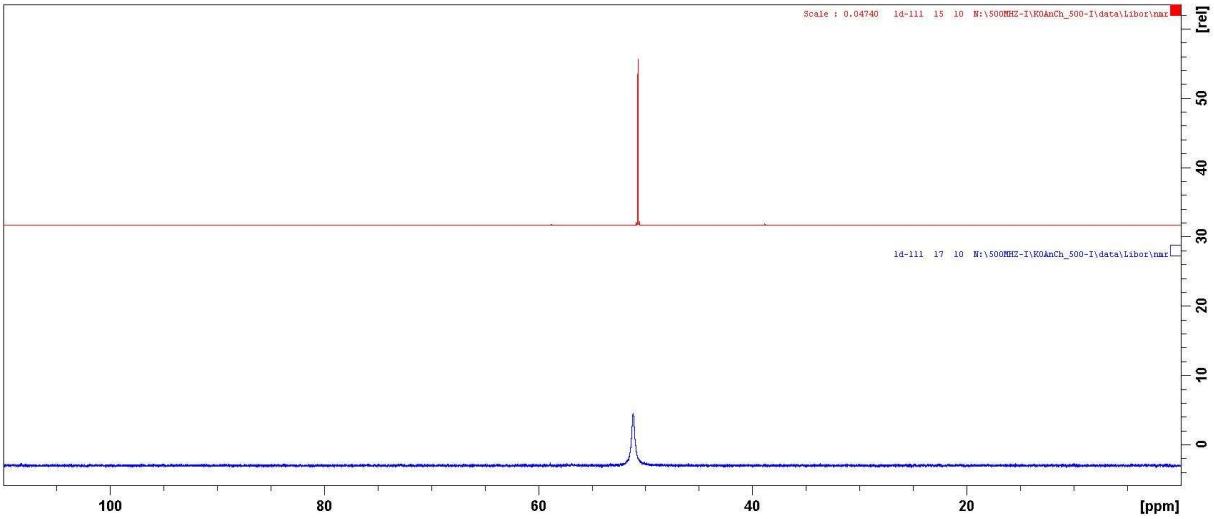

Figure S82: ^{31}P NMR spectra of Et_3PO (top) and its 1:5 molar mixture with **[NCN^{tBu}Te]SbF$_6$** in dichloromethane-d$_2$.

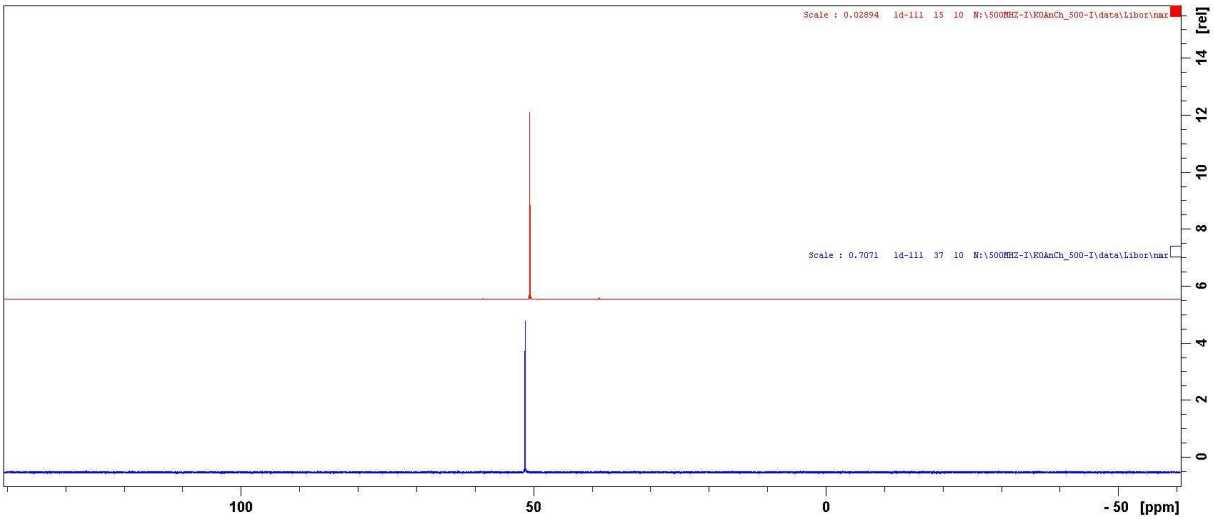

Figure S83: ^{31}P NMR spectra of Et_3PO (top) and its 1:5 molar mixture with **[NCN^{Dipp}Te]Br** in dichloromethane-d$_2$.

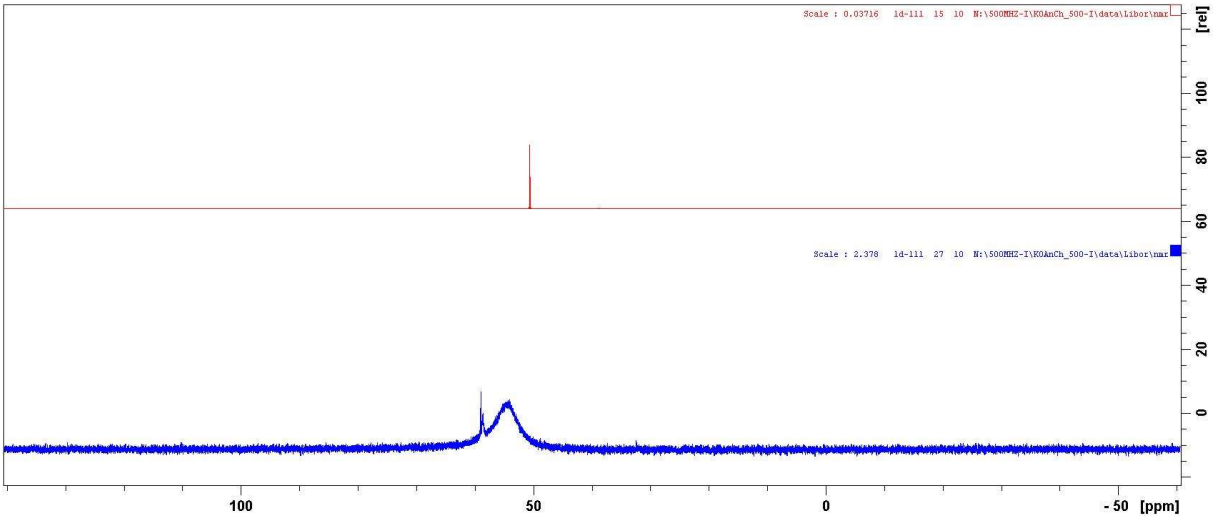

Figure S84: ^{31}P NMR spectra of Et_3PO (top) and its 1:5 molar mixture with **[NCN^{Dipp}Te]SbF$_6$** in dichloromethane-d$_2$.

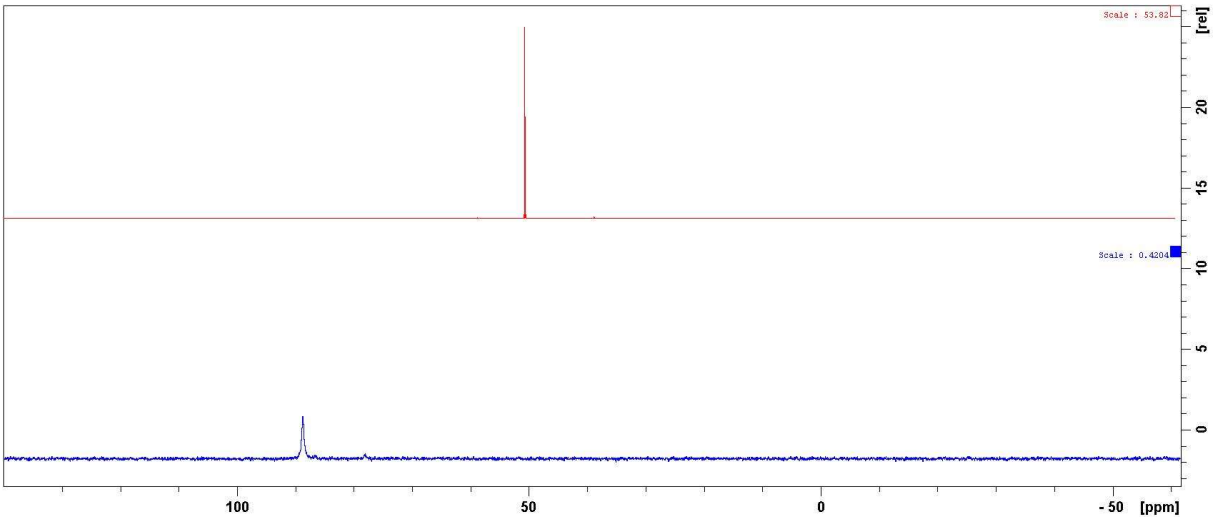

Figure S85: ^{31}P NMR spectra of Et_3PO (top) and its 1:5 molar mixture with **[CN^{tBu}TeCl$_2$]OTf** in dichloromethane-d$_2$.

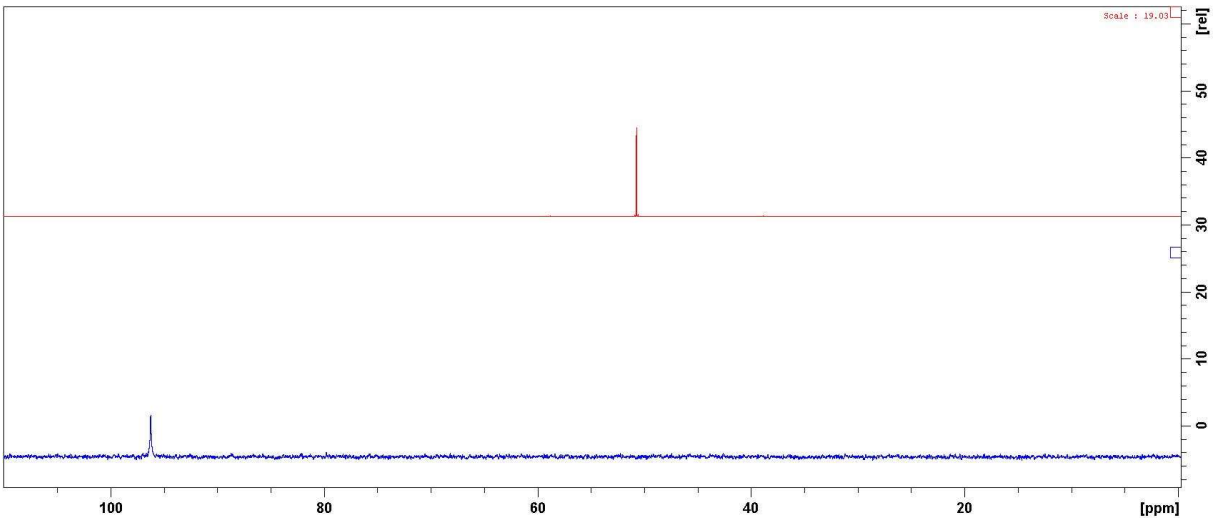

Figure S86: ^{31}P NMR spectra of Et_3PO (top) and its 1:5 molar mixture with **[CN^{tBu}TeCl$_2$]SbF$_6$** in dichloromethane-d$_2$.

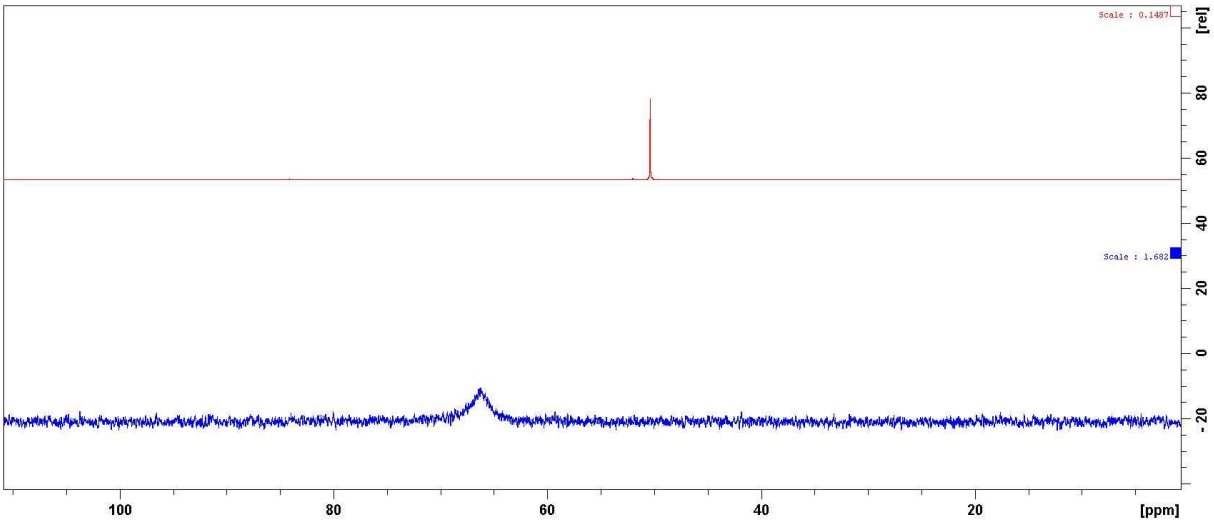

Figure S87: ^{31}P NMR spectra of Et_3PO (top) and its 1:5 molar mixture with **[NCN^{tBu}TeCl$_2$]OTf** in acetonitrile-d$_3$.

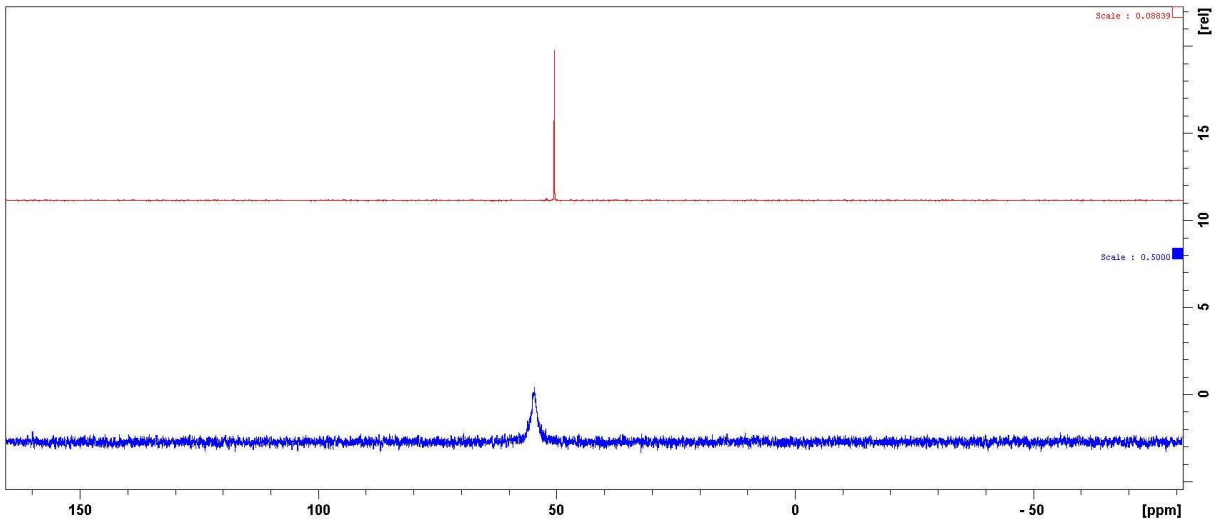

Figure S88: ^{31}P NMR spectra of Et_3PO (top) and its 1:5 molar mixture with **[NCN$^{t\mathrm{Bu}}$TeCl$_2$]SbF$_6$** in acetonitrile-d$_3$.

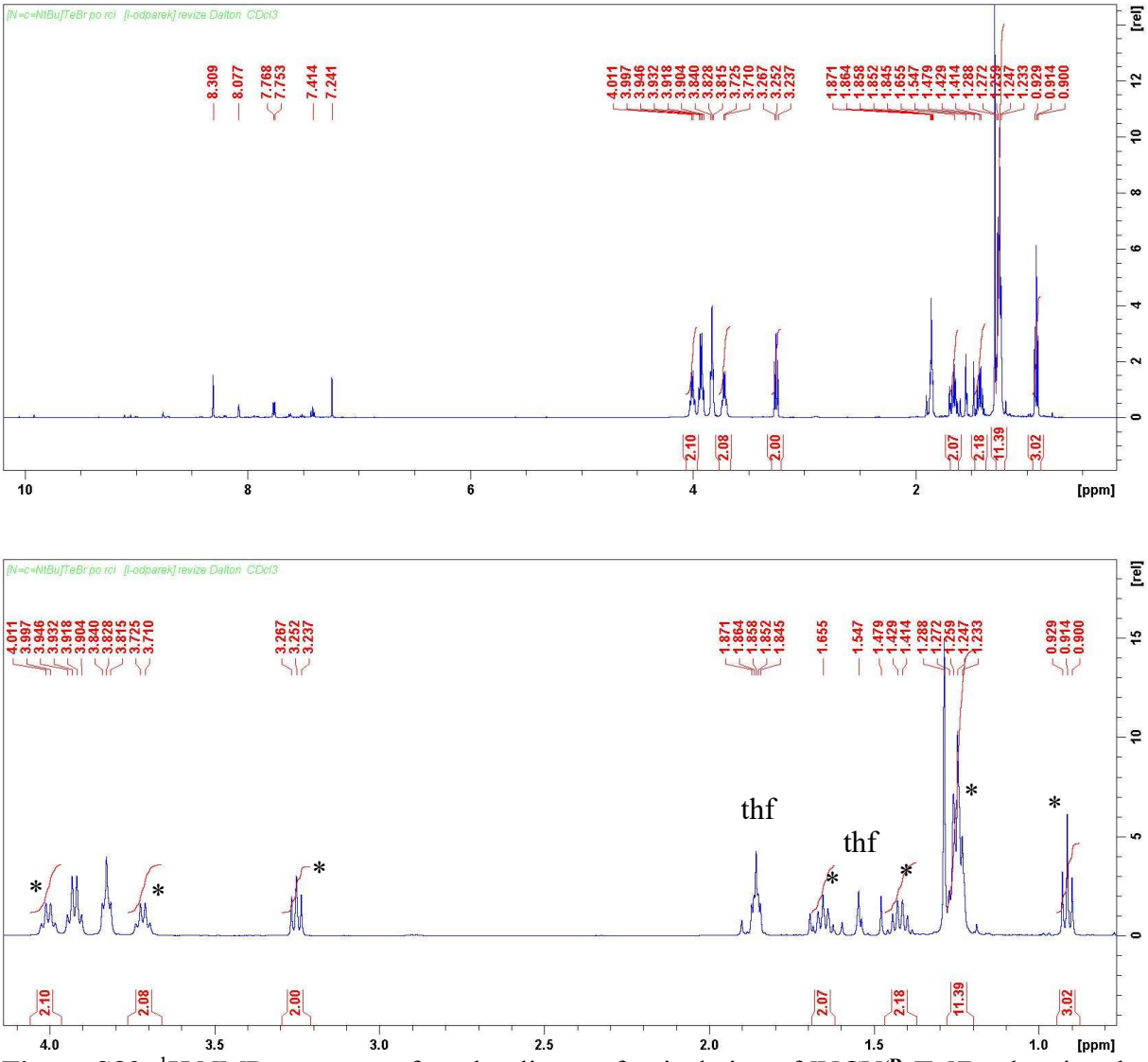

Figure S89: ^{1}H NMR spectrum of mother liquor after isolation of **[NCN$^{t\mathrm{Bu}}$Te]Br** showing the presence of *n*Bu(dtc) (*).

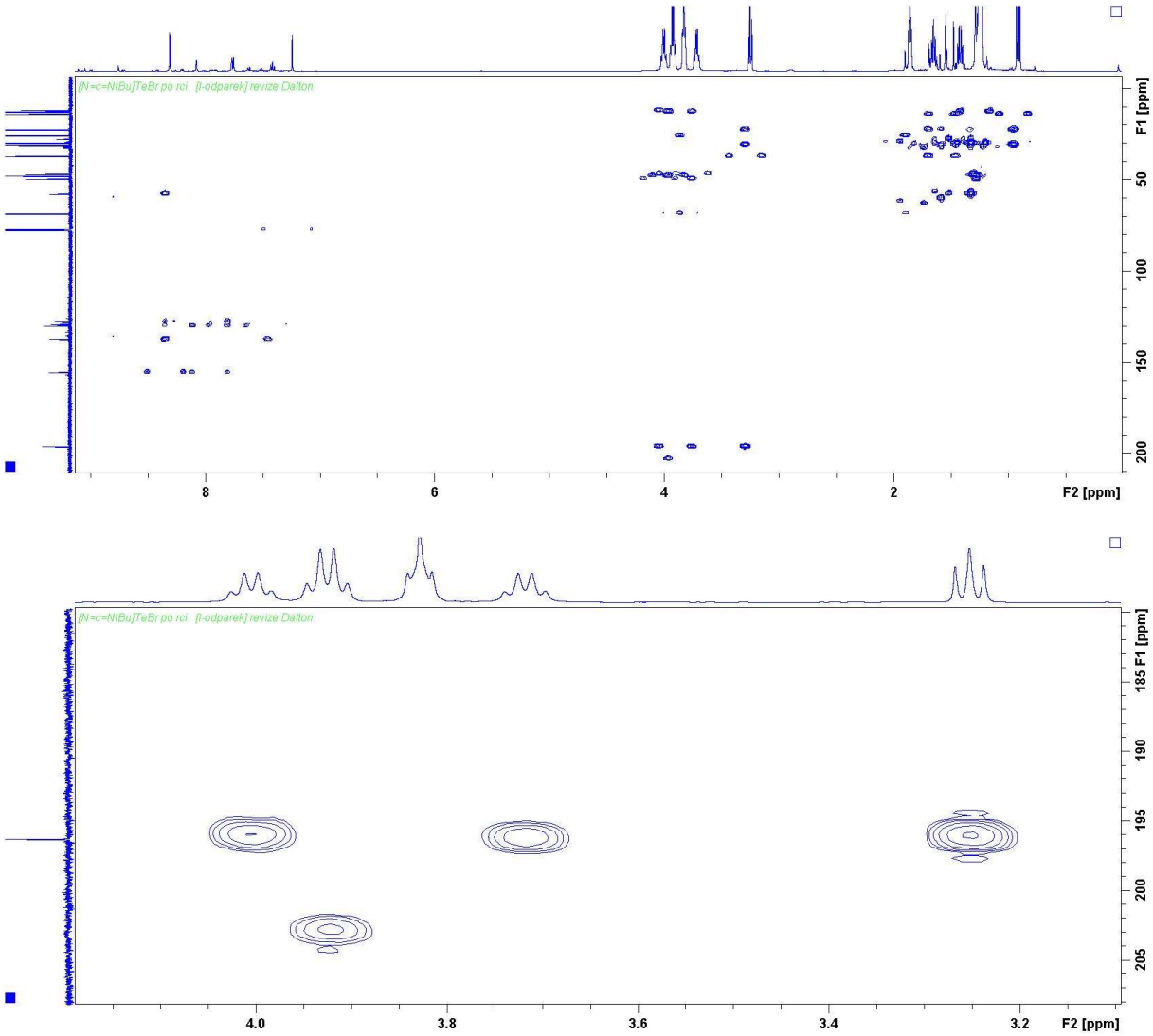

Figure S90: ^{1}H-^{13}C HMBC NMR spectrum of the mother liquor after isolation of **[NCN$^{t\mathrm{Bu}}$Te]Br** showing the presence coupling of all CH_2 groups form both dtc and *n*Bu with the *C*S_2 carbon.

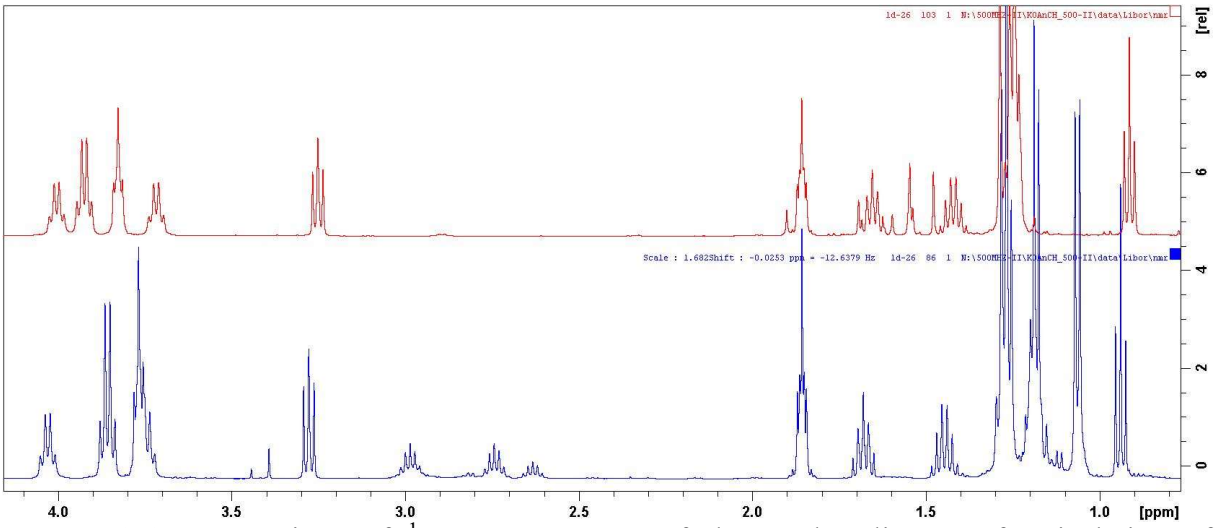

Figure S91: Comparison of ^{1}H NMR spectra of the mother liquors after isolation of **[NCN$^{t\mathrm{Bu}}$Te]Br** (red) and **[NCN^{Dipp}Te]Br** (blue) showing the presence *n*Bu(dtc) in both cases.

2) Solid state NMR spectra of studied compounds.

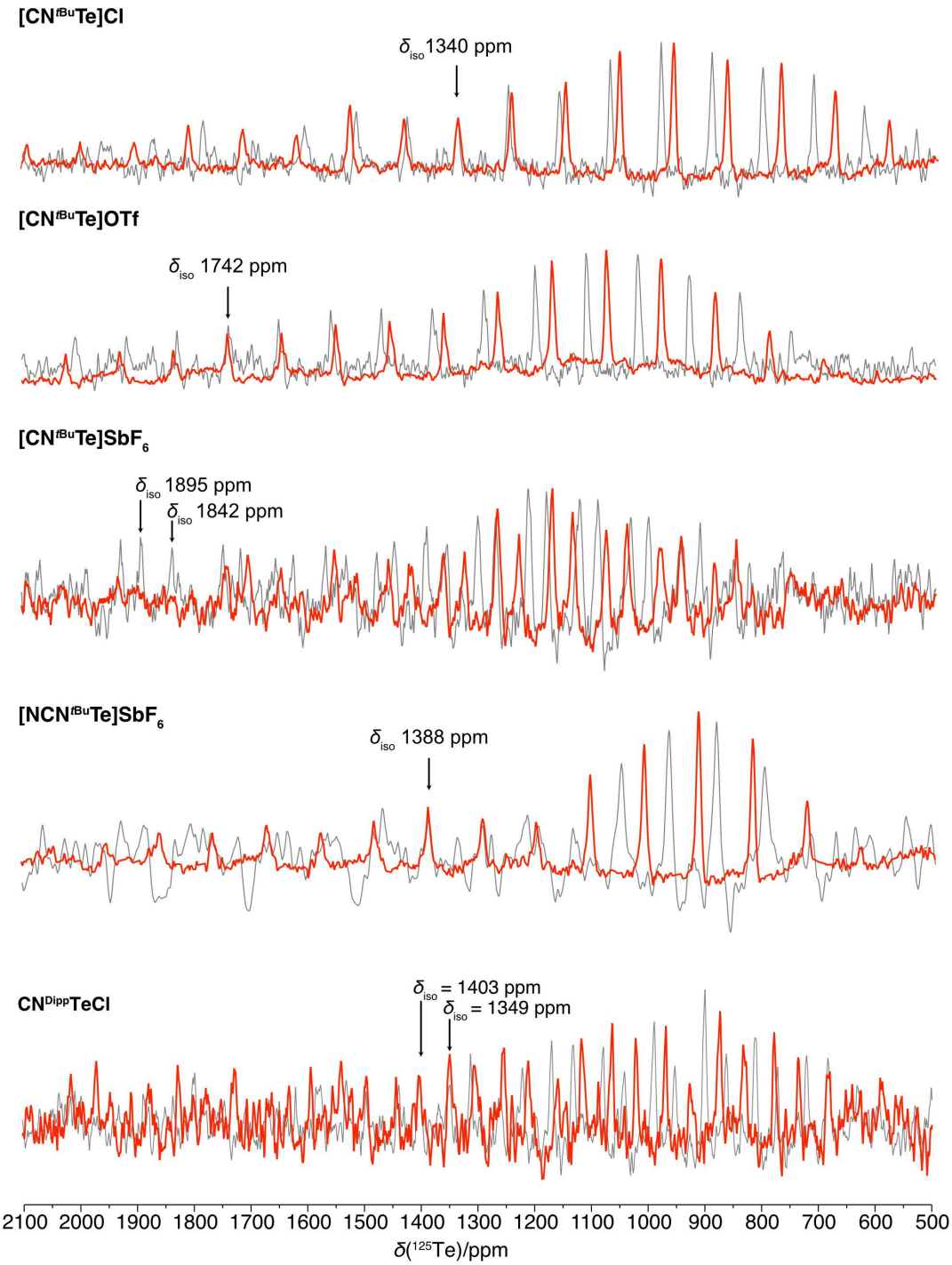

Figure S92: Solid-state MAS NMR ^{125}Te spectra (189.4 MHz, ambient temperature) of entitled complexes acquired at 18kHz MAS rate (red) compared with spectra at 17kHz MAS (16 kHz for [NCN^{tBu}Te]SbF$_6$) for identification of isotropic chemical shift (indicated in figure)

3) Crystallographic data for studied compounds.

Table S1. Crystal data and structure refinement of studied compounds.

	$CN^{Dipp}TeCl$	**$[NCN^{tBu}Te]Br$**	**$[CN^{Dipp}Te]SbF_6$**
Formula	$C_{19}H_{22}ClNTe$	$C_{16}H_{23}N_2TeBr$ CH_2Cl_2	$C_{19}H_{22}NTeF_6Sb$
Formula weight, g mol^{-1}	427.43	535.80	627.72
Crystal system	Monoclinic	Monoclinic	Monoclinic
Crystal size, mm	0.57 × 0.18 × 0.17	0.51 × 0.27 × 0.20	0.58 × 0.57 × 0.33
Space group	P-2$_1$/c	P-2$_1$/n	P-2$_1$/n
a, Å	9.4820(6)	11.2776(7)	15.2837(8)
b, Å	14.8539(12)	15.3893(11)	8.7618(4)
c, Å	26.6321(19)	12.0866(9)	16.0540(8)
α, º	90	90	90
β, º	94.310(6)	92.117(2)	94.823(2)
γ, º	90	90	90
V, Å^3	3740.4(5)	1151.69(16)	2142.22(18)
Z	8	4	4
ρ_{calcd}, Mg m^{-3}	1.518	1.698	1.946
μ (Mo $K\alpha$), mm^{-1}	1.730	3.581	2.678
F(000)	1696	1048	1200
θ range, deg	1 to 27.5	1 to 26.5	1 to 30.0
No. of reflns collected	29757	53971	54653
No. indep. Reflns	8488	4338	6799
No. obsd reflns with ($I>2\sigma(I)$), R_{int}	5881, 0.069	3678, 0.028	6487, 0.024
No. refined params	397	214	258
GooF (F^2)	1.183	1.075	1.174
R_1 (F) ($I > 2\sigma(I)$)	0.049	0.035	0.024
wR_2 (F^2) (all data)	0.072	0.095	0.052
Largest diff peak/hole, e Å^{-3}	0.689 / –0.790	0.786 / –1.691	0.857 / –0.974
CCDC	2254919	2254924	2254925

$R_{int} = \sum|F_o^2 - F_{o,mean}^2|/\sum F_o^2$, $S = [\sum(w(F_o^2 - F_c^2)^2)/(N_{diffrs} - N_{params})]^{½}$ for all data, $R(F) = \sum||F_o| - |F_c||/\sum|F_o|$ for observed data, $wR(F^2) = [\sum(w(F_o^2 - F_c^2)^2)/(\sum w(F_o^2)^2)]^{½}$ for all data.

Table S1 (continuation). Crystal data and structure refinement of studied compounds.

	[NCN^{tBu}Te]SbF$_6$	**[NCN^{Dipp}Te]SbF$_6$**	**CN^{tBu}TeCl$_2$OTf**
Formula	$C_{16}H_{23}N_2TeF_6Sb$	$C_{32}H_{39}N_2TeF_6Sb$ CH_2Cl_2	$C_{12}H_{14}Cl_2F_3NO_3STe$
Formula weight, g mol^{-1}	606.71	899.93	507.80
Crystal system	Monoclinic	Monoclinic	Triclinic
Crystal size, mm	0.59 × 0.28 × 0.15	0.59 × 0.42 × 0.38	0.59 × 0.38 × 0.22
Space group	P-2$_1$/c	P-2$_1$/c	P-1
a, Å	12.2981(13)	13.0781(6)	8.7695(6)
b, Å	9.0873(9)	16.2906(8)	10.5500(8)
c, Å	18.2137(17)	34.6077(17)	10.9648(8)
α, º	90	90	114.602(3)
β, º	97.656(4)	92.357(2)	96.732(3)
γ, º	90	90	106.032(3)
V, Å^3	2017.4(4)	7366.9(6)	854.61(11)
Z	4	8	2
ρ_{calcd}, Mg m^{-3}	1.998	1.623	1.973
μ (Mo $K\alpha$), mm^{-1}	2.841	1.725	2.215
F(000)	1160	3552	492
θ range, deg	1 to 27.5	1 to 30	1 to 27.5
No. of reflns collected	58182	220696	25095
No. indep. Reflns	4653	22937	3954
No. obsd reflns with ($I>2\sigma(I)$), R_{int}	4355, 0.026	18589, 0.035	3629, 0.026
No. refined params	241	837	211
GooF (F^2)	1.338	1.081	1.071
R_1 (F) ($I > 2\sigma(I)$)	0.030	0.037	0.022
wR_2 (F^2) (all data)	0.069	0.071	0.052
Largest diff peak/hole, e Å^{-3}	0.668 / –1.052	0.806 / –1.401	0.582 / –1.305
CCDC	2254923	2254927	2254918

$R_{int} = \sum|F_o^2 - F_{o,mean}^2|/\sum F_o^2$, S = $[\sum(w(F_o^2 - F_c^2)^2)/(N_{diffrs} - N_{params})]^{½}$ for all data, $R(F) = \sum||F_o| - |F_c||/\sum|F_o|$ for observed data, $wR(F^2) = [\sum(w(F_o^2 - F_c^2)^2)/(\sum w(F_o^2)^2)]^{½}$ for all data.

Table S1 (continuation). Crystal data and structure refinement of studied compounds.

	[NCN^{tBu}TeCl$_2$]OTf	**[NCN^{tBu}TeCl$_2$]SbF$_6$**	**[COTeCl$_2$]$_2$O**
Formula	$C_{16}H_{23}Cl_2N_2TeCF_3O_3S$	$C_{16}H_{23}Cl_2N_2TeF_6Sb$	$C_{14}H_{10}Cl_4O_3Te_2$
Formula weight, g mol^{-1}	590.93	677.61	623.22
Crystal system	Monoclinic	Monoclinic	Triclinic
Crystal size, mm	0.43 × 0.32 × 0.08	0.51 × 0.30 × 0.17	0.16 × 0.15 × 0.14
Space group	P-2$_1$/c	P-2$_1$/n	P-1
a, Å	12.2012(8)	12.6772(8)	7.9068(4)
b, Å	8.8429(6)	8.8511(5)	8.7710(5)
c, Å	20.7838(12)	20.6032(13)	14.0259(6)
α, º	90	90	105.762(2)
β, º	100.101(2)	106.793(2)	98.604(2)
γ, º	90	90	97.406(2)
V, Å^3	2207.7(2)	2213.2(2)	910.99(8)
Z	4	4	2
ρ_{calcd}, Mg m^{-3}	1.778	2.034	2.272
μ (Mo $K\alpha$), mm^{-1}	1.730	2.834	3.797
F(000)	1168	1296	580
θ range, deg	1 to 27.5	1 to 27	1 to 27.5
No. of reflns collected	42725	30575	24977
No. indep. Reflns	5091	4549	4208
No. obsd reflns with ($I>2\sigma(I)$), R_{int}	4626, 0.026	4401, 0.024	3725, 0.022
No. refined params	279	259	202
GooF (F^2)	1.212	1.306	1.098
R_1 (F) ($I > 2\sigma(I)$)	0.041	0.040	0.026
wR_2 (F^2) (all data)	0.088	0.100	0.056
Largest diff peak/hole, e Å^{-3}	1.051 / –2.351	1.132 / –2.044	1.791 / –1.972
CCDC	2254922	2254921	2254920

$R_{int} = \sum|F_o^2 - F_{o,mean}^2|/\sum F_o^2$, S = $[\sum(w(F_o^2 - F_c^2)^2)/(N_{diffrs} - N_{params})]^{½}$ for all data, $R(F) = \sum||F_o| - |F_c||/\sum|F_o|$ for observed data, $wR(F^2) = [\sum(w(F_o^2 - F_c^2)^2)/(\sum w(F_o^2)^2)]^{½}$ for all data.

Table S1 (continuation). Crystal data and structure refinement of studied compounds.

	[OCN^{tBu}TeCl$_2$]$_2$O
Formula	$C_{24}H_{28}Cl_4N_2O_3Te_2$
Formula weight, g mol^{-1}	789.48
Crystal system	monoclinic
Crystal size, mm	0.59 × 0.38 × 0.22
Space group	P-2$_1$/n
a, Å	9.628(4)
b, Å	22.625(10)
c, Å	13.848(6)
α, º	90
β, º	107.181(15)
γ, º	90
V, Å^3	2882(2)
Z	4
ρ_{calcd}, Mg m^{-3}	1.820
μ (Mo *Kα*), mm^{-1}	2.424
F(000)	1528
θ range, deg	1 to 26.5
No. of reflns collected	70961
No. indep. Reflns	5946
No. obsd reflns with ($I>2\sigma(I)$), R_{int}	5550, 0.019
No. refined params	316
GooF (F^2)	1.088
R_1 (F) ($I > 2\sigma(I)$)	0.033
wR_2 (F^2) (all data)	0.076
Largest diff peak/hole, e Å^{-3}	2.167 / –2.164
CCDC	2254926

$R_{int} = \sum|F_o^2 - F_{o,mean}^2|/\sum F_o^2$, S = $[\sum(w(F_o^2 - F_c^2)^2)/(N_{diffrs} - N_{params})]^{½}$ for all data, $R(F) = \sum||F_o| - |F_c||/\sum|F_o|$ for observed data, $wR(F^2) = [\sum(w(F_o^2 - F_c^2)^2)/(\sum w(F_o^2)^2)]^{½}$ for all data.

4) Theoretical study

Table S2. Topological and integrated bond properties from AIM and ELI-D of compounds **[CN^{tBu}TeCl$_2$]SbF$_6$**, **[CN^{Dipp}Te]SbF$_6$** as well as on the cations **[NCN^{tBu}Te]$^+$**, **[NCN^{tBu}TeCl$_2$]$^+$** and **[NCN^{Dipp}Te]$^+$**. For comparison the already reported data of **[CN^{tBu}Te]$^+$** are also listed (ref. 23 of the main manuscript).

model	contact or basin	d [Å]	ρ(r) [eÅ^{-3}]	∇^{2}ρ(r) [eÅ^{-5}]	ε	G/ρ(r) [a.u.]	H/ρ(r) [a.u.]	δ(Te,X)	N_{ELI} [e]	γ_{ELI}
[CN^{tBu}TeCl$_2$]SbF$_6$	Te–N	2.197	0.64	2.8	0.02	0.70	–0.40	0.60	2.45	1.71
(lin. Cl–Te–Cl)	Te–F3	2.244	0.42	4.4	0.09	0.89	–0.15	0.37		
	Te–Cl22	2.484	0.52	1.5	0.05	0.56	–0.36	0.73		
	Te–Cl23	2.456	0.55	1.5	0.04	0.57	–0.38	0.77		
[CN^{tBu}TeCl$_2$]SbF$_6$	Te–N	2.325	0.51	2.2	0.04	0.61	–0.31	0.48	2.54	1.75
(rec. Cl–Te–Cl)	Te–F30	2.412	0.30	3.2	0.13	0.82	–0.08	0.26		
	Te–Cl2	2.419	0.59	1.6	0.03	0.58	–0.40	0.84		
	Te–Cl5	2.360	0.65	1.4	0.06	0.59	–0.44	0.90		
[CN^{Dipp}Te]SbF$_6$	Te–N	2.100	0.73	5.0	0.26	0.90	–0.43	0.82	2.58	1.65
	Te–F3	2.350	0.33	3.5	0.09	0.86	–0.11	0.34		
	Te–F6	3.315	0.06	0.7	0.90	0.74	0.10	0.05		
[CN^{tBu}Te]SbF$_6$*	Te–N	2.076	0.77	4.7		0.91	–0.45		2.48	1.64
	Te–F	2.689	0.16	1.6		0.76	–0.02			
[NCN^{tBu}Te]$^+$	Te–N2	2.294	0.51	3.0	0.19	0.71	–0.30	0.60	2.49	1.74
	Te–N4	2.266	0.53	3.2	0.22	0.73	–0.31	0.63	2.58	1.72
[NCN^{tBu}TeCl$_2$]$^+$	Te–N3	2.308	0.52	2.2	0.05	0.61	–0.32	0.51	2.45	1.74
	Te–N6	2.308	0.52	2.2	0.05	0.61	–0.32	0.50	2.45	1.74
	Te–Cl1	2.468	0.54	1.5	0.05	0.56	–0.37	0.74		
	Te–Cl5	2.468	0.54	1.5	0.05	0.56	–0.37	0.74		
[NCN^{Dipp}Te]$^+$	Te–N2	2.248	0.55	3.3	0.20	0.75	–0.33	0.62	2.48	1.72
	Te–N4	2.243	0.56	3.3	0.21	0.75	–0.33	0.63	2.49	1.71

* see reference 23 of main manuscript.

Table S3. Atomic charges [in e], derived from the AIM analysis and Natural Population Analysis of compounds **[CN^{tBu}TeCl$_2$]SbF$_6$**, **[CN^{Dipp}Te]SbF$_6$** as well as on the cations **[NCN^{tBu}Te]$^+$**, **[NCN^{tBu}TeCl$_2$]$^+$** and **[NCN^{Dipp}Te]$^+$**.

	Te		**N1 (top) N2 (botton)**		**F**		**Cl1 (top) Cl2 (bottom)**	
	q_{AIM}	q_{NPA}	q_{AIM}	q_{NPA}	q_{AIM}	q_{NPA}	q_{AIM}	q_{NPA}
[CN^{tBu}TeCl$_2$]SbF$_6$ (lin. Cl–Te–Cl)	1.83	1.81	–1.23	–0.56	–0.73	–0.68	–0.56	–0.51
							–0.52	–0.48
[CN^{tBu}TeCl$_2$]SbF$_6$ (rec. Cl–Te–Cl)	1.77	1.72	–1.22	–0.56	–0.74	–0.69	–0.52	–0.45
							–0.46	–0.38
[CN^{Dipp}Te]SbF$_6$	1.09	1.10	–1.28	–0.59	–0.73	–0.67		
[NCN^{tBu}Te]$^+$	0.99	1.00	–1.20	–0.53				
			–1.19	–0.54				
[NCN^{tBu}TeCl$_2$]$^+$	1.75	1.72	–1.21	–0.52			–0.54	–0.48
			–1.21	–0.52			–0.54	–0.48
[NCN^{Dipp}Te]$^+$	1.04	1.05	–1.26	–0.54				
			–1.26	–0.54				

Table S4. Second order perturbation theory analysis derived from NBO analysis of selected interactions of compounds **[CN^{tBu}TeCl$_2$]SbF$_6$**, **[CN^{Dipp}Te]SbF$_6$** as well as on the cations **[NCN^{tBu}Te]$^+$**, **[NCN^{tBu}TeCl$_2$]$^+$** and **[NCN^{Dipp}Te]$^+$** with respective occupancies given in brackets.

	Donor NBO	Acceptor NBO	Energy [kcal mol^{-1}]
[CN^{tBu}TeCl$_2$]SbF$_6$	LP(3)F3 (1.90794)	RY(1)Te (0.31667)	10.29
(lin. Cl–Te–Cl)	LP(1)N (1.63661)	RY(1)Te (0.31667)	37.44
	BD(1)Te-Cl22 (1.85806)	BD*(1)Te-Cl23 (0.24795)	59.59
	BD(1)Te-Cl22 (1.85806)	RY(1)Te (0.31667)	29.91
	BD(1)Te-Cl23 (1.85239)	BD*(1)Te-Cl22 (0.26057)	63.52
	BD(1)Te-Cl23 (1.85239)	RY(1)Te (0.31667)	31.73
[CN^{tBu}TeCl$_2$]SbF$_6$	LP(3)F30 (1.93947)	BD*(1)Te-Cl5 (0.14510)	13.55
(rec. Cl–Te–Cl)	LP(1)N3 (1.70144)	BD*(1)Te-Cl2 (0.27237)	53.91
[CN^{Dipp}Te]SbF$_6$	LP(3)F3 (1.90475)	BD*(1)Te-N (0.11949)	20.81
[NCN^{tBu}Te]$^+$	LP(1)N2 (1.68533)	LV(1)Te (0.55477)	103.73
	LP(1) N4 (1.67844)	LV(1)Te (0.55477)	111.10
[NCN^{tBu}TeCl$_2$]$^+$	LP(1)N3 (1.67240)	RY(1)Te (0.64751)	119.72
	LP(1)N6 (1.67241)	RY(1)Te (0.64751)	119.73
	BD(1)Te-Cl2 (1.82537)	BD*(1)Te-Cl5 (0.13684)	106.08
	BD(1)Te-Cl5 (1.82537)	BD*(1)Te-Cl2 (0.17640)	106.09
[NCN^{Dipp}Te]$^+$	LP(1)N2 (1.66946)	LV(1)Te (0.53525)	108.79
	LP(1)N4 (1.66756)	LV(1)Te (0.53525)	110.89

Table S5. Additionally, a 3-center, 4-electron hyperbond was detected in the NBO analysis for **[CN^{tBu}TeCl$_2$]SbF$_6$** with the rectangular Cl–Te–Cl linkage.

	Hyperbond A:-B-:C	%A-B/%B-C	Occupation
[CN^{tBu}TeCl$_2$]SbF$_6$	Cl2:-Te-:N3	65.0/35.0	3.9566
(rec. Cl–Te–Cl)			

Table S6. Wiberg Bond Indices (WBI), NLMO/NPA Bond Orders and delocalization index (δ) of compounds **[CN^{tBu}TeCl$_2$]SbF$_6$**, **[CN^{Dipp}Te]SbF$_6$** as well as on the cations **[NCN^{tBu}Te]$^+$**, **[NCN^{tBu}TeCl$_2$]$^+$** and **[NCN^{Dipp}Te]$^+$**.

	contact	WBI	NLMO/NPA	δ(Te,X)
[CN^{tBu}TeCl$_2$]SbF$_6$	Te–N	0.47	0.31	0.60
(lin. Cl–Te–Cl)	Te–F3	0.19	0.10	0.37
	Te–Cl22	0.58	0.41	0.73
	Te–Cl23	0.62	0.44	0.77
[CN^{tBu}TeCl$_2$]SbF$_6$	Te–N	0.33	0.17	0.48
(rec. Cl–Te–Cl)	Te–F30	0.11	0.05	0.26
	Te–Cl2	0.69	0.50	0.84
	Te–Cl5	0.79	0.73	0.90
[CN^{Dipp}Te]SbF$_6$	Te–N	0.63	0.38	0.82
	Te–F3	0.15	0.08	0.34
	Te–F6	0.01	0.01	0.05
[NCN^{tBu}Te]$^+$	Te–N2	0.43	0.23	0.60
	Te–N4	0.46	0.28	0.63
[NCN^{tBu}TeCl$_2$]$^+$	Te–N3	0.38	0.25	0.51
	Te–N6	0.38	0.25	0.50
	Te–Cl1	0.59	0.43	0.74
	Te–Cl5	0.59	0.43	0.74
[NCN^{Dipp}Te]$^+$	Te–N2	0.25	0.45	0.62
	Te–N4	0.28	0.45	0.63

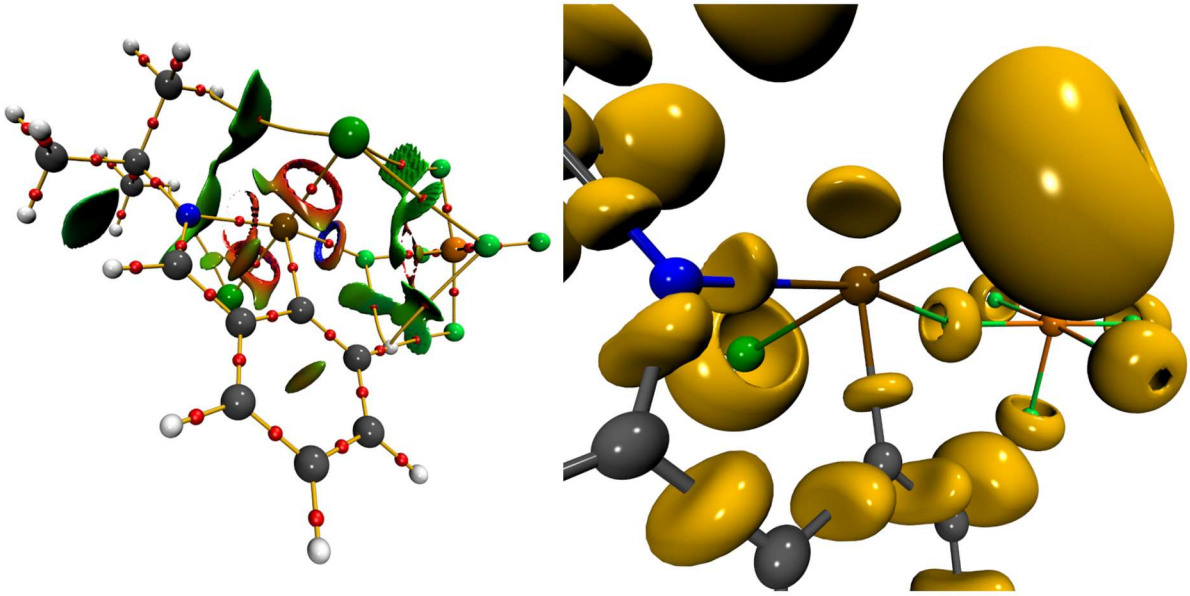

Figure S93. *left:* AIM molecular graph of **[CN$^{t\mathrm{Bu}}$TeCl$_2$]SbF$_6$** (linear Cl–Te–Cl linkage) with bond critical points as red spheres and bond paths in orange as well as NCI iso-surfaces of at s(r) = 0.5 color coded with sign(λ_2)ρ in a. u. Blue surfaces refer to attractive forces and red to repulsive forces. Green indicates weak interactions. *Right:* ELI-D localization domain representation at *iso*-value of 1.5.

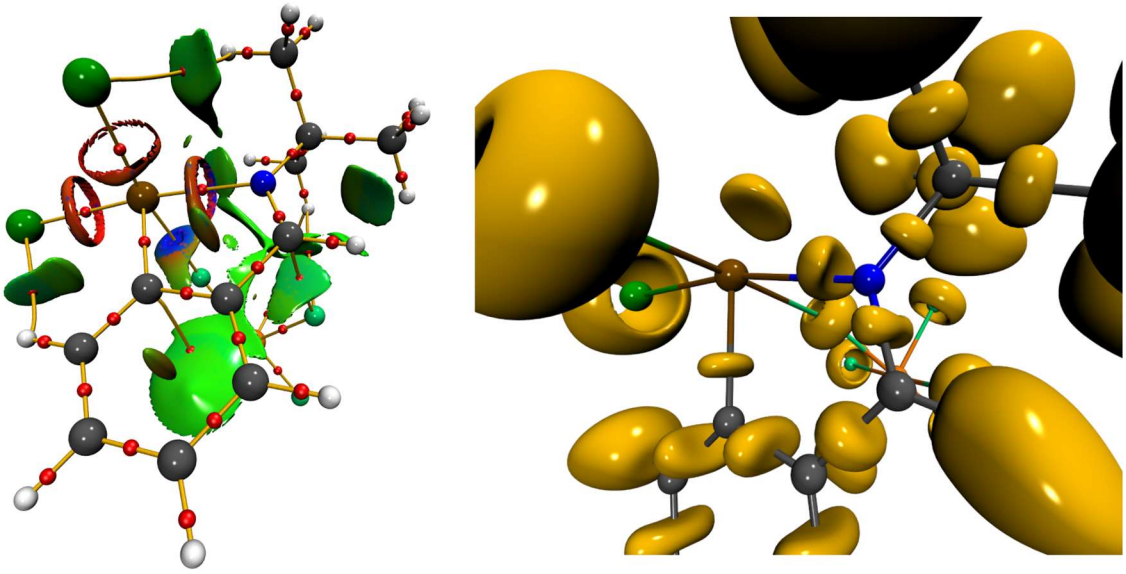

Figure S94. *left:* AIM molecular graph of **[CN$^{t\mathrm{Bu}}$TeCl$_2$]SbF$_6$** (rectangular Cl–Te–Cl linkage) with bond critical points as red spheres and bond paths in orange as well as NCI iso-surfaces at s(r) = 0.5 color coded with sign(λ_2)ρ in a. u. Blue surfaces refer to attractive forces and red to

repulsive forces. Green indicates weak interactions. *Right:* ELI-D localization domain representation at an *iso*-value of 1.5.

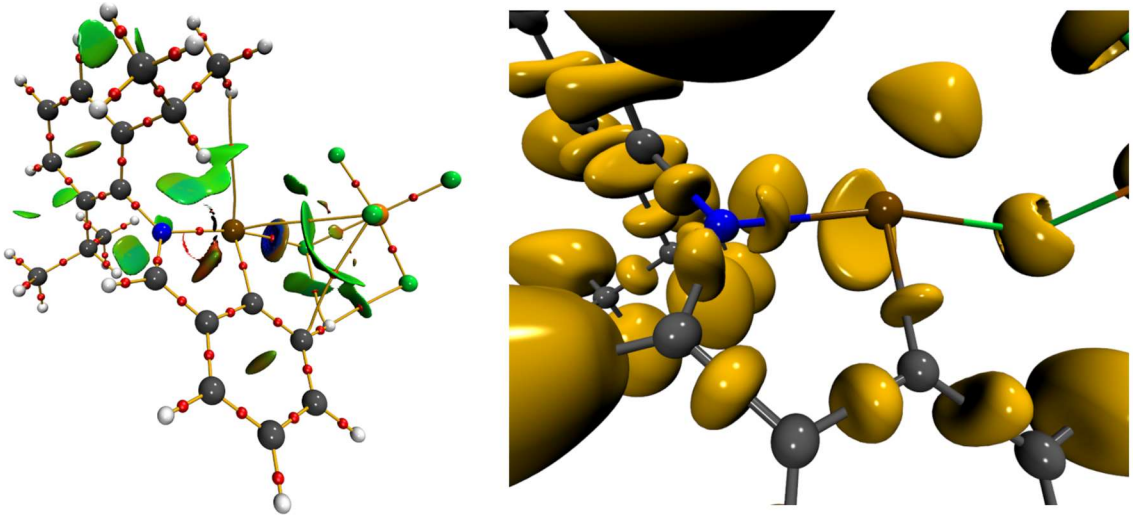

Figure S95. *left:* AIM molecular graph of **[CN^{Dipp}Te]SbF$_6$** with bond critical points as red spheres and bond paths in orange as well as NCI iso-surfaces at s(r) = 0.5 color coded with sign(λ_2)ρ in a. u. Blue surfaces refer to attractive forces and red to repulsive forces. Green indicates weak interactions. *Right:* ELI-D localization domain representation at an *iso*-value of 1.5.

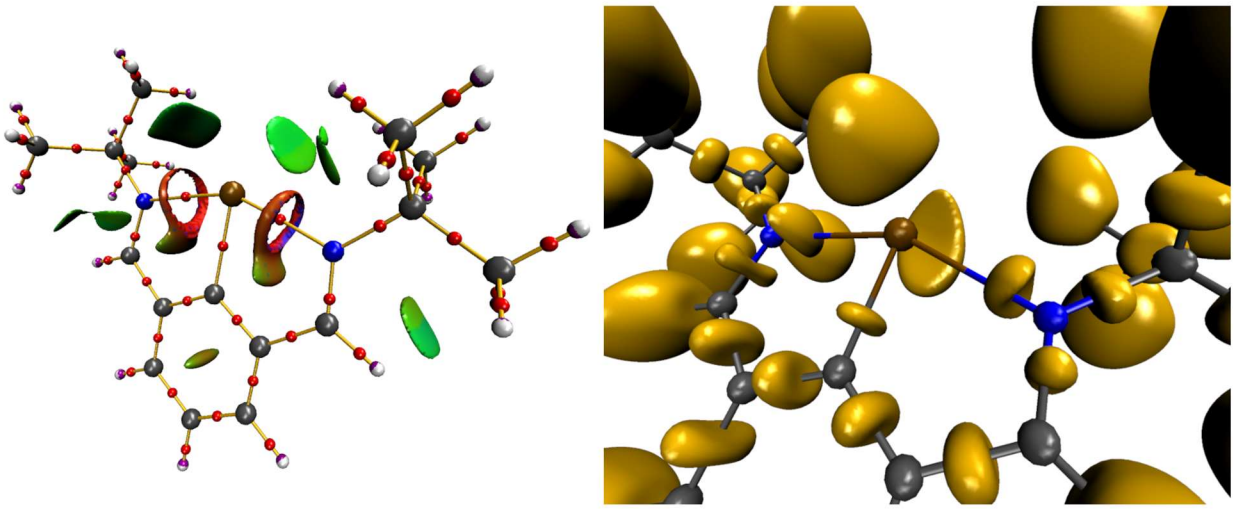

Figure S96. *left:* AIM molecular graph of **[NCN^{tBu}Te]$^+$** with bond critical points as red spheres and bond paths in orange as well as NCI iso-surfaces at s(r) = 0.5 color coded with sign(λ_2)ρ in a. u. Blue surfaces refer to attractive forces and red to repulsive forces. Green indicates weak interactions. *Right:* ELI-D localization domain representation at an *iso*-value of 1.5.

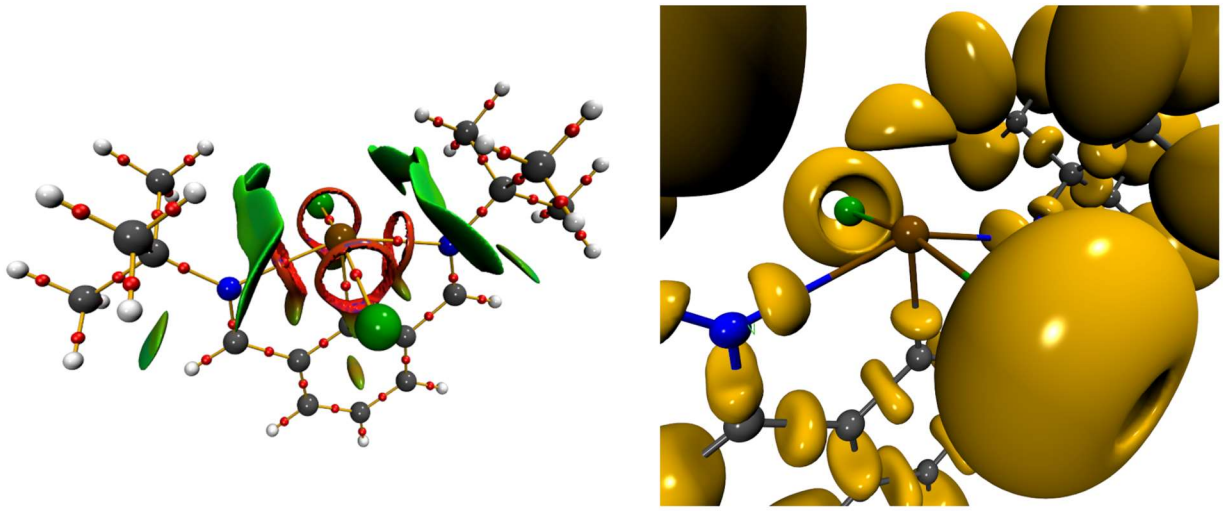

Figure S97. *left:* AIM molecular graph of **[NCN$^{t\mathrm{Bu}}$TeCl$_2$]$^+$** with bond critical points as red spheres and bond paths in orange as well as NCI iso-surfaces at s(r) = 0.5 color coded with sign(λ_2)ρ in a. u. Blue surfaces refer to attractive forces and red to repulsive forces. Green indicates weak interactions. *Right:* ELI-D localization domain representation at an *iso*-value of 1.5.

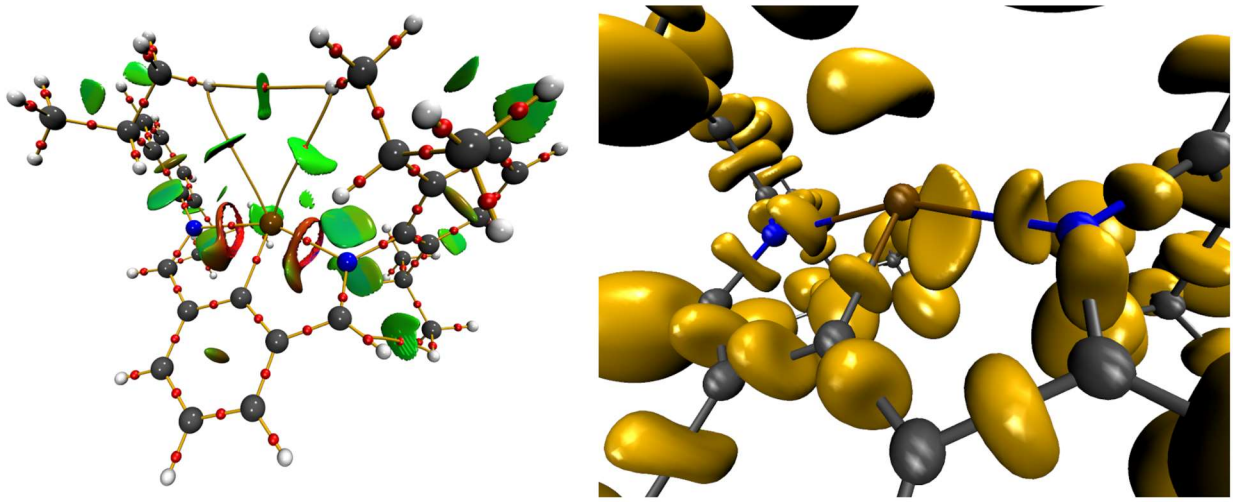

Figure S98. *left:* AIM molecular graph of **[NCN^{Dipp}Te]$^+$** with bond critical points as red spheres and bond paths in orange as well as NCI iso-surfaces at s(r) = 0.5 color coded with sign(λ_2)ρ in a. u. Blue surfaces refer to attractive forces and red to repulsive forces. Green indicates weak interactions. *Right:* ELI-D localization domain representation at an *iso*-value of 1.5.

5) HR-MALDI-MS

Theoretical HR-MALDI-MS spectra were calculated using Qual Browser, Thermo Xcalibur 4.0.27.10 software (Thermo Scientific).

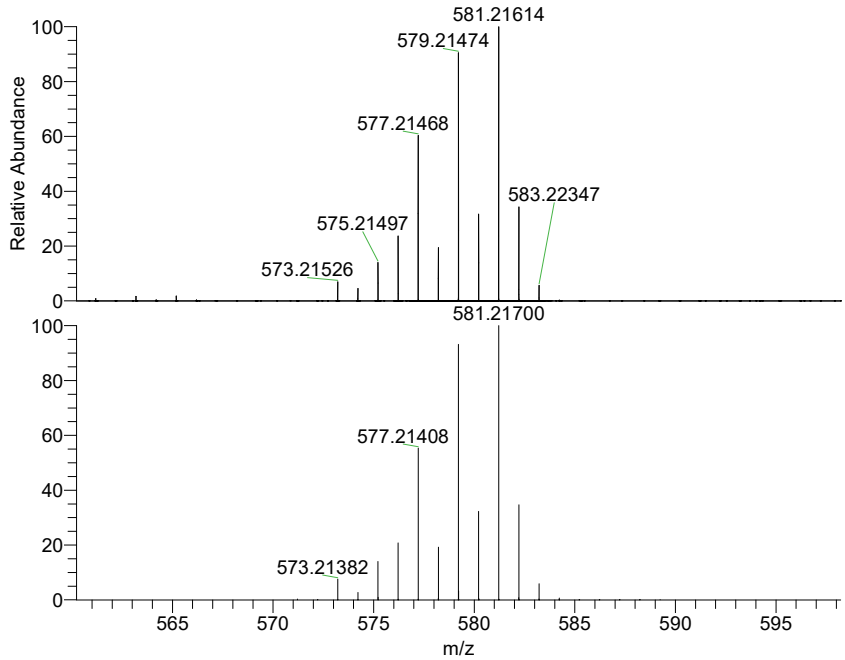

Figure S99. Experimental (top) and calculated (bottom) HR-MALDI-MS of **[NCN^{Dipp}Te]Br**.

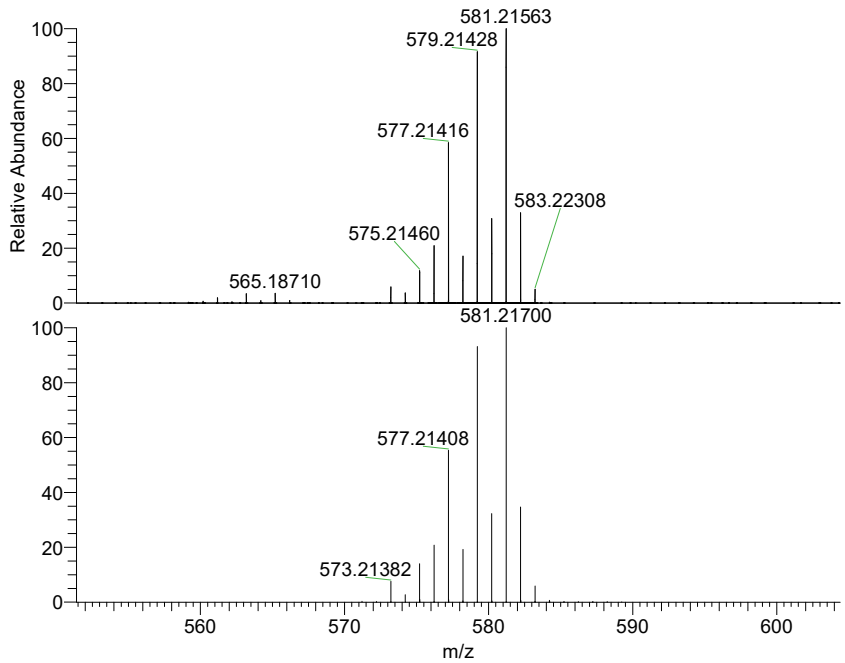

Figure S100. Experimental (top) and calculated (bottom) HR-MALDI-MS of **[NCN^{Dipp}Te]SbF$_6$**.

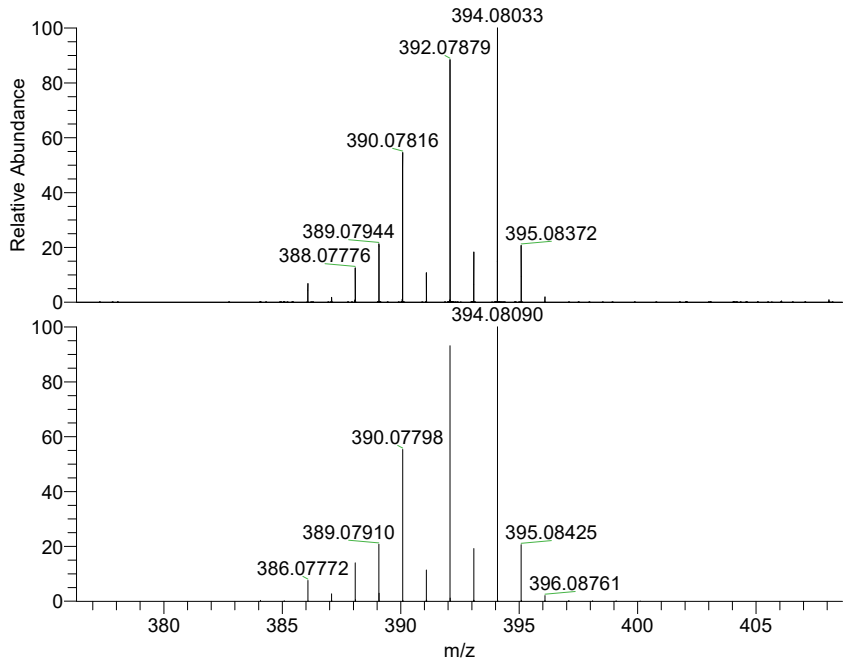

Figure S101. Experimental (top) and calculated (bottom) HR-MALDI-MS of **[CN^{Dipp}Te]SbF$_6$**.

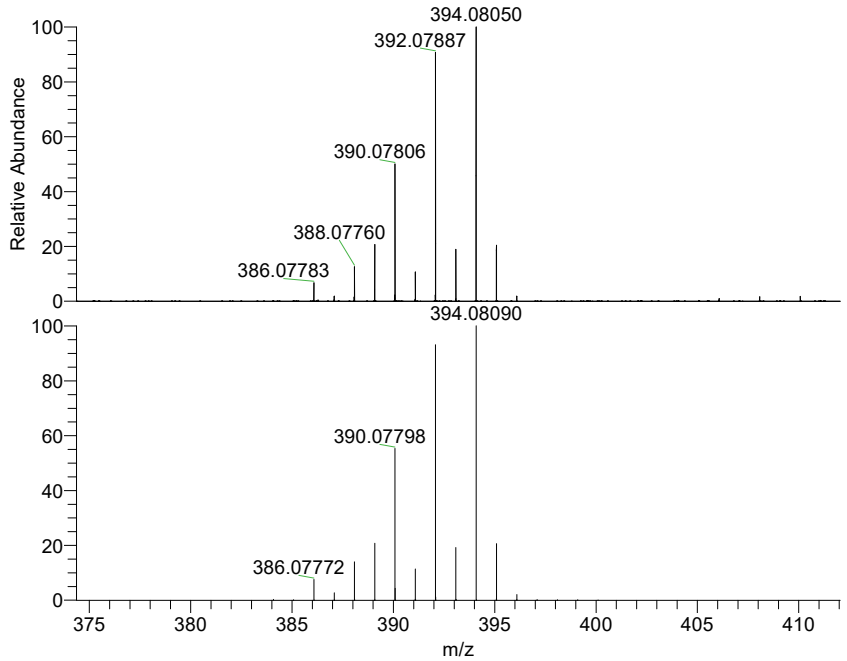

Figure S102. Experimental (top) and calculated (bottom) HR-MALDI-MS of **CN^{Dipp}TeCl**.

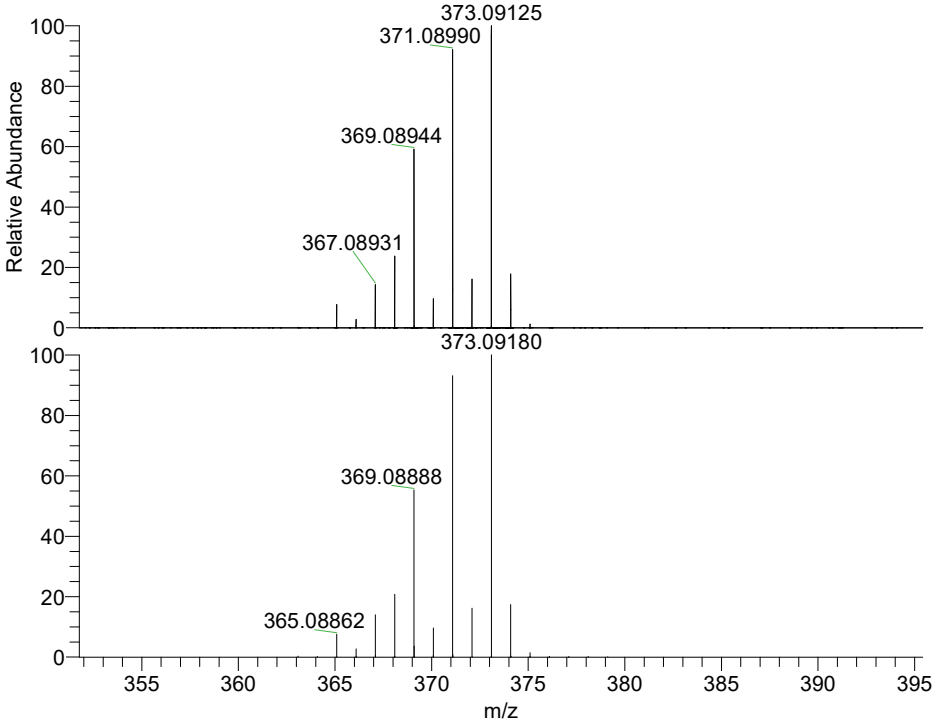

Figure S103. Experimental (top) and calculated (bottom) HR-MALDI-MS of **[NCN$^{t\mathrm{Bu}}$Te]Br**.

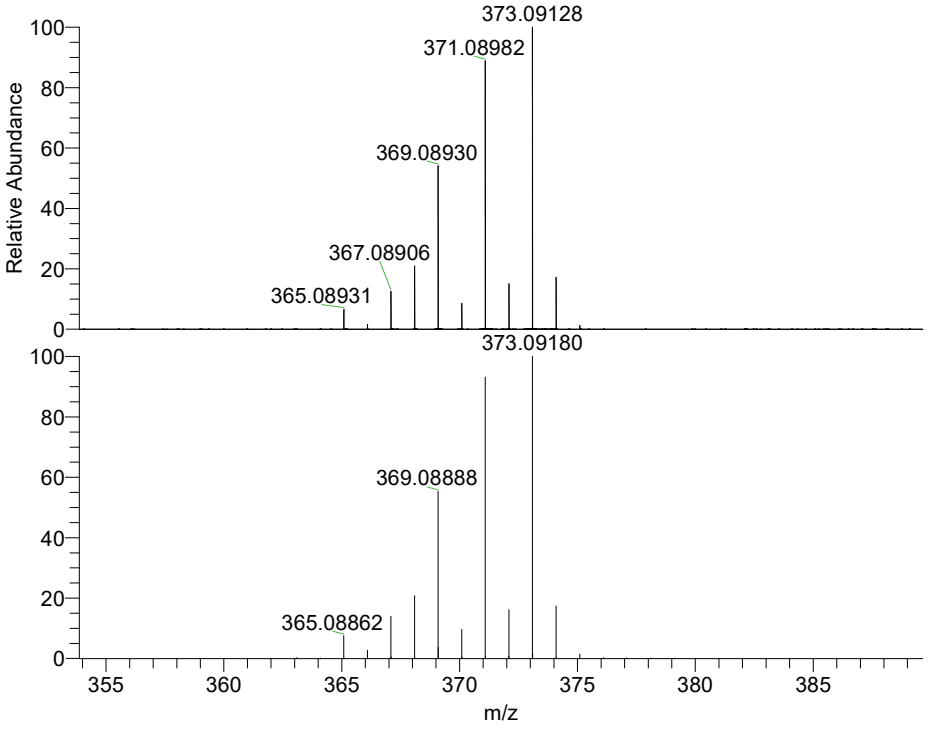

Figure S104. Experimental (top) and calculated (bottom) HR-MALDI-MS of **[NCN$^{t\mathrm{Bu}}$Te]OTf**.

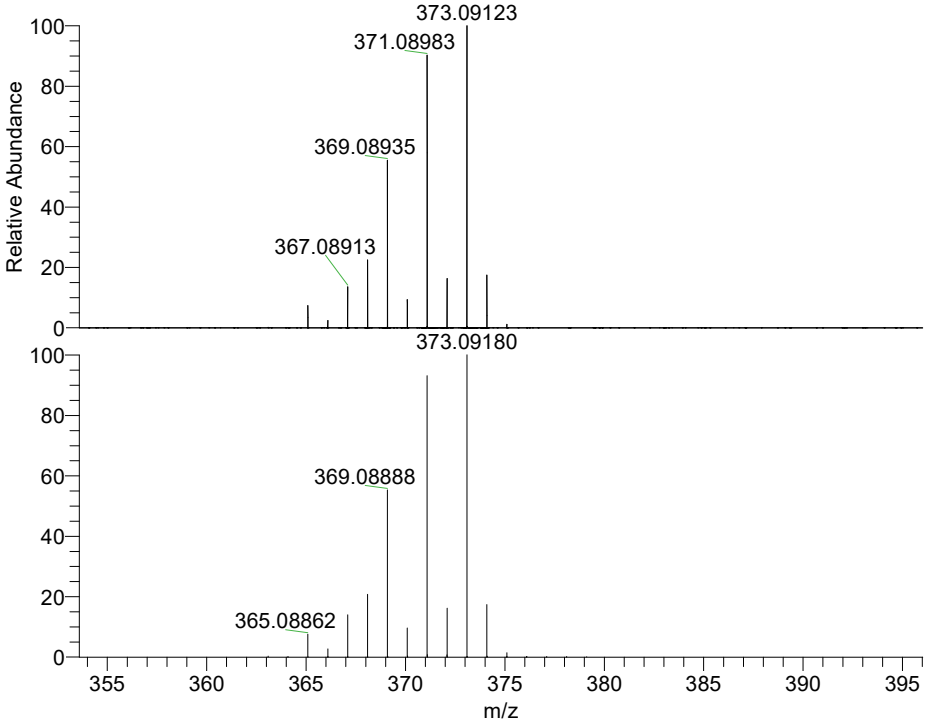

Figure S105. Experimental (top) and calculated (bottom) HR-MALDI-MS of **[NCN^{tBu}Te]SbF$_6$**.